



Energy management at the quantum scale : from thermal machines to energy transport

Pierre Doyeux

► To cite this version:

Pierre Doyeux. Energy management at the quantum scale : from thermal machines to energy transport. Quantum Physics [quant-ph]. Université Montpellier, 2017. English. NNT : 2017MONT070 . tel-01945333

HAL Id: tel-01945333

<https://theses.hal.science/tel-01945333>

Submitted on 5 Dec 2018

HAL is a multi-disciplinary open access archive for the deposit and dissemination of scientific research documents, whether they are published or not. The documents may come from teaching and research institutions in France or abroad, or from public or private research centers.

L'archive ouverte pluridisciplinaire **HAL**, est destinée au dépôt et à la diffusion de documents scientifiques de niveau recherche, publiés ou non, émanant des établissements d'enseignement et de recherche français ou étrangers, des laboratoires publics ou privés.

THÈSE POUR OBTENIR LE GRADE DE DOCTEUR DE L'UNIVERSITÉ DE MONTPELLIER

En Physique

École doctorale Information, Structures, Systèmes (I2S)

Unité de recherche UMR5221 – Laboratoire Charles Coulomb (L2C)

**Energy management at the quantum scale:
from thermal machines to energy transport**

**Présentée par Pierre DOYEUX
Le 20 Novembre 2017**

Sous la direction de Mauro ANTEZZA

Devant le jury composé de

Mário G. SILVEIRINHA, Professeur associé, Universidade de Lisboa

Guido PUPILLO, Professeur, Université de Strasbourg

Angela VASANELLI, Professeur, Université Paris-Diderot

David DEAN, Professeur, Université de Bordeaux

Mauro ANTEZZA, Maître de conférence, Université de Montpellier

Riccardo MESSINA, Chargé de recherche, Université de Montpellier

Rapporteur

Rapporteur

Présidente

Examineur

Directeur

Co-encadrant



**UNIVERSITÉ
DE MONTPELLIER**

En mémoire de mon père

Contents

Acknowledgements	iii
Résumé	v
Introduction	xi
1 Multipartite open quantum systems	1
1.1 Markovian quantum master equation	2
1.2 Energy fluxes	8
1.3 Correlations and other measures	10
1.4 A basic example	13
2 Energy transport in atomic chains in a thermal environment	17
2.1 Introduction	17
2.2 Physical system	19
2.3 Mathematical description of the system	20
2.4 Long-range transport and efficiency amplification	23
2.5 Preliminary investigations	25
2.6 Steady-state analysis	27
2.7 Dynamics	32
2.8 Chains with more atoms	38
2.9 Conclusion	40
3 Energy transport in atomic chains close to photonic topological insulators	43
3.1 Introduction	43
3.2 Physical system	44
3.3 Generalized master equation and basic example	47
3.4 Transport-efficiency enhancement induced by unidirectional-SPP	50
3.5 Practical advantages	52
3.6 Physical insight with two-atom chains	56
3.7 Conclusion	59
4 Quantum thermal machine out of thermal equilibrium	61
4.1 Introduction	61
4.2 Physical system	63
4.3 Open quantum system and out-of-thermal-equilibrium environment	64
4.4 Three-level atom as quantum thermal machine	71

4.5	Role of correlations in thermodynamic tasks	75
4.6	Robustness of thermal tasks	84
4.7	Tuning thermodynamical tasks	86
4.8	Variation of the number of qubits	89
4.9	Conclusion	92
Conclusion		95
List of publications		97
Notes on the numerical results		99
Bibliographie		110

Acknowledgements

Looking back at these three years of PhD thesis, I can fully appreciate how much a great experience it was not only from scientific and intellectual perspectives, but also on a human level. I would like to thank the following people who played an important role in my life during this period.

Pour commencer, je tiens à remercier mon directeur de thèse, Mauro Antezza. Je te serai toujours reconnaissant de m'avoir offert la possibilité de faire cette thèse et de travailler sur des sujets passionnants. J'ai beaucoup appris sous ta direction et j'ai eu la chance de profiter de ton expérience, en particulier sur la façon de mener des recherches face à des problèmes scientifiques ambitieux. Tu m'as toujours soutenu, encouragé et aussi offert la possibilité de voyager dans le cadre de ma formation, ce qui a été pour moi très bénéfique tant sur le plan scientifique que personnel. De manière générale, merci pour ton aide et pour avoir su me guider adroitement pendant ces trois années de thèse qui ont été si importantes pour moi.

Je souhaite également remercier Riccardo Messina qui a co-encadré cette thèse. À dire vrai, je ne saurais être capable de te remercier à la hauteur de tout ce que tu m'as apporté en seulement quelques lignes. Je me contenterai d'une simple énumération (non exhaustive) dont chaque élément mériterait un paragraphe à lui seul ; ainsi, Riccardo, merci pour ta gentillesse, ton soutien et ton amitié, pour la rigueur que tu as su me transmettre, ainsi que pour tes partages scientifiques, musicaux, culinaires, "LOSTiens", sans oublier ta disponibilité sans faille, à l'image de l'engagement dont tu as fait preuve vis-à-vis de mon encadrement.

I would also like to thank Angela Vasanelli, Guido Pupillo, Mário G. Silveirinha and David Dean for accepting to be part of the thesis committee, taking the time to read the manuscript and making constructive suggestions on my work.

Je remercie Bruno Leggio qui a été post-doc dans notre équipe et que j'ai eu la chance de cotoyer pendant la première moitié de ma thèse. En particulier, je tiens à te dire merci d'abord pour ta bonne humeur quotidienne, mais aussi pour toute la pédagogie et la patience dont tu as fait preuve en partageant avec moi tes connaissances scientifiques. Merci pour ton aide et le temps précieux que m'as accordés.

I also want to thank George W. Hanson and Seyyed Ali Hassani Gangaraj with whom I had the chance to collaborate on the exciting topic of photonic topological insulators. It was a real pleasure working with both of you.

Je tiens à remercier les membres du Laboratoire Charles Coulomb pour m'avoir aussi bien accueilli lors de mon arrivée, et en particulier Nicola Bartolo et Antonio Noto, qui m'ont permis de m'intégrer très vite, sans oublier Brahim Guizal qui m'a transmis toujours dans la bonne humeur une part de sa grande culture, qu'elle soit scientifique ou générale. Merci

également à Laëtitia Doyennette pour les conseils et l'aide qu'elle m'a apportés vis-à-vis des enseignements.

Je remercie les personnes avec qui j'ai eu le plaisir de partager mon bureau au cours de ces trois années. Merci à Maha et Hamis, pour leur gentillesse et m'avoir fait découvrir leur belle culture tunisienne. Merci à Richard et Florian, notamment pour nos discussions (parfois quelque peu animées) lors de nos repas tous les trois sur des sujets (méta-)physiques, philosophiques, politiques, d'actualités, ou encore culturels qui ont été très enrichissantes et demeurent pour moi d'excellents souvenirs. J'ai passé de très bons moments avec vous, aussi bien à l'université qu'en dehors où j'ai également eu le plaisir de cotoyer vos proches. Je remercie aussi François et lui souhaite bonne chance pour la nouvelle aventure qu'il commence.

Je tiens bien évidemment à remercier Abir ainsi que Chahine et Carine pour leur grande générosité et leur amitié. Votre soutien m'a été très précieux, notamment pendant les derniers mois de thèse qui ont été intenses à bien des égards. Je tiens particulièrement à vous dire "*choukran*" pour votre ouverture d'esprit qui nous a permis d'avoir des discussions extrêmement enrichissantes.

Je veux aussi remercier Johan, Rémi, Emmanuel, Catherine, Nicolas, Jennifer, Kévin, Boris, Thomas, Pierre, sans oublier Théo, Bac, Tarek, Jean-Maxime et Chloé, Anthony qui m'honnorent de leur amitié depuis toutes ces années.

Pour terminer, "*last but not least*", je remercie ma famille qui a toujours été présente dans les moments importants de ma vie. Merci pour l'affection et le soutien sans faille que vous m'avez toujours apportés.

Résumé

L'une des difficultés majeures à laquelle font face de nombreuses technologies réside dans la capacité à manipuler de l'énergie (sous quelque forme que ce soit) avec le plus de précision possible, tout en limitant les pertes au maximum. Ceci est non seulement vrai à l'échelle macroscopique, mais aussi à des échelles bien plus réduites où les effets quantiques ne sont plus négligeables. En effet, suite aux avancées technologiques au cours des dernières décennies, accompagnées du développement de nouvelles techniques expérimentales, il est désormais possible de manipuler la matière aux échelles micro- et nanoscopiques. Parmi ces techniques peuvent être cités les pièges à ions [1], les atomes froids piégés dans des réseaux optiques [2], ou encore les qubits supraconducteurs [3]. Toutes ces méthodes ouvrent la voie à de nouvelles études expérimentales plus poussées, ainsi qu'au développement de nouvelles technologies basées sur des systèmes élémentaires ne faisant intervenir qu'un ou quelques émetteurs quantiques [4]. De tels systèmes pourraient, par exemple, être utiles à la réalisation de communication quantique [5], ou encore au développement de réseaux et/ou de calculateurs quantiques [6, 7]. Une possibilité alternative est de s'inspirer de systèmes naturels présentant divers attraits, tels que les complexes photosynthétiques [8–10] qui jouent le rôle d'antenne en récoltant l'énergie solaire, puis en la transportant de manière remarquablement efficace vers le centre de réaction, ce qui en l'occurrence fait de ces complexes un modèle particulièrement intéressant vis-à-vis du développement de capteurs photovoltaïques [11]. Il est aussi possible d'envisager des systèmes quantiques capables de contrôler les échanges d'énergie au sein de systèmes biologiques [12].

Le point commun entre toutes ces idées novatrices réside dans le fait qu'elles nécessitent un certain degré de contrôle de l'énergie à l'échelle quantique. La manipulation d'énergie dans des systèmes composés de quelques émetteurs quantiques peut prendre divers aspects, et a été le sujet de nombreuses investigations. Par exemple, le transport d'énergie a été étudié le long de chaînes de systèmes quantiques à deux niveaux d'énergie [13], ou encore dans des chaînes d'ions piégés [14, 15]. Des circuits supraconducteurs ont également été proposés dans le but de reproduire le transport d'excitons au sein des complexes photosynthétiques mentionnés précédemment [16]. Ces complexes ont de plus attiré une attention considérable sur le cas plus général du transport d'énergie dans des systèmes quantiques ouverts, où notamment le lien entre échanges d'énergie par effet de cohérence quantique et dissipation induite par l'environnement a généré de nombreuses discussions [17]. Les environnements dissipatifs ont par ailleurs un rôle important dans le fonctionnement des machines thermiques quantiques à absorption, dont il a été montré que certaines sont capables de fournir de l'énergie de manière continue à un émetteur quantique [18]. Augmenter la distance d'interaction entre

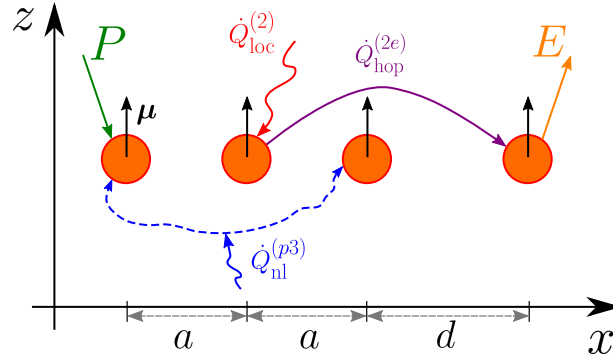


Figure 1: Système étudié dans le Chap. 2 : une chaîne d’atomes à deux niveaux d’énergie qui se trouve plongée dans un bain thermique et dont de l’énergie est pompée à une extrémité et extraite à l’autre. On étudie l’efficacité du transport d’énergie de la chaîne. L’interaction entre chaque atome et le champ électromagnétique environnemental donne lieu à différents types d’interactions qui modifient l’énergie du système quantique (ou de ses sous-systèmes), ce qui influence l’efficacité du transport.

deux émetteurs quantiques est également intéressant d’un point de vue du contrôle d’énergie. Pour ce faire, une méthode souvent employée consiste à coupler les deux émetteurs à travers l’intermédiaire d’un mode électromagnétique capable transporter l’énergie d’un émetteur à l’autre [19]. Tous les exemples cités ci-dessus ne sont que quelques propositions tirées parmi de nombreux travaux de recherche qui pourraient potentiellement apporter des solutions permettant d’augmenter l’efficacité avec laquelle l’énergie est manipulée aux seins de systèmes quantiques élémentaires. Le développement de toutes ces propositions, et de manière plus générale, avoir la capacité de fournir ou d’extraire de l’énergie à une sous-partie arbitrairement choisie d’un système quantique, ou encore de pouvoir régler la force d’interaction entre ses différents composants avec un haut degré de précision, pourraient amener les technologies reposant sur des systèmes quantiques élémentaires vers un nouveau paradigme.

Cette thèse présente l’étude théorique de trois systèmes physiques différents faisant preuve de propriétés remarquables en termes de manipulation d’énergie dans le contexte des *systèmes quantiques ouverts*. Plus précisément, chacun de ces systèmes est composé de quelques émetteurs quantiques (“atomes”) à deux ou trois niveaux d’énergie en interaction avec leur environnement respectif. Dans chacun des cas, le système quantique interagit avec son environnement dans la *limite de couplage faible*, ce qui permet, à l’aide de quelques hypothèses supplémentaires, de décrire l’évolution temporelle de la matrice densité réduite du système quantique par une *équation maîtresse quantique markovienne*. Le premier chapitre contient le calcul explicite d’une telle équation dans le cas particulier d’une chaîne d’atomes à deux niveaux d’énergie qui interagissent en couplage faible avec un champ électromagnétique environnemental. Les équations maîtresses des chapitres suivants peuvent être facilement adap-

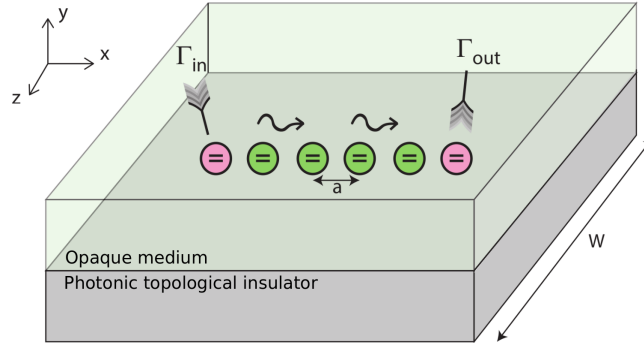


Figure 2: Système étudié dans le Chap. 3 : une chaîne d’atomes à deux niveaux d’énergie se situe à l’interface entre un isolant topologique photonique et un milieu opaque. Du fait de la topologie non-triviale de l’isolant topologique, il existe un plasmon polariton de surface qui se propage unidirectionnellement le long de la chaîne et qui assiste le transport d’énergie.

tées à partir de celle du premier chapitre. Par ailleurs, la dynamique du système ouvert étant décrite par une équation maîtresse markovienne, les notions de thermodynamiques quantiques telles que l’énergie interne du système quantique, ou la notion de chaleur et de travail dans ce contexte particulier sont également présentées dans ce chapitre.

Le Chap. 2, qui discute des résultats présentés dans la Réf. [20], est dédié à l’étude du transport d’énergie le long d’une chaîne de $N = 2 \dots, 7$ atomes à deux niveaux d’énergie (voir Fig. 1), de fréquence de transition $\omega_0 = 10^{14} \text{ rad} \cdot \text{s}^{-1}$, qui interagissent en couplage faible avec un rayonnement de corps noir à la température T . Comme indiqué précédemment, l’évolution temporelle de la matrice densité réduite associée à la chaîne atomique est décrite par une équation maîtresse markovienne. Le facteur de mérite utilisé pour caractériser les performances de la chaîne vis-à-vis du transport d’énergie est *l’efficacité* χ . Pour l’évaluer, de l’énergie est pompée de manière non-cohérente à un bout de la chaîne, et extraite à l’autre bout, de façon non-cohérente également. L’efficacité est obtenue en comparant deux scénarios : le scénario sans pompage, où seule l’extraction est réalisée, et le scénario avec pompage (et extraction). En notant E (E_0) l’énergie¹ extraite en présence (absence) de pompage, et P l’énergie pompée dans la chaîne, l’efficacité s’exprime alors

$$\chi = \frac{E - E_0}{P}. \quad (1)$$

Avoir $\chi = 0$ signifie que l’énergie extraite en présence de pompage est égale à celle extraite dans le cas sans pompage ($E = E_0$), traduisant la perte totale de l’énergie injectée dans la chaîne. En revanche, lorsque $\chi = 1$, la quantité d’énergie supplémentaire extraite en présence de pompage est exactement la même que celle injectée ($E - E_0 = P$), indiquant que l’énergie a été transportée avec 100% d’efficacité.

¹Rigoureusement, il s’agit en réalité d’un *flux* d’énergie.

Le résultat principal présenté dans ce chapitre est que dans certaines configurations géométriques et thermiques, l'efficacité peut non seulement atteindre 100% ($\chi = 1$), mais peut aussi dépasser cette valeur, et être amplifiée jusqu'à atteindre 1400% dans le meilleur des cas étudiés. Pour expliquer ce résultat, une analyse détaillée des flux d'énergie est effectuée tout d'abord à l'état stationnaire, puis au cours de la dynamique. Cette étude révèle l'action d'un *injecteur d'excitations*, qui comme son nom l'indique, absorbe de l'énergie du champ environnemental et l'injecte dans la chaîne. Il faut noter, d'une part, que cet effet est déclenché par le pompage, qui induit une redistribution des flux d'énergie, et d'autre part, que l'amplification de l'efficacité ($\chi > 1$) n'est possible que lorsque les effets thermiques sur la dynamique de la chaîne deviennent significatifs (ici, approximativement : $T > 200$ K). Le deuxième résultat important de ce chapitre est que lorsque l'amplification d'efficacité est réalisée, la distance sur laquelle le transport d'énergie est effectué peut être considérablement augmentée.

Le Chapitre 3 discute des résultats décrits dans la Réf. [21], et similairement au Chap. 2, traite du transport d'énergie le long de chaîne d'atomes à deux niveaux d'énergie, qui ont ici pour fréquence de transition $\nu_0 = 200$ THz (voir Fig. 2). La spécificité de ce système vient du fait que la chaîne atomique se trouve à l'interface d'un *isolant topologique photonique* (ITP) (avec un milieu opaque), qui a la particularité d'avoir une structure de bandes dotée d'une topologie non-triviale. Il s'ensuit qu'à l'interface d'un ITP peuvent exister des plasmons polaritons de surface (PPS) qui se propagent de manière non-réciproque, voire même dans certains cas, *unidirectionnellement*. Dans notre cas, il existe un tel PPS (unidirectionnel) qui se propage le long de la chaîne atomique et qui participe au transport d'énergie. Tout comme pour le Chap. 2, de l'énergie est pompée à un bout de la chaîne et extraite à l'autre bout, et l'efficacité définie par l'Eq. (1) caractérise la qualité du transport d'énergie. Le principal résultat de ce chapitre vient de la comparaison de l'efficacité entre deux scénarios : lorsque le transport est assisté par un PPS unidirectionnel (qui se propage le long de la chaîne), et lorsqu'il est assisté par un PPS réciproque (qui se propage sans direction privilégiée). L'étude effectuée dans ce chapitre montre que le PPS unidirectionnel résulte en une efficacité surpassant celle de son homologue réciproque de *plus d'un ordre de grandeur*.

Par ailleurs, une des propriétés particulièrement intéressante de l'ITP réside dans le fait que le PPS est pratiquement insensible à la réflexion. En effet, de manière générale, en considérant un PPS réciproque, lorsqu'il rencontre un obstacle, celui-ci a pour effet de réfléchir une partie du PPS. En revanche, dans le cas d'un PPS unidirectionnel généré par un ITP, le canal de réflexion étant inexistant, le PPS n'a d'autre possibilité que de contourner l'obstacle et de poursuivre sa route². Dans ce chapitre, il est montré que lorsqu'un obstacle se situe au milieu de la chaîne, l'efficacité du transport d'énergie assisté par un PPS réciproque devient

²Pour être complet : il faut aussi que, comme dans le cas dans notre système, le PPS se situe dans une bande interdite partagée par les deux milieux constituant l'interface, de sorte que le rayonnement au sein de chaque milieu soit impossible.

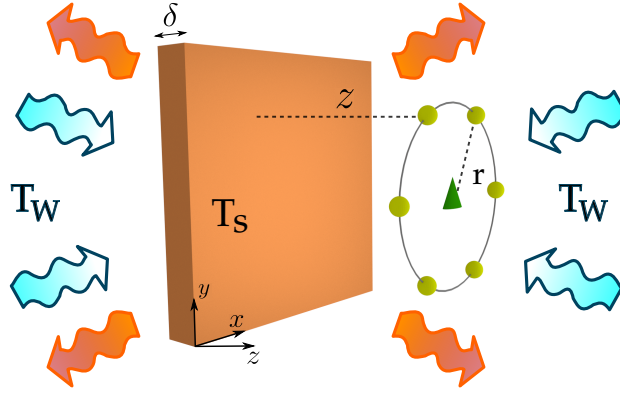


Figure 3: Système étudié dans le Chap. 4 : un système quantique est situé à proximité d’une plaque de saphire à la température T_S . La plaque et le système sont soumis à un rayonnement de corps noir à une température T_W qui diffère de T_S . Le système quantique est composé d’un atome à trois niveaux, jouant le rôle de machine thermique quantique, chauffant ou refroidissant les atomes à deux niveaux qui sont positionnés autour d’elle.

presque nulle, alors que dans le cas d’un PPS unidirectionnel, elle est remarquablement peu affectée par la présence de l’obstacle. Ce résultat est particulièrement intéressant vis-à-vis de réalisations expérimentales, où des défauts de fabrication (obstacles) peuvent exister à l’interface.

Le Chap. 4 de cette thèse, présentant les résultats des Réfs. [22, 23], s’intéresse à une machine thermique quantique. Plus précisément, un système quantique est plongé dans un champ électromagnétique se trouvant hors équilibre thermique (voir Fig. 3). Cette configuration hors équilibre est due à la présence d’une plaque de saphire d’épaisseur $\delta = 5$ nm ayant une température T_S , qui est soumise à un rayonnement de corps noir caractérisé par une température T_W telle que $T_W \neq T_S$. Le système quantique, situé à proximité de la plaque, est composé d’un atome à trois niveaux d’énergie et de N atomes à deux niveaux (“qubits”). Après avoir introduit les quantités nécessaires, et en particulier la notion de température associée à une transition atomique, il est possible de montrer que l’atome à trois niveaux joue le rôle de machine thermique quantique : grâce au champ électromagnétique qui est hors équilibre thermique, cet atome est capable d’interagir avec les atomes à deux niveaux de sorte à diminuer leur énergie, c’est-à-dire à les refroidir. Le processus inverse est également possible : la machine peut chauffer (donner de l’énergie aux) qubits. Il est important de noter que ces deux “tâches thermiques” s’opèrent lorsque le système est dans son état stationnaire. Cet effet a été étudié d’abord dans la Réf. [18] en présence d’un seul qubit, c’est-à-dire pour $N = 1$, et est poursuivie dans ce chapitre dans les cas $1 \leq N \leq 6$. Les qubits forment un polygone régulier à N sommets centré sur la machine, et l’ensemble des atomes appartient au plan parallèle à la surface de la plaque. La tâche thermique délivrée par la machine sur les qubits est étudiée en fonction de la distance entre la plaque et le système atomique. En

particulier, il est montré qu'il existe des régimes où la machine chauffe les qubits jusqu'à les amener en inversion des populations : la probabilité qu'ils soient dans leur état excité est supérieure à celle de leur état fondamental. Inversement, la machine est capable de refroidir considérablement les qubits. De plus, ces tâches thermiques sont non seulement effectuées sur chaque qubit indépendamment, mais aussi sur le sous-système des qubits dans son ensemble. Il est remarquable que la machine puisse réaliser des tâches d'une telle intensité sur des systèmes bien plus grands qu'elle en termes de dimensions d'espace de Hilbert.

De surcroît, une configuration spécifique est étudiée avec $N = 4$, où seuls deux des quatre qubits interagissent avec la machine. L'analyse de ce système montre que malgré cette absence d'interactions, la température des quatre qubits est grandement affectée par la présence de la machine. Cela est dû à l'interaction entre les qubits, et le mécanisme de *partage des tâches* est mis en avant : les deux qubits couplés à la machines relaient la tâche thermique et la transmettent à ceux qui n'interagissent pas directement avec elle. Dans le chapitre, la révélation de ce mécanisme se fait notamment à l'aide des corrélations entre différentes partitions du système quantique, et il est montré que la contribution des corrélations de nature purement quantique est négligeable. Par ailleurs, le contrôle des tâches thermiques ainsi que leur robustesse sont étudiés sous divers aspects.

Introduction

Manipulating energy with as much control and as little loss as possible is a problematic at the heart of many technologies. This is the case not only at the macroscopic scale, but also at much smaller ones where quantum effects may play a crucial role. More specifically, with the development of technologies and experimental techniques over the past decades, it is now achievable to maneuver matter at the micro- or nano- scales. Among these techniques, one could cite ion trapping [1], cold atoms in optical lattices [2], or superconducting qubits [3]. All these methods pave the way for future experiments and the design of new technologies based on elementary systems involving either a single or very few quantum emitters [4]. Such quantum systems could be used to realize quantum communication [5], or to design quantum networks [6], as well as quantum-computation processing [7]. Another possibility would be to mimic relevant natural systems, e.g., the celebrated photosynthetic antenna complexes [8–10], which collect and transport solar radiation to the reaction center with high efficiency, and are particularly interesting with regards to the improvement of photovoltaic cells [11]. One could also consider designing quantum systems capable of controlling energy exchanges in biological constituents [12].

All these promising developments share the common feature to require a certain degree of energy management, which has been explored under many different aspects. For example, energy transport within chains of trapped ions [14, 15] or two-level quantum emitters [13] has been under study. Superconducting circuits have also been proposed to reproduce the exciton transport of the antenna photosynthetic complexes mentioned above [16]. These complexes have additionally triggered a lot of interest on the interplay between quantum coherent energy exchanges and environment-induced dissipation with regards to energy transport within open quantum systems [17]. Such environments can also be exploited through the design of absorption quantum thermal machines to provide energy to single quantum emitters [18]. Moreover, improving the range of interaction between quantum emitters can be fruitful in terms of energy management. This is typically realized by coupling the emitters to an engineered electromagnetic mode mediating the interaction between them [19]. These are only a few examples out of many investigations potentially providing new methods to manage energy within elementary quantum systems. The development of all these different aspects, and more generally, having the capacity of yielding energy to an arbitrary subpart of a quantum system, or tuning with a high degree of precision the interaction strength between its components, could bring the technologies based on systems involving a few elementary quantum emitters to a new paradigm.

This thesis presents the theoretical investigation of three different physical systems which

exhibit noticeable properties with respect to energy management in the framework of *open quantum systems*. To be more specific, each of them will be composed of a few two- or three-level quantum emitters ('atoms') embedded in a common environment with which they will be interacting. It is important to stress that we will consider system–environment interactions in the *weak-coupling limit*, so that in addition to further approximations, the dynamics of the three quantum systems will be described by *Markovian quantum master equations*. This framework will allow us to analyze the energy exchanges involving the open systems through a quantum-thermodynamical approach. More precisely, we will introduce the concept of internal energy of the quantum system, and the notion of energy flux in this context, which will be the main quantities we will consider to investigate the three systems.

The thesis is structured of four chapters. Chapter 1 can be viewed as an introduction, where we will consider a simple open quantum system for which the Markovian quantum master equation will be derived explicitly. The master equations of the other chapters will be easily adapted from this one. Moreover, we will also define the quantum-thermodynamical notions and other measures that will be used in the following, and we will conclude with an example illustrating some of the concepts previously introduced in the chapter.

Chapter 2 is dedicated to the investigation of energy-transport efficiency of a chain of two-level atoms (between 2 and 7) interacting with a blackbody radiation. We will see that for specific configurations, reaching 100% of transport efficiency is achievable around room temperature. More remarkably, we will demonstrate that exceeding this threshold is also possible for many system setups, reaching in some cases 1400% of efficiency. Moreover, when the efficiency is amplified, the transport range is increased as well. Through an analysis of the energy fluxes, we will determine the origin of this effect: an atomic triplet belonging to the chain plays the role of excitation injector, drawing energy from the environment and increasing the quantum-system energy during the transport process. This is only possible when the temperature of the environment is significant (around room temperature). This chapter discusses the results presented in Ref. [20].

Chapter 3 also addresses the energy-transport efficiency of a two-level-atom chain, although thermal effects are negligible in this case. The chain is located at the interface of a photonic topological insulator (PTI), where a unidirectional surface-plasmon-polariton (SPP) can exist, propagating in the bulk band gap and immune to backscattering. By comparing SPP-assisted energy transport between bi- and uni-directional SPPs, we show that the PTI-induced unidirectional SPP leads to a transport efficiency larger than the bidirectional one, by one or more orders of magnitude. Moreover, we highlight different aspects stemming from the use of the photonic topological insulator which are particularly relevant for practical realizations, among which the remarkable robustness of energy transport in the presence of significant defects on the SPP path, or the increase of transport range, as well as the possibility to literally switch off the energy-transport process. The results of this chapter are presented in Ref. [21].

Chapter 4 is devoted to the study of a quantum system immersed in an out-of-thermal-equilibrium environment. The system is composed of an absorption quantum thermal machine, a three-level atom, around which are located a few two-level atoms ('qubits'). We show that the machine is able to yield (heat up) or absorb (cool down) energy to/from the qubits with significant intensity by considering systems involving from 1 to 6 qubits. In some cases, some of the qubits are affected by the machine although they are completely decoupled from it. This effect is analyzed in terms of correlations between the different subparts of the quantum system. Moreover, we propose different methods allowing one to tune thermal tasks, i.e., to control how much energy is yielded/absorbed to/from each qubit by the machine. The results of this chapter are presented in Refs. [22, 23].

Multipartite open quantum systems

Contents

1.1	Markovian quantum master equation	2
1.2	Energy fluxes	8
1.3	Correlations and other measures	10
1.3.1	Bipartite mutual information	11
1.3.2	Tripartite mutual information	11
1.3.3	Trace distance	11
1.3.4	Geometric quantum discord	12
1.4	A basic example	13

This first chapter is dedicated to the introduction of the mathematical tools that will be used in the analysis of the systems studied in the following chapters. All these physical systems have the common property of being open quantum systems weakly interacting with their respective environments. As such, their dynamics will be studied in the framework of Markovian open quantum systems. For this reason, Sec. 1.1 is dedicated to the derivation of a Markovian quantum master equation describing the dynamics of a specific quantum system weakly interacting with a ‘generic’ stationary electric field. This will be useful as only minor modifications of this master equation will be necessary to describe appropriately the dynamics of the systems under consideration in the next chapters.

In Sec. 1.2, based on the master equation, we compute the energy fluxes stemming from the field-induced interactions participating to the system dynamics. They will be of major interest to understand the different effects observed in the next chapters, particularly in Chap. 2. In addition, this will allow us to introduce the notion of heat flux in the framework of quantum systems, which is used in Chap. 4 to describe the energy exchanges through a quantum-thermodynamical approach. In this same chapter, we will also employ several correlation quantifiers and other measures to analyze the interactions between different partitions of the system. These are briefly introduced in Sec. 1.3.

Finally, we conclude with Sec. 1.4 by applying the Markovian quantum master equation derived in Sec. 1.1 to an elementary open quantum system, which will allow us to illustrate miscellaneous notions that have been introduced throughout this chapter.

1.1 Markovian quantum master equation

The quantum system we consider in this section is composed of N two-level quantum emitters, which will be referred to as two-level ‘atoms’, or ‘qubits’, having an equal transition frequency ω_0 . The system is open as the qubits are weakly interacting with a stationary electric field. In this section, we derive a Markovian quantum master equation describing the dynamics of the quantum system. This derivation follows the scheme presented in Ref. [24] [see also [25–27]].

The total Hamiltonian describing this system is

$$H_{\text{tot}} = H_S + H_E + H_{\text{int}}, \quad (1.1)$$

where H_S and H_E are the free Hamiltonians of the quantum system (the qubits) and of the environment, respectively, and H_{int} is the Hamiltonian describing the interaction between these two subsystems. The total system is assumed to be closed, and is characterized by the density matrix $\rho(t)$. Its dynamics is determined by the von Neumann equation

$$\frac{d\rho(t)}{dt} = -\frac{i}{\hbar} [H_{\text{int}}(t), \rho(t)], \quad (1.2)$$

which is expressed in the interaction picture, where

$$H_{\text{int}}(t) = \exp\left(\frac{i}{\hbar}(H_S + H_E)t\right) H_{\text{int}} \exp\left(-\frac{i}{\hbar}(H_S + H_E)t\right) \quad (1.3)$$

is the interaction Hamiltonian in this picture. After integrating over time, we have

$$\rho(t) = \rho(0) - \frac{i}{\hbar} \int_0^t ds [H_{\text{int}}(s), \rho(s)], \quad (1.4)$$

where $\rho(0)$ is the system density matrix at the beginning of the time evolution. Re-injecting $\rho(t)$ in Eq. (1.2), and performing a partial trace over the degrees of freedom of the environment leads to

$$\frac{d\rho_S(t)}{dt} = -\frac{1}{\hbar^2} \text{Tr}_E \left(\int_0^t ds [H_{\text{int}}(t), [H_{\text{int}}(s), \rho(s)]] \right), \quad (1.5)$$

where we have assumed $\text{Tr}_E([H_{\text{int}}(t), \rho(0)]) = 0$, and where $\rho_S(t) = \text{Tr}_E(\rho(t))$ characterizes the reduced density matrix of the qubits system. From this point, we carry out a series of approximations that will lead us to a Markovian quantum master equation describing the time evolution of $\rho_S(t)$. Firstly, we perform the *weak-coupling* or *Born* approximation by assuming that the effect of the quantum system on the environment dynamics is negligible. This allows us to express the total density matrix as a product state: $\rho(t) = \rho_S(t)\rho_E$, where $\rho_E = \text{Tr}_S(\rho(t))$ is the reduced density matrix of the environment. Then, Eq. (1.5) becomes

$$\frac{d\rho_S(t)}{dt} = -\frac{1}{\hbar^2} \text{Tr}_E \left(\int_0^t ds [H_{\text{int}}(t), [H_{\text{int}}(s), \rho_S(s)\rho_E]] \right). \quad (1.6)$$

Secondly, we use the *Markov approximation*, which consists in assuming that the quantum-system time evolution only depends on the present state, leading to the replacement of $\rho_S(s)$ by $\rho_S(t)$ in Eq. (1.6). Moreover, we perform the change of variable $s \rightarrow t - s$, and extend the upper limit of the integral: $t \rightarrow +\infty$. This approximation is permitted when the correlation functions of the environment decay over a time scale τ_B that is small compared to τ_R , the relaxation time of the quantum system: $\tau_B \ll \tau_R$. In this case, the dynamics of the qubits is described on a coarse-grained time scale, for which the environment time evolution is not resolved. This yields the following Markovian quantum master equation

$$\frac{d\rho_S(t)}{dt} = -\frac{1}{\hbar^2} \text{Tr}_E \left(\int_0^{+\infty} ds [H_{\text{int}}(t), [H_{\text{int}}(t-s), \rho_S(t)\rho_E]] \right). \quad (1.7)$$

To develop Eq. (1.7), we need to express the interaction Hamiltonian in the interaction picture, $H_{\text{int}}(t)$. Under the dipole approximation, its expression in the Shrödinger picture reads

$$H_{\text{int}} = -\sum_i \mathbf{D}^{(i)} \cdot \mathbf{E}(\mathbf{r}_i), \quad (1.8)$$

where here and hereafter, the index i always takes the values $i \in \{1, \dots, N\}$. $\mathbf{D}^{(i)}$ is the dipole operator of the i -th qubit, and $\mathbf{E}(\mathbf{r}_i)$ is the electric-field operator at the position of this qubit, noted by \mathbf{r}_i . We will see that due to the Markov approximation, the action of the environment on the qubits dynamics will occur through the electric-field correlation functions. These will be determined from the fluctuation-dissipation theorem, valid at thermal equilibrium¹. Thus, the explicit form of the electric-field operator is not necessary here. It follows from Eq. (1.8) that the interaction picture of H_{int} is

$$H_{\text{int}}(t) = -\sum_i \mathbf{D}^{(i)}(t) \cdot \mathbf{E}(\mathbf{r}_i, t), \quad (1.9)$$

where $\mathbf{D}^{(i)}(t)$ and $\mathbf{E}(\mathbf{r}_i, t) = \exp\left(\frac{i}{\hbar} H_E t\right) \mathbf{E}(\mathbf{r}_i) \exp\left(-\frac{i}{\hbar} H_E t\right)$ are the dipole and electric-field operators in the interaction picture. To express $\mathbf{D}^{(i)}(t)$, we first introduce the following notations. The ground and excited energy levels of the i -th qubit are noted by $|g_i\rangle$ and $|e_i\rangle$, respectively, and we recall that the transition frequency ω_0 is the same for all the qubits, such that the free Hamiltonian of the system reads

$$H_S = \hbar\omega_0 \sum_i |e_i\rangle\langle e_i|. \quad (1.10)$$

To each qubit transition is associated the transition matrix element $\boldsymbol{\mu}^{(i)} = \langle g_i | \mathbf{D}^{(i)} | e_i \rangle$ of

¹In Chap. 4, we study a quantum system embedded in an out-of-thermal-equilibrium environment. However, the correlation functions can still be deduced from the fluctuation-dissipation theorem: this is possible by considering the total electromagnetic field as a sum of fields at thermal equilibrium, as will be detailed in Chap. 4.

the dipole operator $\mathbf{D}^{(i)}$. We stress that $\boldsymbol{\mu}^{(i)}$ is an induced fluctuating dipole due to the action of the electric field on the atomic transition. Here and in the next chapters, we will always assume real induced dipoles, such that $\boldsymbol{\mu}^{(i)} = \boldsymbol{\mu}^{(i)*}$. The dipole operator can thus be expressed as

$$\mathbf{D}^{(i)} = \sum_{\omega=\pm\omega_0} \mathbf{A}^{(i)}(\omega), \quad (1.11)$$

where ω can take the values $\omega = \pm\omega_0$, and where we have introduced the following operators

$$\mathbf{A}^{(i)}(\omega_0) = \boldsymbol{\mu}^{(i)} \sigma^{(i)}, \quad \mathbf{A}^{(i)}(-\omega_0) = \mathbf{A}^{(i)\dagger}(\omega_0) = \boldsymbol{\mu}^{(i)} \sigma^{(i)\dagger}, \quad (1.12)$$

with $\sigma^{(i)} = |g_i\rangle\langle e_i|$ being the lowering operator of the i -th qubit. The operators $\mathbf{A}^{(i)}(\pm\omega_0)$ are eigenoperators of the free Hamiltonian of the system with eigenvalues $\mp\hbar\omega_0$, in the sense that they verify the following commutation relations

$$[H_S, \mathbf{A}^{(i)}(\omega_0)] = -\hbar\omega_0 \mathbf{A}^{(i)}(\omega_0), \quad [H_S, \mathbf{A}^{(i)\dagger}(\omega_0)] = +\hbar\omega_0 \mathbf{A}^{(i)\dagger}(\omega_0). \quad (1.13)$$

The reason for expressing the dipole operator in terms of the eigenoperators $\mathbf{A}^{(i)}(\omega)$ is that their interaction-picture expression, noted by $\mathbf{A}^{(i)}(\omega, t)$, is

$$\mathbf{A}^{(i)}(\omega, t) = \exp\left(\frac{i}{\hbar} H_S t\right) \mathbf{A}^{(i)}(\omega) \exp\left(-\frac{i}{\hbar} H_S t\right) = e^{-i\omega_0 t} \mathbf{A}^{(i)}(\omega), \quad (1.14)$$

and it follows that the dipole operator in the interaction picture is

$$\mathbf{D}^{(i)}(t) = \sum_{\omega=\pm\omega_0} \mathbf{A}^{(i)}(\omega, t) = \sum_{\omega=\pm\omega_0} e^{-i\omega t} \mathbf{A}^{(i)}(\omega). \quad (1.15)$$

Then we can express the interaction Hamiltonian in the interaction picture:

$$\begin{aligned} H_{\text{int}}(t) &= - \sum_i \mathbf{D}^{(i)}(t) \cdot \mathbf{E}(\mathbf{r}_i, t), \\ &= - \sum_i \sum_{\omega=\pm\omega_0} e^{-i\omega t} \mathbf{A}^{(i)}(\omega) \cdot \mathbf{E}(\mathbf{r}_i, t), \\ &= - \sum_i \sum_{\omega=\pm\omega_0} \sum_{\alpha} e^{-i\omega t} A_{\alpha}^{(i)}(\omega) E_{\alpha}(\mathbf{r}_i, t), \end{aligned} \quad (1.16)$$

where here and in the following $\alpha \in \{x, y, z\}$ stands for the Cartesian components. As a remark, we note that H_{int} being Hermitian, it can be equivalently expressed as

$$\begin{aligned} H_{\text{int}}(t) &= - \sum_i \sum_{\omega=\pm\omega_0} \sum_{\alpha} e^{-i\omega t} A_{\alpha}^{(i)}(\omega) E_{\alpha}(\mathbf{r}_i, t), \\ &= - \sum_i \sum_{\omega=\pm\omega_0} \sum_{\alpha} e^{+i\omega t} A_{\alpha}^{(i)\dagger}(\omega) E_{\alpha}^{\dagger}(\mathbf{r}_i, t). \end{aligned} \quad (1.17)$$

Based on Eq. (1.17) and after some algebra, Eq. (1.7) leads to the following equation of

motion for the qubits reduced density matrix

$$\frac{d\rho_S(t)}{dt} = \sum_{i,j} \sum_{\alpha,\beta} \sum_{\omega=\pm\omega_0} \left(\Theta_{\alpha\beta}^{(ij)}(\omega) [A_\beta^{(j)}(\omega)\rho_S(t), A_\alpha^{(i)\dagger}(\omega)] + \Theta_{\beta\alpha}^{(ji)*}(\omega) [A_\alpha^{(i)}(\omega), \rho_S(t)A_\beta^{(j)\dagger}(\omega)] \right), \quad (1.18)$$

where we performed the rotating-wave approximation by eliminating the rapidly-oscillating terms. This can be operated when the intrinsic-evolution time scale of the open system, noted by τ_S , is much smaller than its relaxation time scale: $\tau_S \ll \tau_R$. Moreover, we have introduced the following functions

$$\Theta_{\alpha\beta}^{(ij)}(\omega) = \frac{1}{\hbar^2} \int_0^{+\infty} ds e^{i\omega s} \langle E_\alpha^\dagger(\mathbf{r}_i, t) E_\beta(\mathbf{r}_j, t-s) \rangle, \quad (1.19)$$

which involve the correlation functions of the electric field

$$\langle E_\alpha^\dagger(\mathbf{r}_i, t) E_\beta(\mathbf{r}_j, t-s) \rangle = \text{Tr}_E \left(E_\alpha^\dagger(\mathbf{r}_i, t) E_\beta(\mathbf{r}_j, t-s) \rho_E \right). \quad (1.20)$$

As mentioned before, we are considering an environmental electric field that is stationary ($[H_E, \rho_E] = 0$), such that the correlation functions are homogeneous in time:

$$\langle E_\alpha^\dagger(\mathbf{r}_i, t) E_\beta(\mathbf{r}_j, t-s) \rangle = \langle E_\alpha^\dagger(\mathbf{r}_i, s) E_\beta(\mathbf{r}_j, 0) \rangle. \quad (1.21)$$

In addition, the following decomposition can be realized

$$\Theta_{\alpha\beta}^{(ij)}(\omega) = \frac{1}{2} \gamma_{\alpha\beta}^{(ij)}(\omega) + i s_{\alpha\beta}^{(ij)}(\omega), \quad (1.22)$$

where we have used

$$\gamma_{\alpha\beta}^{(ij)}(\omega) = \Theta_{\alpha\beta}^{(ij)}(\omega) + \Theta_{\beta\alpha}^{(ji)*}(\omega) = \frac{1}{\hbar^2} \int_{-\infty}^{+\infty} ds e^{i\omega s} \langle E_\alpha^\dagger(\mathbf{r}_i, s) E_\beta(\mathbf{r}_j, 0) \rangle, \quad (1.23)$$

$$s_{\alpha\beta}^{(ij)}(\omega) = \frac{1}{2i} \left(\Theta_{\alpha\beta}^{(ij)}(\omega) - \Theta_{\beta\alpha}^{(ji)*}(\omega) \right). \quad (1.24)$$

The main interest of this decomposition is to allow us to clearly identify the terms that will contribute to the dissipative and unitary dynamics of $\rho_S(t)$, the functions $\gamma_{\alpha\beta}^{(ij)}(\omega)$ and $s_{\alpha\beta}^{(ij)}(\omega)$, respectively. It follows that Eq. (1.18) can be formulated as

$$\begin{aligned} \frac{d\rho_S(t)}{dt} = & \sum_{i,j} \sum_{\alpha,\beta} \sum_{\omega=\pm\omega_0} \left\{ \frac{1}{2} \gamma_{\alpha\beta}^{(ij)}(\omega) \left([A_\beta^{(j)}(\omega)\rho_S(t), A_\alpha^{(i)\dagger}(\omega)] + [A_\alpha^{(i)}(\omega), \rho_S(t)A_\beta^{(j)\dagger}(\omega)] \right) \right. \\ & \left. + i s_{\alpha\beta}^{(ij)}(\omega) \left([A_\beta^{(j)}(\omega)\rho_S(t), A_\alpha^{(i)\dagger}(\omega)] - [A_\alpha^{(i)}(\omega), \rho_S(t)A_\beta^{(j)\dagger}(\omega)] \right) \right\}. \end{aligned} \quad (1.25)$$

By introducing the following functions,

$$S_{\pm}^{(ij)}(\omega) = \sum_{\alpha, \beta} \mu_{\alpha}^{(i)} \mu_{\beta}^{(j)} s_{\alpha\beta}^{(ij)}(\pm\omega), \quad (1.26)$$

$$\Gamma_{\text{em}}^{(ij)}(\omega) = \sum_{\alpha, \beta} \mu_{\alpha}^{(i)} \mu_{\beta}^{(j)} \gamma_{\alpha\beta}^{(ij)}(\omega), \quad (1.27)$$

$$\Gamma_{\text{abs}}^{(ij)}(\omega) = \sum_{\alpha, \beta} \mu_{\alpha}^{(i)} \mu_{\beta}^{(j)} \gamma_{\alpha\beta}^{(ij)}(-\omega), \quad (1.28)$$

and with the help of Eq. (1.12), we obtain the following interaction-picture master equation for the dynamics of the qubits reduced density matrix

$$\begin{aligned} \frac{d\rho_S(t)}{dt} = \sum_{i,j} \bigg\{ & \frac{1}{2} \Gamma_{\text{em}}^{(ij)}(\omega_0) \left([\sigma^{(j)} \rho_S(t), \sigma^{(i)\dagger}] + [\sigma^{(i)}, \rho_S(t) \sigma^{(j)\dagger}] \right) \\ & + \frac{1}{2} \Gamma_{\text{abs}}^{(ij)}(\omega_0) \left([\sigma^{(j)\dagger} \rho_S(t), \sigma^{(i)}] + [\sigma^{(i)\dagger}, \rho_S(t) \sigma^{(j)}] \right) \\ & + i S_{+}^{(ij)}(\omega_0) \left([\sigma^{(j)} \rho_S(t), \sigma^{(i)\dagger}] - [\sigma^{(i)}, \rho_S(t) \sigma^{(j)\dagger}] \right) \\ & + i S_{-}^{(ij)}(\omega_0) \left([\sigma^{(j)\dagger} \rho_S(t), \sigma^{(i)}] - [\sigma^{(i)\dagger}, \rho_S(t) \sigma^{(j)}] \right) \bigg\}. \end{aligned} \quad (1.29)$$

Firstly, we note that all the coefficients involved here have units of inverse time. The coefficients $\Gamma_{\text{em/abs}}^{(ij)}(\omega_0)$ are the rates associated to the photon emission/absorption processes. They involve either a single ($i = j$) or a pair ($i \neq j$) of qubit(s), and in the following we will refer to them as ‘local’ and ‘non-local’ rates, respectively. The coefficients $S_{\pm}^{(ij)}(\omega_0)$, when $i \neq j$, characterize environment-mediated long-range dipole–dipole interactions, transferring energy between two qubits. When $i = j$, they correspond (to a factor \hbar) to Lamb-type renormalization of the qubits energy levels due to the interaction with their environment. It is important to stress that this master equation is not yet the typical Markovian quantum master equation for the density matrix of a quantum system interacting with an environmental field that one usually finds in the literature [24, 26], which is given below. Indeed, Eq. (1.29) takes into account the possibility that the environment of the quantum system might be non-reciprocal, in which case the correlation functions are such that $\Gamma_{\text{em/abs}}^{(ij)}(\omega) \neq \Gamma_{\text{em/abs}}^{(ji)}(\omega)$ and $S_{\pm}^{(ij)}(\omega) \neq S_{\pm}^{(ji)}(\omega)$ [27]. We will consider such an atomic environment in Chap. 3, where the environment-induced interactions of the quantum system will be dominated by a unidirectional surface-plasmon-polariton, and therefore where Eq. (1.29) is required to describe the open-system dynamics.

On the other hand, the environments of Chaps. 2 and 4 are reciprocal, and having $\Gamma_{\text{em/abs}}^{(ij)}(\omega) = \Gamma_{\text{em/abs}}^{(ji)}(\omega)$ and $S_{\pm}^{(ij)}(\omega) = S_{\pm}^{(ji)}(\omega)$ leads to the following well-known interaction-

picture master equation

$$\boxed{\frac{d\rho_S(t)}{dt} = -\frac{i}{\hbar}[H_{\text{shift}} + H_\Lambda, \rho_S(t)] + \mathcal{D}_{\text{em}}[\rho_S(t)] + \mathcal{D}_{\text{abs}}[\rho_S(t)]}. \quad (1.30)$$

In this expression, we have introduced the two following terms:

$$H_{\text{shift}} = \hbar \sum_i \left(S_+^{(ii)}(\omega_0) \sigma^{(i)\dagger} \sigma^{(i)} + S_-^{(ii)}(\omega_0) \sigma^{(i)} \sigma^{(i)\dagger} \right), \quad (1.31)$$

$$H_\Lambda = \hbar \sum_{i \neq j} \Lambda^{(ij)}(\omega_0) \sigma^{(i)\dagger} \sigma^{(j)}, \quad (1.32)$$

with $\Lambda^{(ij)}(\omega) = S_+^{(ij)}(\omega) + S_-^{(ji)}(\omega)$. The operator H_{shift} describes the energy shift associated to the qubits energy levels mentioned above. In the following, they will usually be small with respect to the qubits energy ($S_\pm^{(ii)}(\omega_0) \ll \omega_0$), such that we will neglect them, or equivalently, directly include them in the definition of the qubits free Hamiltonian ($H_S \equiv H_S + H_{\text{shift}}$). Moreover, H_Λ corresponds to the coherent environment-mediated dipole-dipole interactions between each pair of qubits. We note that this Hamiltonian commutes with the qubits free Hamiltonian $[H_S, H_\Lambda] = 0$. In addition to these two terms, we have also introduced in Eq. (1.30) the dissipative terms $\mathcal{D}_{\text{em/abs}}$, which encapsulate all the processes of photon emission/absorption of the quantum system, defined by

$$\mathcal{D}_{\text{em}}[\rho_S(t)] = \sum_{i,j} \mathcal{D}_{\text{em}}^{(ij)}(\omega_0)[\rho_S(t)] = \sum_{i,j} \Gamma_{\text{em}}^{(ij)}(\omega_0) \left(\sigma^{(j)} \rho_S(t) \sigma^{(i)\dagger} - \frac{1}{2} \{ \sigma^{(i)\dagger} \sigma^{(j)}, \rho_S(t) \} \right), \quad (1.33)$$

$$\mathcal{D}_{\text{abs}}[\rho_S(t)] = \sum_{i,j} \mathcal{D}_{\text{abs}}^{(ij)}(\omega_0)[\rho_S(t)] = \sum_{i,j} \Gamma_{\text{abs}}^{(ij)}(\omega_0) \left(\sigma^{(j)\dagger} \rho_S(t) \sigma^{(i)} - \frac{1}{2} \{ \sigma^{(i)} \sigma^{(j)\dagger}, \rho_S(t) \} \right), \quad (1.34)$$

with $\{\cdot, \cdot\}$ denoting the anticommutator. Each $\mathcal{D}_{\text{em/abs}}^{(ij)}$ is a super-operator, so-called *Lindblad dissipator*, acting on the qubits reduced density matrix and describing either the local ($i = j$) or non-local ($i \neq j$) process of photon emission/absorption. As a remark, it is possible to diagonalize the matrix formed by the transition rates $\Gamma_{\text{em/abs}}^{(ij)}(\omega_0)$ in order to obtain Eq. (1.30) under a diagonal form in terms of collective qubits operators.

Let us briefly compare the reciprocal and nonreciprocal master equations, namely, Eqs. (1.29) and (1.30). Firstly, it must be pointed out that the processes involving a single qubit are not affected by the reciprocity feature of the environment. Thus, H_{shift} and the local dissipators $\mathcal{D}_{\text{em/abs}}^{(ii)}$ are present in both equations, although we did not express them explicitly in Eq. (1.29) for readability. On the other hand, the environment-induced dipole-dipole interactions and the non-local dissipative terms contribute differently to the qubits dynamics depending on whether the environment is reciprocal or not. For example, some terms present

in the nonreciprocal master equation cancel each other out in the reciprocal case. Finally, we note that in both cases, the Schrödinger picture of the master equation is simply obtained by adding the term $-\frac{i}{\hbar}[H_S, \rho_S(t)]$.

About the validity of the approximations necessary to derive the master equations Eqs. (1.29) and (1.30), following [24, 28], in the next chapters, the different time scales for a transition of frequency ω will be estimated by $\tau_R(\omega) \sim [\Gamma_{\text{em}}^{(ii)}(\omega) + \Gamma_{\text{abs}}^{(ii)}(\omega)]^{-1}$, $\tau_B(\omega) \sim \omega^{-1}$, and $\tau_S(\omega) \sim (2\omega)^{-1}$. In each case, we will consider the set of parameters that produces the ‘worst’ possible scenario with regards to these approximations.

1.2 Energy fluxes

In this section, we will use a quantum thermodynamical approach to investigate the energy exchanges related to the open system. Indeed, the Markovian quantum master equation derived in the previous section allows us to consider the time evolution of observables exclusively related to the open system, the role of the environment being reduced to its correlation functions. This will allow us to introduce, in analogy with classical thermodynamics, the notion of internal energy of the open system, and to derive its time evolution, which will lead us to the concepts of heat and work in the framework of quantum thermodynamics. In addition, we express in terms of heat fluxes the different energy exchanges either between the open system and its environment, or between its subparts. This will help us in the analysis of the systems investigated in Chaps. 2 and 4. In these cases, the qubits environment will be reciprocal, which is why in the present section, we will remain focused on the reciprocal master equation Eq. (1.30). Moreover, for simplicity, the reduced density matrix of the open system will be denoted by $\rho(t)$, rather than by $\rho_S(t)$, and $\text{Tr} \equiv \text{Tr}_S$ will designate the trace over the quantum-system degrees of freedom.

To begin with, we express the internal energy $U(t)$ of the qubits system with the help of its free Hamiltonian,

$$U(t) = \langle H_S \rangle(t) = \text{Tr}(H_S \rho(t)). \quad (1.35)$$

The time variation of internal energy can be induced either by a change of the open-system free Hamiltonian or by the time evolution of the qubits density matrix:

$$\frac{dU(t)}{dt} = \text{Tr}\left(\frac{\partial H_S}{\partial t} \rho(t)\right) + \text{Tr}\left(H_S \frac{d\rho(t)}{dt}\right) = \dot{W} + \dot{Q}, \quad (1.36)$$

where we have introduced the following quantities

$$\dot{W} = \text{Tr}\left(\frac{\partial H_S}{\partial t} \rho(t)\right), \quad \dot{Q} = \text{Tr}\left(H_S \frac{d\rho(t)}{dt}\right), \quad (1.37)$$

which are assimilated to the quantum-mechanical version of work and heat contributions [29–

31], respectively. In analogy with classical thermodynamics, the work contribution is identified as the one not increasing the von Neumann entropy of the system density matrix, which is defined by

$$S(\rho(t)) = -\text{Tr}(\rho(t) \ln [\rho(t)]). \quad (1.38)$$

The reminder of the contributions constitute the heat fluxes. In this framework, Eq. (1.36) constitutes the first law of quantum thermodynamics. In the scenarios considered in the following chapters, the system free Hamiltonian will always be time independent, such that $\dot{W} = 0$. Consequently, the modifications of the system internal energy will only occur through heat fluxes.

By injecting Eq. (1.30) in Eq. (1.36), we obtain

$$\frac{dU(t)}{dt} = -\frac{i}{\hbar} \text{Tr}(H_S[H_\Lambda, \rho(t)]) + \text{Tr}(H_S \mathcal{D}_{\text{em}}[\rho(t)]) + \text{Tr}(H_S \mathcal{D}_{\text{abs}}[\rho(t)]). \quad (1.39)$$

We first note that $\text{Tr}(H_S[H_\Lambda, \rho(t)]) = \text{Tr}([H_S, H_\Lambda]\rho(t)) = 0$, since as pointed out in the previous section $[H_S, H_\Lambda] = 0$. In addition, by considering the dissipative processes related to either a single or a pair of qubit(s), we define the local and non-local superoperators based on Eqs. (1.33) and (1.34):

$$\mathcal{D}_{\text{loc}}^{(i)}[\rho(t)] = \mathcal{D}_{\text{em}}^{(ii)}[\rho(t)] + \mathcal{D}_{\text{abs}}^{(ii)}[\rho(t)], \quad (1.40)$$

$$\mathcal{D}_{\text{nl}}^{(ij)}[\rho(t)] = \mathcal{D}_{\text{em}}^{(ij)}[\rho(t)] + \mathcal{D}_{\text{abs}}^{(ij)}[\rho(t)] + \text{H.c.}, \quad (1.41)$$

such that Eq. (1.39) can be expressed as

$$\frac{d\langle U \rangle(t)}{dt} = \sum_i \text{Tr}(H_S \mathcal{D}_{\text{loc}}^{(i)}[\rho(t)]) + \sum_{i < j} \text{Tr}(H_S \mathcal{D}_{\text{nl}}^{(ij)}[\rho(t)]). \quad (1.42)$$

Each term on the right-hand side of Eq. (1.42) corresponds to a heat flux between the quantum system and the environment. To be more precise, the *local flux* $\dot{Q}_{\text{loc}}^{(i)}(\omega_0)$ characterizes the energy exchanged between the transition of the i -th qubit and the electric field:

$$\boxed{\dot{Q}_{\text{loc}}^{(i)}(\omega_0) = \text{Tr}(H_S \mathcal{D}_{\text{loc}}^{(i)}[\rho(t)]) = \hbar\omega_0 \left(\Gamma_{\text{abs}}^{(ii)}(\omega_0) p_g^{(i)}(t) - \Gamma_{\text{em}}^{(ii)}(\omega_0) p_e^{(i)}(t) \right)}, \quad (1.43)$$

where $p_g^{(i)}(t) = \text{Tr}(\sigma^{(i)} \sigma^{(i)\dagger} \rho(t))$ and $p_e^{(i)}(t) = \text{Tr}(\sigma^{(i)\dagger} \sigma^{(i)} \rho(t))$ are the ground and excited populations of the i -th qubit. The sign of this flux is settled by the competition between photon emission and absorption processes: when it is positive (negative), energy is absorbed (lost) by the transition from (to) the environment, thereby increasing (decreasing) the internal energy of the quantum system. Regarding the other dissipative processes, each of them

involves two qubits and yields a *non-local heat flux*:

$$\dot{Q}_{\text{nl}}^{(ij)}(\omega_0) = \text{Tr}\left(H_S^{(i)} \mathcal{D}_{\text{nl}}^{(ij)}[\rho(t)]\right) = -\hbar\omega_0 \text{Re}[c^{(ij)}(t)] \left(\Gamma_{\text{em}}^{(ij)}(\omega_0) - \Gamma_{\text{abs}}^{(ji)}(\omega_0)\right), \quad (1.44)$$

with $H_S^{(i)} = \hbar\omega_0|e_i\rangle\langle e_i|$, and where $c^{(ij)}(t) = \text{Tr}(\sigma^{(i)\dagger}\sigma^{(j)}\rho(t))$ is the coherence between qubits i and j . Being computed with $H_S^{(i)}$, the flux $\dot{Q}_{\text{nl}}^{(ij)}(\omega_0)$ describes the amount of energy traded by atom i with the environment due to its interaction with atom j . It is important to stress that this collective interaction has the same effect on atom j : $\dot{Q}_{\text{nl}}^{(ij)}(\omega_0) = \dot{Q}_{\text{nl}}^{(ji)}(\omega_0)$. In other words, the amount of energy traded with the environment through this common flux is equally shared between the two qubits: they either both absorb ($\dot{Q}_{\text{nl}}^{(ij)}(\omega_0) = \dot{Q}_{\text{nl}}^{(ji)}(\omega_0) > 0$) or loose ($0 > \dot{Q}_{\text{nl}}^{(ij)}(\omega_0) = \dot{Q}_{\text{nl}}^{(ji)}(\omega_0)$) the same quantity of energy.

In addition to internal-energy variations of the quantum system in its whole, it can be insightful to take into account the energy exchanges occurring between its different subparts, thereby leaving the total internal energy unchanged. In analogy with Eq. (1.35), the internal energy of the i -th qubit² is [32]: $U^{(i)}(t) = \text{Tr}(H_S^{(i)}\rho(t))$, and its time variation can be expressed from Eq. (1.39) by replacing the free Hamiltonian of the quantum system H_S by the one of the single qubit under consideration, $H_S^{(i)}$. This equation leads to the expressions of the local and non-local heat fluxes involving this atom, which stem from the dissipators. Additionally, the fact of having $\text{Tr}(H_S^{(i)}[H_\Lambda, \rho(t)]) \neq 0$ (or alternatively $[H_S^{(i)}, H_\Lambda] \neq 0$) reveals the existence of energy fluxes modifying the internal energy (and entropy) of the subsystem under consideration, but once again, without changing the one of the whole quantum system. These fluxes, the *hopping heat fluxes*, stem from the coherent dipole–dipole interaction mediated by the environment between each pair of qubits. For a generic pair of qubits (i, j) , they read

$$\dot{Q}_{\text{hop}}^{(ij)}(\omega_0) = -\frac{i}{\hbar} \text{Tr}\left(H_S^{(i)}[H_\Lambda, \rho(t)]\right) = -2\hbar\omega_0 \Lambda^{(ij)}(\omega_0) \text{Im}[c^{(ij)}(t)]. \quad (1.45)$$

Having $\dot{Q}_{\text{hop}}^{(ij)}(\omega_0) > 0$ indicates that the internal energy of qubit i is increasing to the detriment of the one of qubit j , such that $\dot{Q}_{\text{hop}}^{(ij)}(\omega_0) = -\dot{Q}_{\text{hop}}^{(ji)}(\omega_0)$.

We stress that the hopping and non-local heat fluxes crucially depend on the quantum coherences between the eigenstates of the system free Hamiltonian: in the absence of these coefficients, both of these fluxes vanish.

1.3 Correlations and other measures

In this section, we briefly introduce miscellaneous mathematical tools that we will use to investigate interactions within the quantum systems under consideration in the following

²As far as these internal energy exchanges are concerned, we will only be interested in subsystems reducing to a single qubit, but we could in principle also consider larger subsystems.

chapters (mainly in Chap. 4).

1.3.1 Bipartite mutual information

Consider a bipartite quantum system, with partitions A and B . The *bipartite mutual information* quantifies the total correlations (classical+quantum) between these two subsystems [33, 34]. It is based on the von Neumann entropy defined in Eq. (1.38). To be more precise, if the state of the composite system is described by the density matrix ρ_{AB} , and if $\rho_{A(B)} = \text{Tr}_{B(A)}(\rho_{AB})$ is the reduced state of the partition A (B), then the bipartite mutual information between A and B is defined by

$$\text{MI}(A : B) = S(\rho_A) + S(\rho_B) - S(\rho_{AB}), \quad (1.46)$$

where $S(\rho_A) + S(\rho_B)$ characterizes the uncertainty (as measured by entropy) on ρ_A and ρ_B treated separately, and where $S(\rho_{AB})$ is the one on the whole system. The bipartite mutual information is a non-negative quantity, which equals zero when the two partitions are uncorrelated, namely, when $\rho_{AB} = \rho_A \otimes \rho_B$. On the other hand, when the composite system is in a maximally-entangled pure state, the reduced states ρ_A and ρ_B are maximally mixed, such that the mutual information is maximized and $\text{MI}_{\max}(A : B) = 2 \ln(\min(d_A, d_B))$, where d_A and d_B are the dimensions of the Hilbert spaces of the subsystems A and B, respectively.

1.3.2 Tripartite mutual information

In the same spirit as for bipartite systems, when considering a quantum system with three partitions A , B , and C , the total correlations between them are given by the *tripartite mutual information* [35, 36]:

$$\tau(A, B, C) = \text{MI}_3(A : B : C) - \mu(A : B : C), \quad (1.47)$$

where $\text{MI}_3(A : B : C) = S(\rho_A) + S(\rho_B) + S(\rho_C) - S(\rho_{ABC})$, and with $\mu(A : B : C) = \max\{\text{MI}(A : B), \text{MI}(A : C), \text{MI}(B : C)\}$. Note that $\tau(A, B, C)$ characterizes the correlations that are genuinely tripartite, in the sense that they cannot be accounted for by considering subsystems of $\{A, B, C\}$.

1.3.3 Trace distance

The *trace distance* is a metric on the space of density matrices. For two density matrices ρ and σ , it is defined by [37]

$$D_t(\rho, \sigma) = \frac{1}{2} \text{Tr} \left(\sqrt{(\rho - \sigma)^\dagger (\rho - \sigma)} \right). \quad (1.48)$$

It belongs to the interval $D_t(\rho, \sigma) \in [0, 1]$, where $D_t(\rho, \sigma) = 0$ if and only if $\rho = \sigma$, while when the two states have orthogonal supports, i.e. when all their eigenvectors with non-zero eigenvalues are orthogonal, then $D_t(\rho, \sigma) = 1$. One of the interests of the trace distance is to provide a measure of state distinguishability [37, 38]: Suppose we consider a system which is either in the state ρ or σ , but we don't know which of the two. The trace distance allows us to know the maximum probability to correctly distinguish between ρ and σ after a single optimal measure, which is given by

$$P = \frac{1}{2}(1 + D_t(\rho, \sigma)). \quad (1.49)$$

When the trace distance between the two states is $D_t(\rho, \sigma) = 1$, we can experimentally distinguish ρ and σ with full certainty ($P = 1$), whereas for $D_t(\rho, \sigma) \simeq 0$, the uncertainty on our state is almost maximum ($P \simeq 1/2$).

1.3.4 Geometric quantum discord

As mentioned previously, the mutual information between two partitions A and B of a quantum system corresponds to the total correlations, thereby encapsulating classical and quantum contributions. One way to determine the quantum contribution is to use the notion of *quantum discord* [34, 39]:

$$D(A \rightarrow B) = \text{MI}(A : B) - \mathcal{C}(A \rightarrow B), \quad (1.50)$$

where $\text{MI}(A : B)$ characterizes the total correlations between A and B [see Eq. (1.46)] and $\mathcal{C}(A \rightarrow B)$ represents the classical contribution to $\text{MI}(A : B)$. Firstly, it is important to stress that unlike the mutual information, D and \mathcal{C} are not symmetric with respect to A and B . Secondly, the quantum discord is generally difficult to compute as determining $\mathcal{C}(A \rightarrow B)$ requires a usually-complicated optimization with respect to POVMs (positive-operator-valued measures) on A . By introducing a metric $g(\cdot, \cdot)$ on the space of states, it is possible to compute the *geometric quantum discord* [39, 40], defined as the distance between the bipartite state under consideration, ρ_{AB} , and its closest classical state χ_{AB} (having only classical correlations):

$$D_G(A, B) = g(\rho_{AB}, \chi_{AB}). \quad (1.51)$$

There exists analytical expressions of D_G in specific configurations, and in particular for the case of a bipartite system having dimensions $2 \times d$ [41], namely, systems composed of a qubit and another subsystem of arbitrary but finite size. One of the most commonly employed metrics of the state space used to compute the geometric discord is the one based on the Bures distance [37].

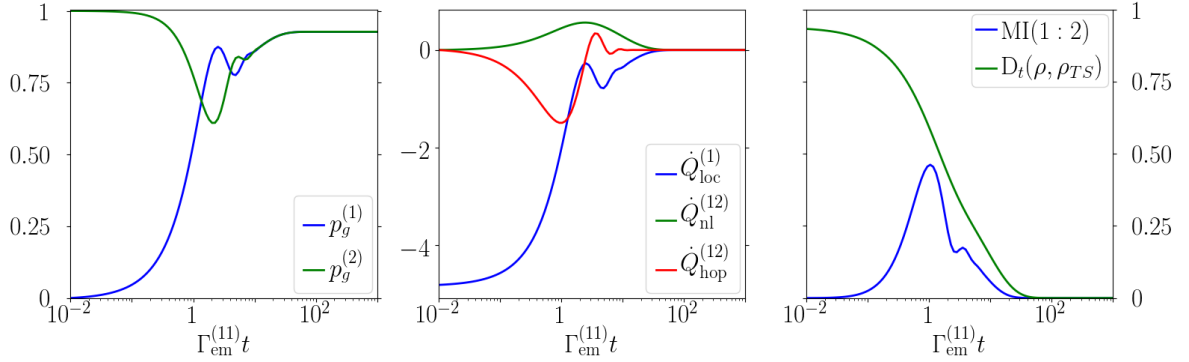


Figure 1.1: Dynamics of the quantum system. Panel(a): Ground-state populations of the two qubits. Panel (b): $\dot{Q}_{\text{loc}}^{(1)}(\omega_0)$ is the local heat flux of the qubit 1, while $\dot{Q}_{\text{nl}}^{(12)}(\omega_0)$ and $\dot{Q}_{\text{hop}}^{(12)}(\omega_0)$ are, respectively, the non-local and hopping fluxes between the two qubits from the perspective of qubit 1. Units: $10^{-20} \text{ J} \cdot \text{s}^{-1}$. Panel (c): Bipartite mutual information between the two qubits, and trace distance between the qubits state and the thermal state at $T = 300 \text{ K}$.

1.4 A basic example

We conclude this chapter by a simple example illustrating the dynamics of an open quantum system described by the reciprocal Markovian quantum master equation Eq. (1.30) derived in Sec. 1.1.

We consider two qubits in free space interacting with a blackbody radiation at $T = 300 \text{ K}$. The qubits have the same atomic transition frequency $\omega_0 = 10^{14} \text{ rad} \cdot \text{s}^{-1}$. The induced dipoles associated to the qubits transitions are assumed to be identical, pointing orthogonally to the line joining the qubits and having magnitudes $|\boldsymbol{\mu}^{(1)}| = |\boldsymbol{\mu}^{(2)}| = |\boldsymbol{\mu}| = 10^{-30} \text{ C} \cdot \text{m}$. The distance separating the qubits is $a = 3 \mu\text{m}$. We will consider similar physical configurations in Chap. 2 but with more than two qubits. The Hamiltonian of the total system is

$$H_{\text{tot}} = H_S + H_E + H_{\text{int}}, \quad (1.52)$$

where H_S and H_E are the qubits and electric-field free Hamiltonian, respectively, and H_{int} is the Hamiltonian of interaction between the qubits and the electric field. To be more explicit, we have

$$H_S = \hbar\omega_0(|e_1\rangle\langle e_1| + |e_2\rangle\langle e_2|) = \hbar\omega_0(\sigma^{(1)\dagger}\sigma^{(1)} + \sigma^{(2)\dagger}\sigma^{(2)}). \quad (1.53)$$

In the framework of Markovian open quantum systems, the Hamiltonian dynamics of the environment will be neglected, such that explicit knowledge of H_E is not required. In the

dipole approximation, the interaction Hamiltonian is

$$H_{\text{int}} = - \sum_{i=1}^2 \mathbf{D}^{(i)} \cdot \mathbf{E}(\mathbf{r}_i) = - \sum_{i=1}^2 \left(\boldsymbol{\mu}^{(i)} \sigma^{(i)} + \boldsymbol{\mu}^{(i)} \sigma^{(i)\dagger} \right) \cdot \mathbf{E}(\mathbf{r}_i). \quad (1.54)$$

The parameters of the present set up have been chosen based on typical parameters from Chap. 2, where we show that the Born-Markov and rotating-wave approximations can be applied. Consequently, the master equation Eq (1.30) can be used to describe the dynamics of the qubits reduced density matrix, denoted by $\rho(t)$:

$$\frac{d\rho(t)}{dt} = -\frac{i}{\hbar} [H_{\Lambda}, \rho(t)] + \mathcal{D}_{\text{em}}[\rho(t)] + \mathcal{D}_{\text{abs}}[\rho(t)], \quad (1.55)$$

where H_{shift} has been neglected, and where we have:

$$H_{\Lambda} = \Lambda^{(12)}(\omega_0) \sigma^{(1)\dagger} \sigma^{(2)} + \Lambda^{(21)}(\omega_0) \sigma^{(1)} \sigma^{(2)\dagger}, \quad (1.56)$$

$$\mathcal{D}_{\text{em/abs}}[\rho(t)] = \sum_{i,j=1}^2 \mathcal{D}_{\text{em/abs}}^{(ij)}[\rho(t)]. \quad (1.57)$$

Equation (1.55) can be written in a slightly more explicit form with the help of Eqs. (1.40) and (1.41):

$$\frac{d\rho(t)}{dt} = -i[H_{\Lambda}, \rho(t)] + \mathcal{D}_{\text{loc}}^{(1)}[\rho(t)] + \mathcal{D}_{\text{loc}}^{(2)}[\rho(t)] + \mathcal{D}_{\text{nl}}^{(12)}[\rho(t)]. \quad (1.58)$$

The expressions of the coefficients entering into play in the dynamics of the quantum system stem in the present case from the correlation functions of blackbody radiation at $T = 300$ K in free space, whose expression is well-known [26]. Introducing the quantities $\tilde{r} = \omega_0 |\mathbf{r}_1 - \mathbf{r}_2|/c$ and $\gamma_0 = |\boldsymbol{\mu}|^2 \omega_0^3 / 3\hbar\pi\epsilon_0 c^3$, the local dissipative rates read

$$\Gamma_{\text{em}}^{(11)}(\omega_0) = \Gamma_{\text{em}}^{(22)}(\omega_0) = [1 + n(\omega_0, T)]\gamma_0, \quad \Gamma_{\text{abs}}^{(11)}(\omega_0) = \Gamma_{\text{abs}}^{(22)}(\omega_0) = n(\omega_0, T)\gamma_0, \quad (1.59)$$

where $n(\omega, T) = (\exp(\hbar\omega/k_B T) - 1)^{-1}$ is the mean number of thermal photons at frequency ω and temperature T . The non-local dissipative rates are

$$\Gamma_{\text{em}}^{(12)}(\omega_0) = \Gamma_{\text{em}}^{(21)}(\omega_0) = [1 + n(\omega_0, T)]\gamma_0\alpha(\tilde{r}), \quad \Gamma_{\text{abs}}^{(12)}(\omega_0) = \Gamma_{\text{abs}}^{(21)}(\omega_0) = n(\omega_0, T)\gamma_0\alpha(\tilde{r}), \quad (1.60)$$

where we defined

$$\alpha(\tilde{r}) = \frac{3}{2\tilde{r}^3} (\tilde{r} \cos(\tilde{r}) + [\tilde{r}^2 - 1] \sin(\tilde{r})).$$

The strength of the coherent dipole-dipole interaction is

$$\Lambda^{(12)}(\omega_0) = \Lambda^{(21)}(\omega_0) = -\frac{3}{4} \frac{\gamma_0}{\tilde{r}^3} [(\tilde{r}^2 - 1) \cos(\tilde{r}) - \tilde{r} \sin(\tilde{r})], \quad (1.61)$$

and we point out that unlike the transition rates, this quantity does not depend on the field temperature T . We note that the coefficients $\Lambda^{(ij)}(\omega_0)$ and $\Gamma_{\text{em/abs}}^{(ij)}(\omega_0)$ with $i, j \in \{1, 2\}$ defined above are particular cases of the more general Eqs. (2.6), (2.7) and (2.8) introduced in Chap. 2.

Figure 1.1(a) shows the dynamics of the qubits ground-state populations $p_g^{(1)}(t)$ and $p_g^{(2)}(t)$ for an initial state $|\psi(0)\rangle = |e_1 g_2\rangle$, i.e. with qubit 1 in its excited state ($p_g^{(1)}(0) = 0$) and qubit 2 in its ground state ($p_g^{(2)}(0) = 1$). At the beginning of the evolution, they exhibit an oscillatory behavior which has a decreasing amplitude, until both populations equal each other. After that, they tend together to their stationary value, which in this case is given by the Boltzmann distribution: $p(\omega) = e^{-\hbar\omega/k_B T}/Z$, where Z is the partition function. Notice that during the oscillation period, the local maxima of one population correspond to the local minima of the other, which suggests a coherent energy exchange between the qubits. This is confirmed by Fig. 1.1(b) showing some of the heat fluxes involved in the system. To be more precise, one sees that the hopping flux $\dot{Q}_{\text{hop}}^{(12)}(\omega_0)$, stemming from the field-mediated coherent dipole–dipole interaction between qubits 1 and 2, has a dynamics very similar to the one of the populations. In particular, at the beginning of the evolution $\dot{Q}_{\text{hop}}^{(12)}(\omega_0) < 0$, indicating that qubit 1 is yielding energy to qubit 2 ($\dot{Q}_{\text{hop}}^{(21)}(\omega_0) = -\dot{Q}_{\text{hop}}^{(12)}(\omega_0) > 0$), which is why the ground-state population of the latter decreases (i.e. its excited population increases). This energy transfer goes on with a decreasing amplitude until $\dot{Q}_{\text{hop}}^{(12)}(\omega_0) = 0$, and after that, we have $\dot{Q}_{\text{hop}}^{(12)}(\omega_0) > 0$: it is now the qubit 2 that is transferring energy to the benefit of qubit 1. As explained previously, this coherent interaction continues until the populations equal each other, in which case the hopping flux vanishes. As a witness of the interactions between the qubits, the bipartite mutual information $\text{MI}(1 : 2)$ is displayed in Fig. 1.1(c). Initially, the qubits are uncorrelated such that $\text{MI}(1 : 2) = 0$. When they start interacting, the mutual information immediately increases, with an intensity reflecting the hopping flux amplitude, where in particular the local maxima of $\text{MI}(1 : 2)$ occur at the same times as the local extrema of $\dot{Q}_{\text{hop}}^{(12)}$. After that, when the interaction between qubits vanishes, they decorrelate from each other and $\text{MI}(1 : 2) = 0$ again.

The damped coherent oscillations of the populations are due to the dissipative processes. Indeed, the local flux of qubit 1, illustrated in Fig 1.1(b), shows that this qubit is dissipating energy into the environment ($\dot{Q}_{\text{loc}}^{(1)}(\omega_0) \leq 0$), and this is also the case for qubit 2 (not shown here). On the other hand, the non-local flux between these qubits is such that $\dot{Q}_{\text{nl}}^{(12)}(\omega_0) = \dot{Q}_{\text{nl}}^{(21)}(\omega_0) > 0$: the atomic pair is collectively drawing energy from the environment through this heat flux, but not enough to fully balance the energy lost through the local fluxes. Eventually, at stationarity, the dissipative fluxes vanish, and the mean energy exchanged between the open system and its environment is zero.

The trace distance $D_t(\rho, \rho_{\text{TS}})$ between the qubits reduced density matrix and the thermal state $\rho_{\text{TS}} = \exp(-\frac{H_S}{k_B T})/Z$ at $T = 300 \text{ K}$ is shown in Fig. 1.1(c). Initially, the quantum system is far from the thermal state, but under the effect of energy dissipation, it gets closer

and closer to it, until they become equal when $D_t(\rho, \rho_{\text{TS}}) = 0$. This clearly illustrates the thermalization of the quantum system to the equilibrium thermal state at the temperature of the environmental electric field.

Energy transport in atomic chains in a thermal environment

Contents

2.1	Introduction	17
2.2	Physical system	19
2.2.1	Relevant parameters of the system	19
2.3	Mathematical description of the system	20
2.3.1	Master equation	20
2.3.2	Definition of energy-transport efficiency	22
2.4	Long-range transport and efficiency amplification	23
2.5	Preliminary investigations	25
2.6	Steady-state analysis	27
2.7	Dynamics	32
2.8	Chains with more atoms	38
2.9	Conclusion	40

2.1 Introduction

Finding new methods to efficiently transport energy within molecular or atomic systems is a key ingredient for future technologies, such as quantum-computing processing or photovoltaic cells [42]. To this end, a number of physical systems have been investigated, many of them being based on the coupling between emitters (e.g. molecules or atoms) and tailored electromagnetic modes. This is typically realized when emitters are located within optical cavities [43, 44], or close to metallic surfaces such as mirrors [45], or nanospheres [46]. Moreover, some investigations found inspiration from natural systems such as light-harvesting photosynthetic complexes [11, 47], which transport energy with high efficiency. Remarkably, it has been shown that these systems exhibit long-living excitonic quantum coherences [8–10]. These observations have drawn a considerable attention, and a number of studies have suggested

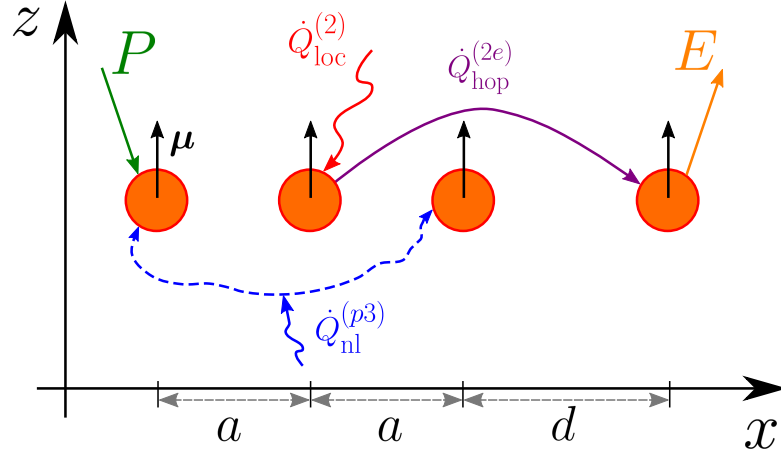


Figure 2.1: Physical system under investigation in this chapter: atomic chain embedded in an electromagnetic field at temperature T . The interactions between the environmental field and the atoms open different channels of energy exchange, either between the quantum system and its environment or within the chain. Moreover, to evaluate the energy-transport efficiency of the chain, energy is pumped into the first atom and extracted from the last one through the fluxes P and E , respectively. The atoms are labeled with increasing x as $\{p, 2, \dots, N-1, e\}$, where p denotes the atom of pumping, and e the extraction atom.

that the energy-transport process occurring in these complexes could result from the interplay between quantum coherent transfer of excitations and environment-induced dissipation, a mechanism called environment-assisted quantum transport (ENAQT) [17, 48–57]. In this spirit, the role of temperature on energy transport of thermal photons has been investigated in Ref. [58] for bi- and tri-dimensional open systems composed of a few two-level quantum emitters (‘atoms’). It has been shown that thermally-enhanced nonlocal effects could drastically improve transport efficiency. In particular, it has been demonstrated that in specific configurations, the efficiency can largely surpass 100% and reach 300%.

In this chapter, we focus our investigation of thermal effects on energy transport in the case of unidirectional chains of two-level atoms. We will show that for specific configurations, the transport efficiency can be dramatically amplified, reaching sometimes 1400%. To unveil the origin of this effect, we perform both steady-state and dynamical studies of the heat-flux interplay between the two-level atoms. In addition, we show that the transport range can be up to 8 times larger than in the absence of thermal effects. These investigations are realized for different number of atoms composing the chain. The results presented in this chapter have been published in Ref. [20].

2.2 Physical system

The system we consider in this chapter consists of N identical two-level atoms distributed linearly in free space along the x -axis, as depicted in Fig. 2.1, and embedded in an electromagnetic field at thermal equilibrium at temperature T . Our aim here is to investigate the properties of energy transport within such atomic chains, and to dedicate a particular attention to the role played by the thermal environment in the transport process.

The figure of merit we will use throughout this chapter is the energy-transport efficiency. The mathematical definition of this quantity will be given further, but we can already provide the underlying idea: energy is artificially pumped at one edge of the chain, and extracted from the other edge. The efficiency stems from the comparison between these two amounts of energy.

2.2.1 Relevant parameters of the system

Before entering the heart of the subject and giving the mathematical description of the problem, let us first briefly discuss the physical parameters of the system that are relevant, and introduce several assumptions that will be valid throughout this work.

First of all, we will assume that all the atoms have the same transition frequency ω_0 . This parameter will be varied in the following investigations but its typical value is of the order of $\omega_0 \sim 10^{14} \text{ rad} \cdot \text{s}^{-1}$ ($\nu_0 \sim 16 \text{ THz}$, $\lambda_0 \sim 19 \mu\text{m}$), that is near the far-infrared region of the electromagnetic spectrum. This corresponds to a temperature of $\hbar\omega_0/k_B \sim 764 \text{ K}$. Being interested in the energy transport related to thermal effects, working with higher frequencies would necessitate unrealistic environmental temperatures (e.g. $1.8 \times 10^4 \text{ K}$ for a wavelength of 800 nm).

To each atomic transition is associated a transition dipole moment $\boldsymbol{\mu}$, which will be as well considered identical for all atoms in the chain. We set arbitrarily both its direction, that we choose orthogonal to the one of the chain, i.e., $\boldsymbol{\mu} = |\boldsymbol{\mu}|\hat{\mathbf{z}}$, and its magnitude $|\boldsymbol{\mu}| = 10^{-30} \text{ C} \cdot \text{m}$.

Another important parameter is the geometrical configuration of the chain. Indeed, we will see that the interaction between two atoms depends on their spatial separation. This is also a parameter that will be changed during our investigations, but the configuration of reference will be a regular chain with step a , with typical value $a = 0.1 \mu\text{m}$. In this case, the length of the chain is $L = (N - 1)a$.

Last but not least, the temperature T of the electromagnetic field embedding the atomic chain is an essential parameter. Once again, although this parameter will be varied during our analysis, two main regimes will be considered: low temperature ($T = 10 \text{ K}$) and room temperature ($T = 300 \text{ K}$).

2.3 Mathematical description of the system

2.3.1 Master equation

Let us now turn to the model describing the time evolution of the system. By calling H_S and H_E the atomic chain and environment bare Hamiltonians, respectively, the Hamiltonian of the total system reads

$$H_{\text{tot}} = H_S + H_E + H_{\text{int}}, \quad (2.1)$$

where H_{int} is the Hamiltonian describing the interaction between the quantum system and the environment. The ground and excited states of the i -th qubit are noted by $|g_i\rangle$ and $|e_i\rangle$, respectively, and the corresponding lowering operator is $\sigma_i = |g_i\rangle\langle e_i|$. The system Hamiltonian then reads $H_S = \sum_{i=1}^N \hbar\omega_0\sigma_i^\dagger\sigma_i$, whereas the interaction Hamiltonian is given in the framework of the dipole approximation by $H_{\text{int}} = -\sum_{i=1}^N(\sigma_i^\dagger + \sigma_i)\boldsymbol{\mu} \cdot \mathbf{E}(\mathbf{r}_i)$. The derivation of the Markovian quantum master equation Eq. (1.30) described in Chap. 1 can be applied here. Regarding the validity of the approximations for the Born-Markov and rotating-wave approximations, the environment decay time is $\tau_B = \omega_0^{-1} = 10^{-14}$ s, and the intrinsic time scale is $\tau_S \sim (2\omega_0)^{-1} \sim 5 \times 10^{-15}$ s. Among the configurations we will consider, the one generating the smallest relaxation time scale occurs when the environmental temperature is $T = 1000$ K, leading to $\tau_R \sim 10^{-1}$ s, such that $\tau_R \gg \tau_B$ and $\tau_R \gg \tau_S$ are both verified. Besides, being interested in the energy transport from one edge of the chain to the other, we introduce incoherent energy pumping on the first atom, atom p , and extraction from the N -th atom, noted by e . Consequently, the time evolution of the reduced density matrix of the atomic chain $\rho(t)$ is

$$\frac{d\rho(t)}{dt} = -\frac{i}{\hbar}[H_\Lambda, \rho(t)] + \mathcal{D}_{\text{em}}[\rho(t)] + \mathcal{D}_{\text{abs}}[\rho(t)] + \mathcal{D}_{\text{in}}[\rho(t)] + \mathcal{D}_{\text{out}}[\rho(t)], \quad (2.2)$$

where the dissipators \mathcal{D}_{in} and \mathcal{D}_{out} represent the pumping and extraction processes. To be more specific, the pumping on atom p is

$$\mathcal{D}_{\text{in}}[\rho(t)] = \Gamma_{\text{in}} \left(\sigma_p^\dagger \rho(t) \sigma_p - \frac{1}{2} \{ \sigma_p \sigma_p^\dagger, \rho(t) \} \right), \quad (2.3)$$

with $\sigma_p = \sigma_1$, whereas the extraction on atom e is

$$\mathcal{D}_{\text{out}}[\rho(t)] = \Gamma_{\text{out}} \left(\sigma_e \rho(t) \sigma_e^\dagger - \frac{1}{2} \{ \sigma_e^\dagger \sigma_e, \rho(t) \} \right), \quad (2.4)$$

where $\sigma_e = \sigma_N$, and Γ_{in} and Γ_{out} being the rates of pumping and extraction, respectively. In this chapter, these rates will be fixed at $\Gamma_{\text{in}} = 10^{-3}\gamma_0$ and $\Gamma_{\text{out}} = 10^2\gamma_0$. These values will remain the same throughout this chapter. They have been chosen based on previous works attempting to reproduce the environment of natural physical systems realizing photosynthesis, where the interplay between coherent quantum dynamics and environmental-induced

dissipation seems to play a fundamental role in the energy transport [58].

The other contributions to this master equation (H_Λ , \mathcal{D}_{em} and \mathcal{D}_{abs}) stem from the interaction between the EM field and each atom in the chain. This interaction produces an effective field-induced Hamiltonian coupling [H_Λ , see Eq. (1.32)] between pairs of atoms thanks to the self-correlation of the field at two distinct points in space. In addition, dissipation of atomic energy into the field is accounted for by the terms \mathcal{D}_{em} and \mathcal{D}_{abs} [Eqs. (1.33) and (1.34)]. More precisely, environmental properties are taken into account through the coefficients $\Lambda^{(ij)}(\omega_0)$, $\Gamma_{\text{em}}^{(ij)}(\omega_0)$ and $\Gamma_{\text{abs}}^{(ij)}(\omega_0)$, respectively. Again, since no ambiguity is possible regarding the transition frequency, we will drop the notation showing the explicit dependence on ω_0 , e.g. $\Lambda^{(ij)}(\omega_0) \rightarrow \Lambda^{(ij)}$. Before giving the expression of these coefficients, we introduce the following notations for a given atomic couple (j, k) :

$$\begin{aligned} \mathbf{r}_{jk} &= \mathbf{r}_k - \mathbf{r}_j, & \hat{\mathbf{r}}_{jk} &= \frac{\mathbf{r}_{jk}}{|\mathbf{r}_{jk}|}, \\ \tilde{r}_{jk} &= \frac{\omega_0}{c} |\mathbf{r}_{jk}|, & \hat{\boldsymbol{\mu}} &= \frac{\boldsymbol{\mu}}{|\boldsymbol{\mu}|}. \end{aligned} \quad (2.5)$$

The strength of the unitary dynamics in free space between atoms j and k with identical dipoles is

$$\begin{aligned} \Lambda^{(jk)} &= -\frac{3}{4}\gamma_0 \left[2(\hat{\boldsymbol{\mu}} \cdot \hat{\mathbf{r}}_{jk})^2 f(\tilde{r}_{jk}) + (1 - (\hat{\boldsymbol{\mu}} \cdot \hat{\mathbf{r}}_{jk})^2) g(\tilde{r}_{jk}) \right], \\ f(x) &= \frac{\cos x + x \sin x}{x^3}, \quad g(x) = \frac{(x^2 - 1) \cos x - x \sin x}{x^3}. \end{aligned} \quad (2.6)$$

These coefficients depend on the interatomic separation and dipoles orientations. On the other hand, they are independent of the electromagnetic-field temperature.

The rates of spontaneous emission and absorption of photons into/from the field associated to the dissipative processes \mathcal{D}_{em} and \mathcal{D}_{abs} are

$$\Gamma_{\text{em}}^{(jk)} = \gamma^{(jk)} [1 + n(\omega_0, T)], \quad (2.7)$$

$$\Gamma_{\text{abs}}^{(jk)} = \gamma^{(jk)} n(\omega_0, T), \quad (2.8)$$

where

$$\gamma^{(jk)} = \gamma_0 \sum_{l=x,y,z} ([\hat{\boldsymbol{\mu}}]_l)^2 \alpha_l^{(jk)}, \quad (2.9)$$

with l denoting the three Cartesian components, and where we used

$$\alpha_x^{(jk)} = \frac{3}{\tilde{r}_{jk}^3} \left(\sin \tilde{r}_{jk} - \tilde{r}_{jk} \cos \tilde{r}_{jk} \right), \quad (2.10)$$

$$\alpha_y^{(jk)} = \alpha_z^{(jk)} = \frac{3}{2\tilde{r}_{jk}^3} \left(\tilde{r}_{jk} \cos \tilde{r}_{jk} + (\tilde{r}_{jk}^2 - 1) \sin \tilde{r}_{jk} \right). \quad (2.11)$$

As mentioned before, in our system the atoms are aligned along the x -axis, such that only the terms $\alpha_x^{(jk)}$ will contribute to the rates. It is worth stressing that unlike $\Lambda^{(jk)}$, these rates do depend on the temperature through the thermal factor $n(\omega_0, T)$. In the limiting case of a field in the vacuum state, that is in the absence of thermal photons ($n(\omega_0, T) = 0$), the quantum system cannot absorb energy from the environment ($\Gamma_{\text{abs}}^{(jk)} = 0$), and thus its interaction with the field is exclusively reduced to spontaneous emission. As expected, the presence of thermal photons both provides the possibility to absorb energy from the field and triggers the additional process of stimulated emission.

2.3.2 Definition of energy-transport efficiency

As mentioned before, we need to quantify the fraction of the extracted energy which is due to the presence of pumping, and, to do so, we begin by quantifying how much energy can be extracted when the pumping is not present.

Therefore we consider a first situation, the so-called no-pumping scenario, where only extraction is performed. The corresponding density matrix of the chain $\rho_0(t)$ is solution to Eq. (2.2) after having set $\Gamma_{\text{in}} = 0$ (while $\Gamma_{\text{out}} \neq 0$). The corresponding energy flux extracted from the last atom is

$$E_0(t) = -\text{Tr}(H_{\text{sys}}\mathcal{D}_{\text{out}}[\rho_0(t)]). \quad (2.12)$$

The minus sign present in this definition has been added so that $E_0(t)$ is a positive quantity, which describes the amount of energy extracted. Having $E_0(t) \neq 0$ implies that energy is extracted from the system despite the absence of pumping. As mentioned before, this typically occurs when thermal effects are non-negligible, providing the chain with the possibility to absorb thermal energy from the field. The second case is the pumping scenario, where both pumping and extraction are performed ($\Gamma_{\text{in}} \neq 0$ and $\Gamma_{\text{out}} \neq 0$). By calling $\rho(t)$ the density matrix associated to this configuration, the pumping and extraction fluxes are respectively

$$P(t) = \text{Tr}(H_S\mathcal{D}_{\text{in}}[\rho(t)]), \quad E(t) = -\text{Tr}(H_S\mathcal{D}_{\text{out}}[\rho(t)]). \quad (2.13)$$

The definition of energy-transport efficiency directly stems from these three energy fluxes, and reads

$$\chi(t) = \frac{E(t) - E_0(t)}{P(t)}. \quad (2.14)$$

Note that we are comparing *energy fluxes* rather than energies. Having $E(t) = E_0(t) + P(t)$ ($\chi(t) = 1$) suggests that the energy is effectively transported along the chain without any loss, namely with 100% of efficiency. On the other hand, if the extraction flux is the same whether pumping is performed or not ($E(t) = E_0(t)$), it can be considered that the pumped energy has been totally lost to the environment or stored in the system but has never reached

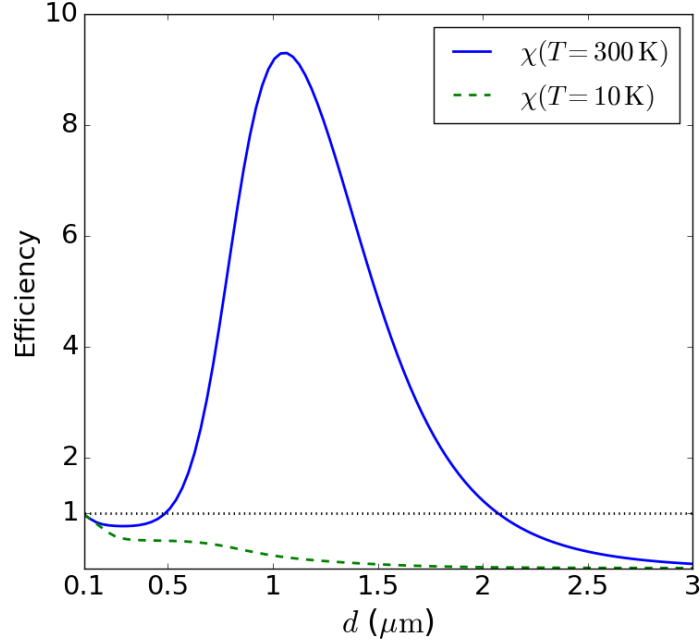


Figure 2.2: Energy-transport efficiency as a function of the distance between the last two atoms of a four-atom chain.

atom e .

2.4 Long-range transport and efficiency amplification

Let us begin our investigation on transport efficiency with a system of $N = 4$ atoms of transition frequency $\omega_0 = 10^{14} \text{ rad} \cdot \text{s}^{-1}$, regularly distributed with a constant step $a = 0.1 \text{ } \mu\text{m}$. The atoms are labeled $\{p, 2, 3, e\}$. We will start focusing on the energy transport at the steady state of the system and therefore consider only stationary quantities (unless specified otherwise), such that we drop the explicit time dependence, e.g., $\chi = \lim_{t \rightarrow \infty} \chi(t)$.

We investigate here how the energy transport is affected when the atom of extraction, i.e., the last one of the chain, is moved along the x -axis. The energy-transport efficiency corresponding to this simulation is shown in Fig. 2.2. The displacement of the extraction atom is described by the parameter d characterizing the distance between atoms $N - 1$ and N , that is between atoms 3 and e in this case. The regular chain disposition corresponds to $d = a$. Besides, being interested in thermal effects on energy transport, we analyze this displacement for two different thermal configurations: at low temperature ($T = 10 \text{ K}$) and at room temperature ($T = 300 \text{ K}$).

At low temperature, there being no thermal photons ($n(\omega_0, 10) \simeq 0$), the EM field is close to its vacuum state. In this case, no thermal energy is available in the atomic environment

($\Gamma_{\text{abs}}^{(ij)} = 0$) and pumping is thus the only process increasing the energy of the quantum system. For this reason, in the absence of pumping, no energy is extracted from the chain ($E_0 = 0$). Concerning the other energy channels, the strength of the hopping fluxes ($\Lambda^{(ij)}$) is independent of the temperature, and the rates of emission reduce to $\Gamma_{\text{em}}^{(ij)} = \gamma^{(ij)}$, such that both types of fluxes, hopping and emission, are contributing in this low-temperature regime. This implies that the pumped energy can either be transmitted within the chain or lost to the environment, such that the relation $0 \leq \chi \leq 1$ holds, and therefore the transport efficiency depends on the competition between energy transmission and energy loss. This can be seen in Fig. 2.2: when $d \sim a$, the hopping fluxes are dominant. The major amount of the pumped energy is transported to the extraction atom, while the effects related to the dissipative fluxes are negligible. This leads to $\chi \sim 1$. When d increases, however, the strength of the hopping fluxes between atoms 3 and 4 weakens, progressively reducing the amount of energy transmitted between them, until it completely vanishes when $d \geq 2\mu\text{m}$. In this case, the extraction atom cannot interact with the rest of the chain, where the pumped energy remains trapped and then ends up by being dissipated, resulting in $\chi = 0$.

At $T = 300\text{ K}$ the EM field is not in the vacuum state since the mean number of thermal photons is not negligible, having for effect to boost the interactions between the quantum system and its environment. On the one hand, the chain absorbs thermal photons present in EM field with rates $\Gamma_{\text{abs}}^{(ij)}$, and having $E_0 > 0$ is very likely. On the other hand, the loss of energy is also enhanced ($\Gamma_{\text{em}}^{(ij)} = \gamma^{(ij)}(1 + n(\omega_0, 300))$). In this case, having a good efficiency does not rely on the bare competition between energy-transmission and energy-loss, as in the low-temperature configuration. Indeed, pumping energy into atom p causes modifications in all the quantum-system energy-exchange processes: hopping, emission and absorption (the latter being active only when T is large enough, as is the case, e.g., at $T = 300\text{ K}$). A good efficiency then requires that these interactions modified due to pumping lead to an enhanced amount of energy extracted from atom e in comparison to the no-pumping scenario. Figure 2.2 clearly shows that the behavior of the transport efficiency is radically different from the low-temperature regime, although the regular-chain configuration ($d = a$) also leads to $\chi \sim 1$. When d increases, even though the hopping fluxes between atoms 3 and 4 are weak in comparison to the emission ones, the efficiency overcomes the low-temperature upper bound, and can reach values up to ~ 9 times greater. This means that the energy extracted from the chain remarkably surpasses the one pumped in by almost one order of magnitude.

In addition to being interesting per se, this effect of efficiency amplification occurs within a wide interval of d , therefore considerably extending the range of energy-transport. For example, comparing with the low-temperature regime, producing $\chi \simeq 1$ at $T = 10\text{ K}$ necessitates a regular-chain configuration, thus limiting the transport to a distance of $L = 3 \times 0.1 = 0.3\mu\text{m}$. At room temperature, on the other hand, this can be achieved either with a regular chain or with a chain of length $L = 2 \times 0.1 + 2.2 = 2.4\mu\text{m}$, which is 8 times larger than in the low-temperature regime. Besides, the smooth variation of χ within the efficiency-amplification

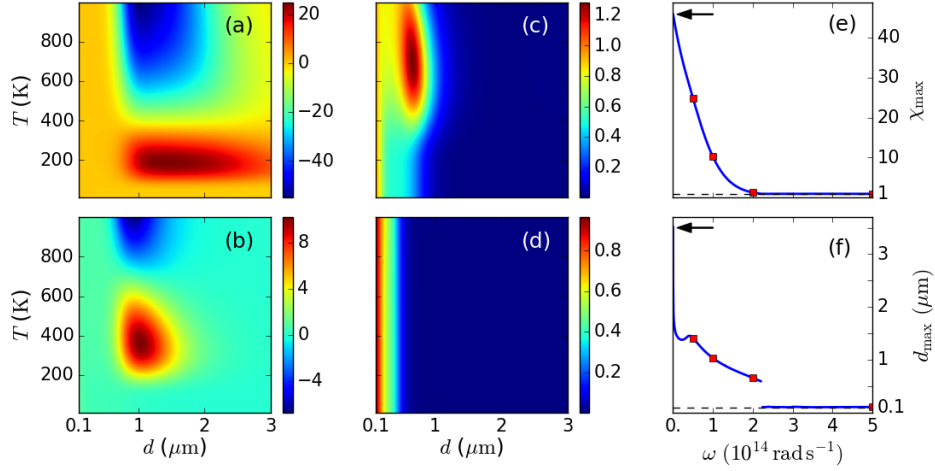


Figure 2.3: Panels (a)-(d): Efficiency as a function of the distance d between atoms $N - 1$ and N (with $N = 4$), and of the environmental temperature T . The atomic transition ω_0 takes the values 0.5, 1, 2 and 5 (units of $10^{14} \text{ rad} \cdot \text{s}^{-1}$) in panels (a), (b), (c) and (d), respectively. Panel (e): Maximum efficiency with respect to $d \in [0.1, 3] \mu\text{m}$ and $T \in [10, 1000] \text{ K}$ as a function of ω_0 . Panel (f): Value of d , noted d_{max} , producing the best efficiency as a function of ω_0 . In panels (e) and (f), the red squares correspond to panels (a)-(d), and the black arrows represent the asymptotic limit when $\omega_0 \ll 10^{14} \text{ rad} \cdot \text{s}^{-1}$.

interval makes it robust against small variations of d . Regarding energy transport and its practical realization, these properties of long range and robustness make this physical system more advantageous at room temperature than at low temperature. Indeed, working at $T = 10 \text{ K}$ necessitates a very specific atomic distribution, which can be hardly achievable experimentally, and produces at best $\chi = 1$. On the other hand, at room temperature, less precision is required on the atomic positions, and obtaining $\chi > 1$ is achievable for a large number of configurations.

2.5 Preliminary investigations

In the aim of getting more insight on the efficiency amplification, we explore the dependence of this phenomenon on the variation of several relevant parameters, still at stationarity. More specifically, Figs. 2.3(a-d) show a density plot of χ as a function of the distance between atoms 3 and e , and of the EM-field temperature, each panel corresponding to a different atomic transition frequency.

The first thing to point out is the difference of the efficiency-variation scale between each panel. Indeed, when $\omega_0 = 0.5 \times 10^{14} \text{ rad} \cdot \text{s}^{-1}$, depending on the couple of parameters (d, T) , the interval of efficiency variation is $[-40, 20]$, whereas it is reduced to $\chi \in [0, 1]$ for

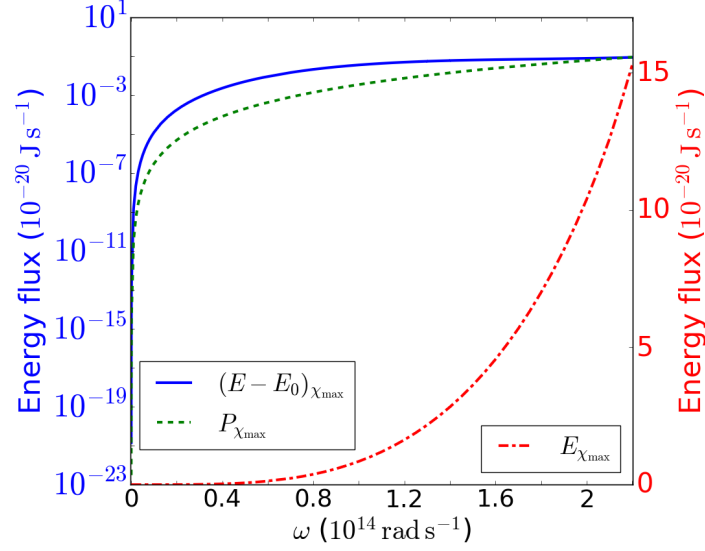


Figure 2.4: Left scale: Difference between the energies extracted with and without pumping (solid blue line) and pumping (dashed green line), which produce the maximum efficiency shown in Fig. 2.3(e). Right scale: Energy extracted in the presence of pumping (dash-dotted red line) in correspondence with the left scale.

$\omega_0 = 5 \times 10^{14} \text{ rad} \cdot \text{s}^{-1}$. Although some configurations result in $\chi < 0$, we will remain focused on the ones producing $\chi > 0$ since the analysis we are pursuing is dedicated to increasing the efficiency of energy transport. For the atomic transition frequency $\omega_0 = 0.5 \times 10^{14} \text{ rad} \cdot \text{s}^{-1}$ [Fig. 2.3(a)], the mean number of thermal photons is non-negligible for a large number of $T \in [10, 1000] \text{ K}$. Within this range of temperatures, the variation of $n(\omega_0, T)$ is considerable and induces in turn a strong sensitivity of the efficiency with respect to T at this frequency [Fig. 2.3(a)]. With the frequency increasing, the minimum temperature necessary to have considerable thermal effects rises, leading to a shift of the high-efficiency regions towards high temperatures [Figs. 2.3(b-c)]. Finally, the mean number of thermal photons at $\omega_0 = 5 \times 10^{14} \text{ rad} \cdot \text{s}^{-1}$ is negligible for all the temperatures in the interval considered here, and therefore pulling away the N -th atom in such environments [Fig. 2.3(d)] or in a field in vacuum state is similar. In such cases, the maximum value of efficiency is $\chi \simeq 1$ and is reached when the chain is regularly distributed ($d = a$), and then monotonically decreases toward 0 when increasing d .

This analysis is generalized with Fig. 2.3(e), which shows the maximum efficiency χ_{\max} with respect to $(d, T) \in [0.1, 3] \mu\text{m} \times [10, 1000] \text{ K}$, as a function of the atomic transition frequency. Clearly, χ_{\max} decreases with the increase of ω_0 , that is with the disappearance of thermal effects in the environment. Finally, the frequencies are too high for the presence of notable thermal effects within the considered interval of temperatures, leading to the vacuum-state-field regime, characterized by $\chi_{\max} \simeq 1$ with $d = a$. The black arrow corresponds to the

asymptotic value of χ_{\max} when $\omega_0 \ll 10^{14} \text{ rad} \cdot \text{s}^{-1}$, which reaches the remarkable value of 40.

Investigating the dependence of χ on the distance between atoms $N - 1$ and e reveals that the efficiency amplification is not only a thermal effect, but also geometrical. Indeed, we just showed that the high-efficiency region is shifted toward high temperatures when ω_0 increases. In addition, this shift is accompanied by a shrinking of these regions with respect to the parameter d . Besides, as shown in Fig. 2.3(f), when ω_0 is increased, the distance d_{\max} producing the best efficiency is reduced, and eventually reaches the regular-configuration value $d_{\max} = a$. The discontinuity visible at $\omega_0 \sim 2.2 \times 10^{14} \text{ rad} \cdot \text{s}^{-1}$ reflects the transition between the configuration where $\chi_{\max} > 1$ for a given $d_{\max} > a$, to the one where $\chi_{\max} = 1$ and $d_{\max} = a$ represent the best possible scenario. Note that in the latter case there is still a region of $d > a$ where the efficiency slightly increases, but such that $\chi < 1$. This is illustrated in Fig. 2.2, where a small bounce of χ at $T = 10 \text{ K}$ is visible around $d \sim 0.7 \mu\text{m}$. Once again the black arrow indicates the limiting case $\omega_0 \ll 10^{14} \text{ rad} \cdot \text{s}^{-1}$.

Figure 2.4 displays the fluxes entering into play in the definition of efficiency [Eq. (2.14)] as a function of ω_0 . The values shown here are the one producing the maximum efficiency shown in Fig. 2.2. It can be seen that the additional energy extracted from the chain in the presence of pumping can be of several orders of magnitude larger than the one pumped in. Also, note that in the limit $\omega_0 \ll 10^{14} \text{ rad} \cdot \text{s}^{-1}$, although having $\chi \sim 40$ is remarkable, the fluxes involved here are rather small.

2.6 Steady-state analysis

This section is dedicated to the steady-state analysis of the energy-transport efficiency. To be more specific, we will study the interplay between the energy fluxes occurring either within the quantum system or between the chain and its environment, and elucidate the mechanism inducing the efficiency amplification discussed previously.

We begin our analysis with Fig. 2.5, where the last atom of the chain is pulled away, similarly to Fig. 2.2, but for several values of N . Not surprisingly, the best values of efficiency reached in the low-temperature regime are produced by the regular-chain configuration, and never exceed 1. More remarkably, at room temperature, the efficiency amplification only occurs in the case of a four-atom chain, revealing that this effect results from a very specific balance of the interplay between the energy fluxes.

Before going further, let us briefly recall the different heat fluxes entering into play, which have been introduced in Chap. 1. The hopping fluxes ($\dot{Q}_{\text{hop}}^{(ij)}$) describe energy exchanges between two atoms and do not change the total energy of chain. The local fluxes ($\dot{Q}_{\text{loc}}^{(i)}$) result from the sum of both photon absorption and emission processes, which stem from the interactions between a single atomic transition and the environment. On the other hand, the non-local fluxes ($\dot{Q}_{\text{nl}}^{(ij)}$) are associated with the interaction between an atomic couple and the

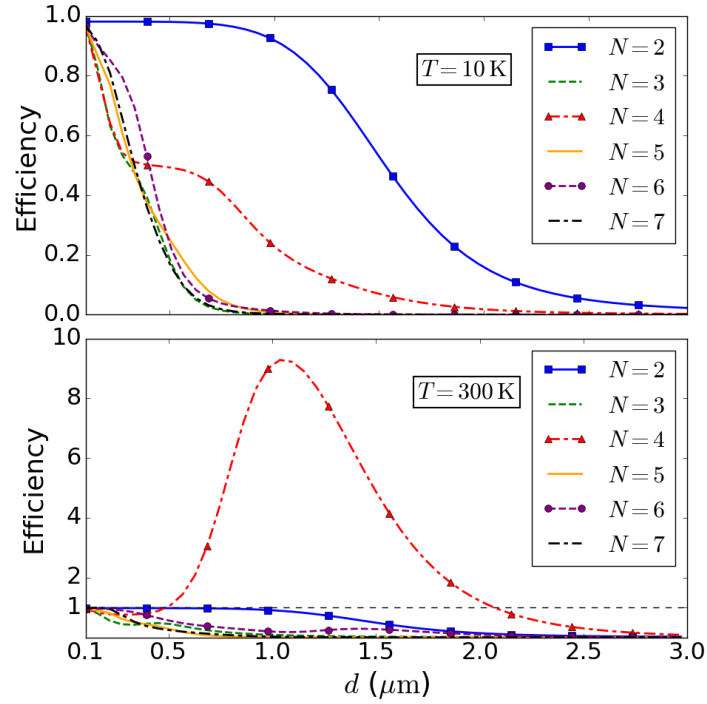


Figure 2.5: Efficiency as a function of the distance between atoms $N - 1$ and N for chains with different number of atoms. The environmental temperature is $T = 10\text{ K}$ (upper panel) and $T = 300\text{ K}$ (lower panel). The configuration $N = 4$ is the one presented in Fig. 2.2.

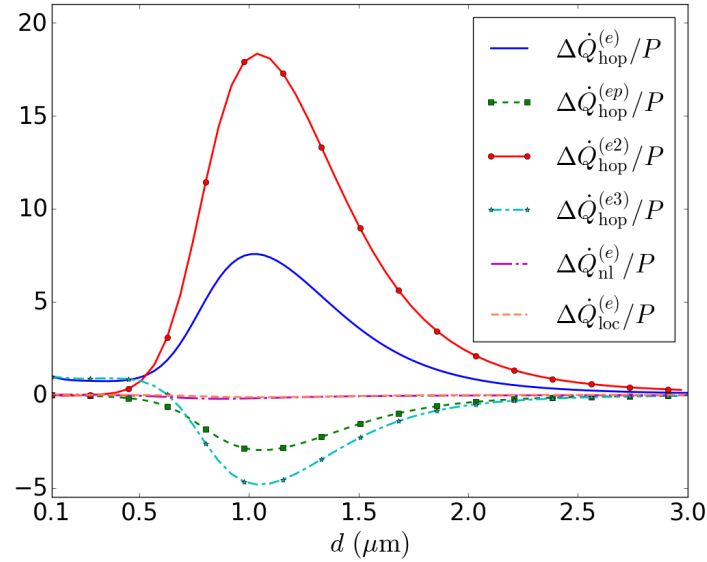


Figure 2.6: Global differences for each type of energy flux involving atom e [Eq. (2.16)] as a function of the distance between atoms 3 and e . Additionally, the contributions of each atom to $\Delta\dot{Q}_{\text{hop}}^{(e)}$ are shown as well.

environment. Similarly to the local fluxes, they result from the balance between emission and absorption of energy by the couple. The amount of energy exchanged between the atomic pair and the field is the same for the two atoms, i.e., each of them either receives or loses half of the energy.

In order to highlight the role played by each of these fluxes in both the pumping and no-pumping scenarios, instead of working with bare energy fluxes, we will rather use *differences of energy fluxes* between the pumping and no-pumping scenarios, as follows

$$\Delta\dot{Q}_{\text{loc}}^{(j)} = \dot{Q}_{\text{loc}}^{(j)} - \dot{Q}_{\text{loc},0}^{(j)}, \quad \Delta\dot{Q}_{\varphi}^{(jk)} = \dot{Q}_{\varphi}^{(jk)} - \dot{Q}_{\varphi,0}^{(jk)}, \quad (2.15)$$

where here the local flux concerns atom j and the hopping ($\varphi = \text{“hop”}$) and non-local ($\varphi = \text{“nl”}$) fluxes involve atoms j and k . Then, the global difference of hopping (non-local) fluxes involving the j -th atom reads

$$\Delta\dot{Q}_{\varphi}^{(j)} = \sum_{k \neq j} \Delta\dot{Q}_{\varphi}^{(jk)}. \quad (2.16)$$

Note that in the following, most of the time these differences will be normalized by the pumping flux P .

Let us now use these quantities to investigate the efficiency amplification occurring in the four-atom chain. The following figures have been realized at $T = 361$ K, because in this case, the maximum efficiency ($\chi = 10.2$) is even higher than at $T = 300$ K. Although we do not explicitly plot the efficiency as a function of d for $T = 361$ K, its behavior is extremely similar to the one at $T = 300$ K, shown in Fig. 2.2, which can safely be used as reference in the following. In this figure, it is worth stressing that the efficiency is always positive within the whole interval of d , implying that the energy extracted from the chain in the presence of pumping is larger than without pumping ($E > E_0$). This leaves two possibilities concerning the origin of the additional energy ($E - E_0$): it is either absorbed by atoms ($p, 2, 3$) (by pumping or environmental interactions) and transmitted to the extraction atom, or absorbed directly by the latter from the field. To determine this, Fig. 2.6 shows the global differences of each type of flux involving the extraction atom ($\Delta\dot{Q}_{\text{loc}}^{(e)}$, $\Delta\dot{Q}_{\text{nl}}^{(e)}$ and $\Delta\dot{Q}_{\text{hop}}^{(e)}$) as a function of d at $T = 361$ K. The difference $\Delta\dot{Q}_{\text{hop}}^{(e)}$ follows a behavior very similar to the one of χ in Fig. 2.2, and having $\Delta\dot{Q}_{\text{loc}}^{(e)} \sim \Delta\dot{Q}_{\text{nl}}^{(e)} \sim 0$ leads us to conclude that the additional energy is absorbed by the chain (atom e excluded) and transmitted exclusively by hopping to the extraction atom. A further step is to unveil the origin of this extra energy. A hint is given by the different contributions to $\Delta\dot{Q}_{\text{hop}}^{(e)}$, i.e., each $\Delta\dot{Q}_{\text{hop}}^{(ei)}$ such that $i \neq e$, are also shown in Fig. 2.6. One can see that having $d \sim a$ induces $\Delta\dot{Q}_{\text{hop}}^{(e)} \sim \Delta\dot{Q}_{\text{hop}}^{(e3)} \sim P$, indicating that atom e receives an amount of energy close to P by hopping from its nearest neighbor, that is atom 3. The rest of the hopping fluxes are negligible. When d increases, however, the distribution of hopping fluxes changes significantly, and two distinct behaviors emerge. On the one hand, both differences $\Delta\dot{Q}_{\text{hop}}^{(ep)}$ and $\Delta\dot{Q}_{\text{hop}}^{(e3)}$ become negative, signifying that atoms p and 3 yield less

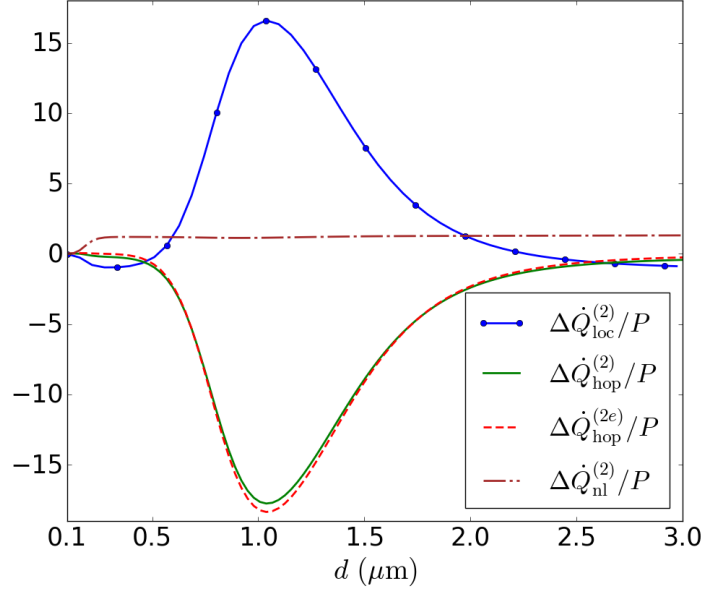


Figure 2.7: Global difference of each type of flux involving atom 2 as a function of the distance between the last two atoms of the chain. The hopping flux between atoms 2 and e is also shown. It appears clear that the main contribution to $\Delta\dot{Q}_{\text{hop}}^{(2)}$ comes from the interaction between this atomic pair. This quantity is plotted in Fig. 2.6 from the perspective of atom e , which explains the opposite sign between the two curves (i.e., $\Delta\dot{Q}_{\text{hop}}^{(e2)} = -\Delta\dot{Q}_{\text{hop}}^{(2e)}$).

energy to atom e in the presence of pumping than in its absence. On the other hand, a drastic enhancement in the energy flowing from atom 2 to atom e arises. This huge increase is such that $\Delta\dot{Q}_{\text{hop}}^{(e2)} + \Delta\dot{Q}_{\text{hop}}^{(ep)} + \Delta\dot{Q}_{\text{hop}}^{(e3)} > 0$: in the pumping case, although atoms p and 3 transmit less energy to the extraction atom, this deficit is overwhelmed by the increase of the hopping flux originating from atom 2, such that $E > E_0$ which leads to $\chi > 0$. Besides, in most of these cases, the additional energy is larger than P , resulting in $\chi > 1$. This suggests that the pumping induces a modification of the fluxes distribution such that the quantum system, and in particular the triplet $(p, 2, 3)$, absorbs energy from the environment. Consequently, the rest of the analysis is declined in two steps: on the one hand, we will focus on atom 2, and on the other hand, on the atomic pair $(p, 3)$.

Firstly, we start with Fig. 2.7, which shows the same quantities as in Fig. 2.6, but related to atom 2, that is $\Delta\dot{Q}_{\text{loc}}^{(2)}$, $\Delta\dot{Q}_{\text{nl}}^{(2)}$ and $\Delta\dot{Q}_{\text{hop}}^{(2)}$. The peculiar flux $\Delta\dot{Q}_{\text{hop}}^{(2e)}$ is pictured as well. The analysis will be focused on the region $d > 0.4 \mu\text{m}$. Consistently with the previous observations, it can be seen that in the pumping case, atom 2 yields more energy to e than in the no-pumping scenario since $\Delta\dot{Q}_{\text{hop}}^{(2e)} < 0$ (recall that $\Delta\dot{Q}_{\text{hop}}^{(2e)} = -\Delta\dot{Q}_{\text{hop}}^{(e2)}$). This loss, however, is compensated by a significant increase of the energy absorbed by atom 2 from the environment, mainly through local flux, but also, to a lesser extent, by non-local flux. Secondly, concerning the atomic pair $(p, 3)$, Fig. 2.8 shows the local fluxes of these two atoms, as well as their shared

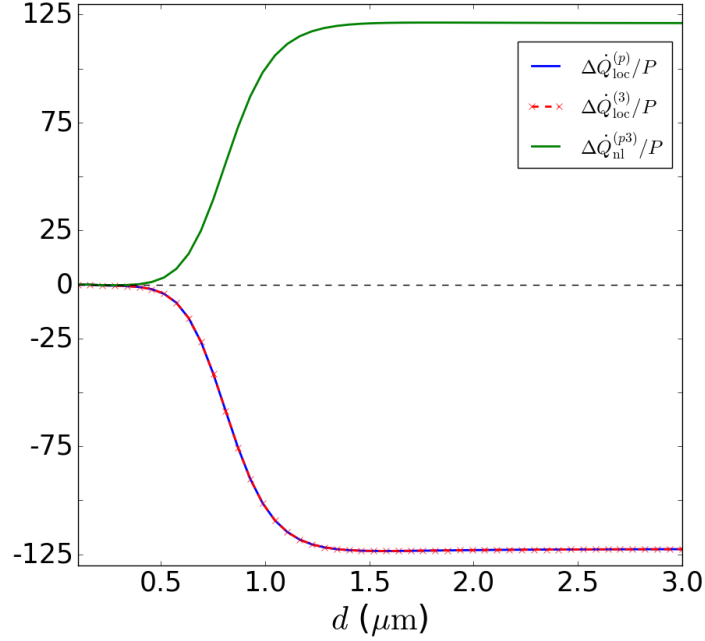


Figure 2.8: Difference of local and non-local fluxes related to atoms p and 3 as a function of the distance between atoms 3 and e . The rise of these flux differences coincides with the amplification of the efficiency ($\chi \geq 1$).

non-local flux. In the region of efficiency amplification, and in the presence of pumping, a collective behavior arises between these two atoms: they absorb energy cooperatively through their non-local flux. Although this energy income is counter-balanced by their individual local fluxes, this collective behavior privileges the interactions between these two atoms, and at the same time, reduces the interactions between each of them and the rest of the atoms not belonging to this couple. Consequently, atom 2 gets isolated (in terms of interactions with its neighbors), providing it with the possibility to interact more with both its environment and the extraction atom. Then, the atomic triplet $(p, 2, 3)$ functions as an excitation injector: the cooperation of atoms p and 3 induced by pumping has for effect to single out atom 2 , allowing it to absorb more thermal energy from the environment, and to transmit it to the extraction atom via hopping. In such cases, the energy extracted at the end of the chain has potentially two contributions: the energy pumped in, which is (partially) transmitted along the chain, and the energy injected by the triplet $(p, 2, 3)$ by the thermal environment.

Synthesizing the previous observations, two different regimes can be identified depending on the geometry of the chain. Within the range $d \in [0.1, 0.4] \mu\text{m}$ the regular-transmission regime occurs. It is characterized by the fact that most of (if not all) the extracted energy originates from the pumping and $\chi \leq 1$. In this case, the transport is realized by hopping from an atom to its neighbor, from one edge of the chain to the other. The hopping strength being independent of the temperature, this regime can exist at any T , including $T = 0 \text{ K}$,

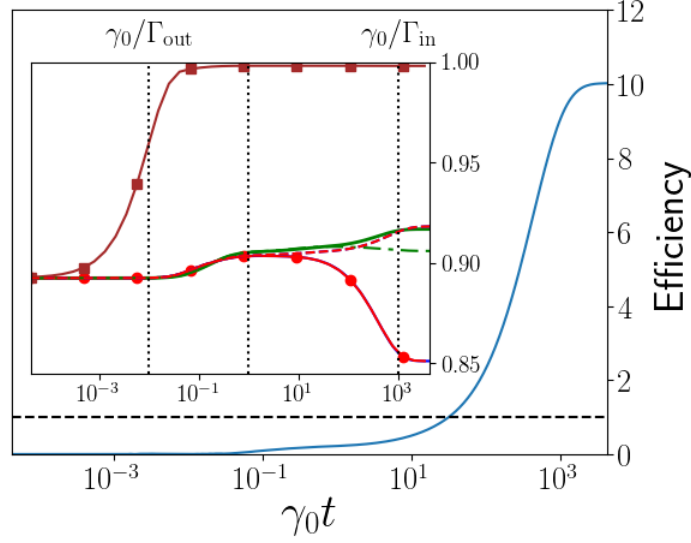


Figure 2.9: Main part: Dynamics of the energy-transport efficiency. Inset: Dynamics of the ground state populations of each atom. These populations, noted $p^{(i)}(t)$ ($p_0^{(i)}(t)$) for the i -th atom in the presence (absence) of pumping, are obtained from the reduced density matrix $\rho^{(i)}(t)$ ($\rho_0^{(i)}(t)$). The correspondence between curves and populations are the following. Solid brown line with squares: $p^{(e)}$; solid red line $p^{(p)}$; dash-dotted red line: $p_0^{(p)}$; solid green line with circles: $p^{(2)}$; dashed green line: $p_0^{(2)}$. The curves of $p_0^{(e)}$, $p^{(3)}$ and $p_0^{(3)}$ are superimposed with $p^{(e)}$, $p^{(p)}$ and $p_0^{(p)}$, respectively.

when the field is in the vacuum state. When $d > 0.4 \mu\text{m}$, the excitation-injector regime dominates. In this regime, the extraction atom is spatially isolated, and the atomic triplet $(p, 2, 3)$ plays the role of excitation injector described above. This mechanism results from the competition between two opposite requirements: on the one hand, the excitation injector needs to be isolated as much as possible, otherwise the interactions with the extraction atom redistribute the fluxes and destroy the effect. On the other hand, since a large amount of the energy absorbed by atom 2 is transmitted to atom e via hopping, then the distance between them must not be too large, otherwise the strength of the interaction vanishes. This regime being based on the absorption of thermal energy from the environment, it cannot be realized with a field in the vacuum state. However, it allows energy transport over a much larger range than the other regime, in addition to the drastic efficiency amplification.

2.7 Dynamics

In the previous section, we have analyzed the energy-transport efficiency as a function of the chain geometry. This analysis was performed at stationarity, and it emerged that in some cases, the atomic triplet $(p, 2, 3)$ induces an amplification of the efficiency. In the following,

we will focus our attention on this mechanism by fixing the chain geometry, and investigate the efficiency dynamics. This will allow us to have a deeper insight on the establishment of the interplay between different kinds of fluxes that gives birth to the excitation injector.

Throughout this section, the system of reference will be a four-atom chain with the temperature of the electromagnetic field fixed at $T = 361$ K. The distance between two neighboring atoms is $a = 0.1 \mu\text{m}$, except the one between atoms 3 and e , which is $d = 1.03 \mu\text{m}$. The stationary energy-transport efficiency of this chain is $\chi = 10.2$, and its time evolution is depicted in Fig. 2.9. Moreover, to have a global insight on the energy distribution dynamics, the inset of this figure shows the ground state populations of each atom as a function of time, both in the presence (solid lines) and in the absence (dashed lines) of pumping.

Before entering into details, it is worth stressing that three time scales enter into play in the dynamics of this system. Each of them corresponds to a different physical process and is characterized by a specific rate: pumping (Γ_{in}), spontaneous relaxation (γ_0) and extraction (Γ_{out}). As mentioned before, we have set $\Gamma_{\text{in}} = 10^{-3}\gamma_0$ and $\Gamma_{\text{out}} = 10^2\gamma_0$, and consequently the effects of each process manifest themselves in the following chronological order: extraction, relaxation, and pumping ($\Gamma_{\text{out}}^{-1} < \gamma_0^{-1} < \Gamma_{\text{in}}^{-1}$). These three time scales are clearly visible on the population dynamics, shown in the inset of Fig. 2.9. At $t = 0$, the initial state of the system is the thermal state, where all the ground state populations, noted $p^{(i)}$ ($p_0^{(i)}$) in the presence (absence) of pumping (with $i \in \{p, 2, 3, e\}$), are equal to each other. The ground state population of the extraction atom is the first one to be affected by the extraction process in both cases, with and without pumping, and rapidly reaches its maximum value for the rest of the dynamics: the extraction maintains atom e close to its ground state. The populations of the other atoms start to change during the time scale associated to the spontaneous relaxation. Within this period ($\sim \gamma_0 t \in [10^{-2}, 1]$), they follow a similar evolution, whether pumping is performed or not. After that, however, there begin to arise differences of two natures. Firstly, focusing on a single scenario, either pumping or no-pumping, the population dynamics can differ from an atom to another. Secondly, for a given atom, the pumping and no-pumping scenarios can induce different dynamics.

To begin our investigation, we will first compare the populations dynamics of each atom in the no-pumping case (dashed lines). In this case, the ground state population of atom 2 is approximately constant starting from $\gamma_0 t \sim 1$. Concerning atoms p and 3, their populations remain close to each other throughout the dynamics ($p_0^{(p)} \simeq p_0^{(3)}$). Until $\gamma_0 t \sim 2 \times 10^2$, their behavior is roughly the same as atom 2, but after that they start increasing, such that at stationarity, the probability of excitation of atom 2 (i.e., $1 - p_0^{(2)}$) is higher than the one of atoms p and 3. Although we are interested in the comparison of this scenario with the pumping case, it is worth noticing that there already appears a similar behavior of atoms p and 3 differing from the one of atom 2. This results from the symmetry of the triplet: atom 2 standing in between atoms p and 3, its interactions with them are equal. On the other

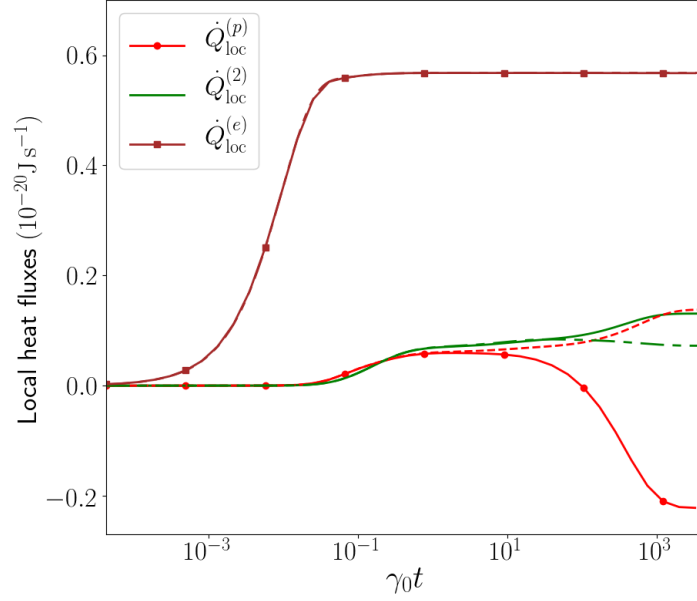


Figure 2.10: Dynamics of the local fluxes of atoms p , 2 and e . The local flux $\dot{Q}_{\text{loc}}^{(3)}$ is not shown because it is superimposed with $\dot{Q}_{\text{loc}}^{(p)}$. Two curves with the same color code are associated to the same atom: the solid lines correspond to the pumping case while their dashed counterparts characterize the no-pumping scenario.

hand, the atomic separations of the couples $(p, 2)$ and $(p, 3)$ ($(3, 2)$ and $(3, p)$) differ, leading to unequal interactions. The positions of atoms p and 3 being symmetric with respect to atom 2, they have identical interactions and therefore their populations are extremely close, but different from the ones of atom 2. Rigorously, the symmetry of the triplet in terms of interactions is broken by the extraction (and pumping) process(es), but most of the time this is negligible.

We now turn to the pumping scenario (solid lines). In this case, although once again the populations of atoms p and 3 stay close to each other ($p^{(p)} \simeq p^{(3)}$), their behavior is radically different from the no-pumping scenario. Indeed, the pumping has for effect to decrease significantly these populations, which reach their stationary value shortly after passing $\gamma_0 t = 10^3$, i.e., the time associated to γ_{in} . On the contrary, the ground state population of atom 2 increases. As a consequence, in comparison to the no-pumping scenario, the atoms p and 3 have their probability of excitation increased, while the one of atom 2 has decreased. Moreover, the hierarchy between atomic populations is reversed, changing from $p_0^{(2)} < p_0^{(p)}, p_0^{(3)}$ to $p^{(2)} > p^{(p)}, p^{(3)}$.

Having now a first glimpse of the atomic-energy-state dynamics, let us turn to the time evolution of the different energy fluxes inducing this dynamics, and as usual, compare the differences between pumping and no-pumping scenarios. The dynamics of the local fluxes

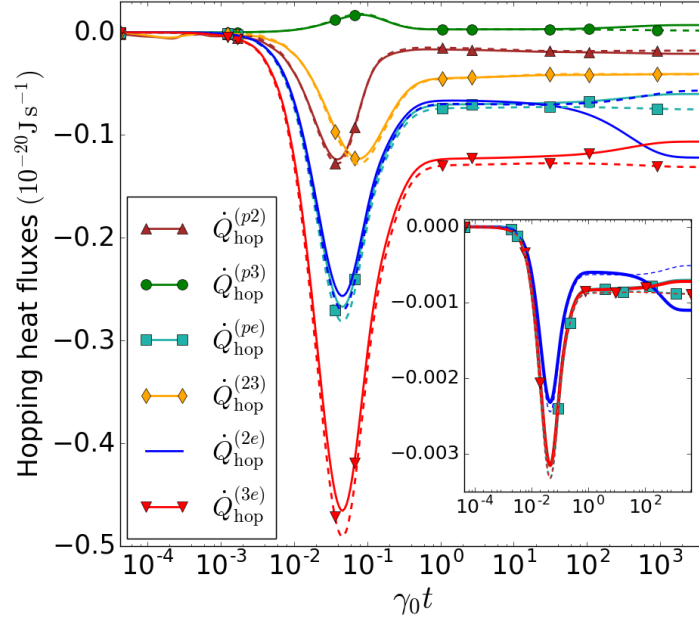


Figure 2.11: Dynamics of the hopping fluxes both in the presence (solid lines) and absence (dashed lines) of pumping. Inset: Dynamics of the imaginary parts of the coherences between the atomic couples $(2, e)$ (solid and dashed blue lines) and $(3, e)$ (solid and dashed red lines), which generate the corresponding hopping fluxes shown in the main part.

shown in Fig. 2.10 are deeply related to the ones of the ground state populations. In particular, it can be seen that each considerable change in the evolution of the populations is related to the successive appearances, firstly, of the extraction flux which occurs very early in the dynamics ($t \sim \Gamma_{\text{out}}^{-1}$), secondly, of the fluxes related to the interactions between the atoms and their environment ($t \sim \gamma_0^{-1}$), and finally, of the pumping flux ($t \sim \Gamma_{\text{in}}^{-1}$). Rigorously, it should be noted that there is actually a supplementary slight modification of the populations in between the regimes of extraction and spontaneous relaxation ($\gamma_0 t \sim 10^{-1}$). This is related to the hopping fluxes, and we will look into it more in detail with Fig. 2.11. Before going further, let us recall that these fluxes are determined by the imaginary parts of the coherences present in the density matrix of the chain. These latter are plotted as an inset of Fig. 2.11, and indeed, it can be seen that they are intimately related to the behavior of the hopping fluxes.

In Fig. 2.11, two intervals can be distinguished in the time evolution of both the main part and the inset. As mentioned before, the first one occurs in between the regimes of extraction and spontaneous relaxation. In the no-pumping scenario, this relaxation leads to a stabilized fluxes distribution. However, in the presence of pumping, during the corresponding time scale, there appears an additional modification of the hopping fluxes distribution. The presence of the peaks in the first region can be interpreted with the help of the atomic ground

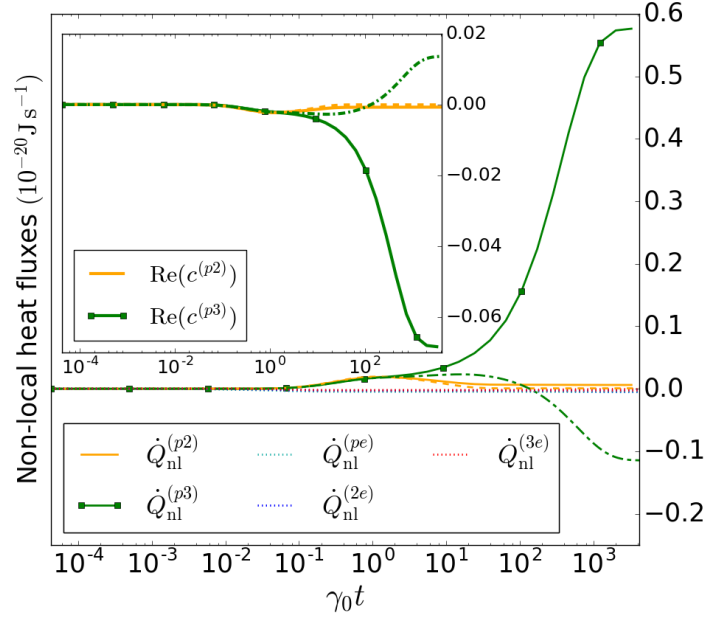


Figure 2.12: Main part: Dynamics of the non-local fluxes of each atomic couples. Two cuves with the same color characterize the same atomic couple, and the solid (dashed) lines indicate the presence (absence) of pumping. Inset: Real parts of the coherences related to the atomic couples $(p, 2)$ (orange lines) and $(p, 3)$ (green lines) from which stem the non-local fluxes displayed in the main part.

state populations in Fig. 2.9. As discussed previously, the system is initially in a thermal state, such that the atomic populations are equally distributed. At this stage, there is no interatomic energy exchange and the imaginary parts of the coherences are non-existent. The manifestation of the extraction process rapidly breaks this homogeneity by forcing atom e to remain poorly excited. As a consequence, in the attempt of bringing back the system to a Gibbs state, the imaginary parts of the coherences arise, inducing hopping fluxes, and thus providing the atoms with the possibility to redistribute the energy uniformly within the chain acting in this respect against the extraction process. Note that the highest peaks (in absolute value) are the ones involving atom e , which is obviously the atom affected the most by the extraction. The amplitude of this effect increases until the evolution enters the time scale related to the spontaneous relaxation processes. At this moment, the energy channel related to the interactions between the system and the environment comes into play. Consequently, the inhomogeneity of the atomic population distribution is even more profound and therefore the balance between hopping fluxes is strongly disrupted. Finally, the effect of pumping begins to appear, and the differences between the two scenarios, with and without pumping, heighten. As expected from the steady-state analysis of the excitation-injector mechanism, the hopping flux between atoms 2 and e is the one the most enhanced, to the benefit of the extraction atom. Moreover, although atoms p and 3 still yield energy to e , this occurs to a

lesser extent.

Regarding the different interactions necessary to the establishment of the excitation-injector mechanism, we still have to investigate the collective interaction between atoms p and 3. To this end, their dynamics is pictured in Fig. 2.12, along with the real part of the relevant coherences (see the inset): as mentioned before [Eq. (1.44)], these coefficients dictate the behavior of the non-local fluxes. The difference between pumping and no-pumping scenarios is striking. In the absence of pumping, the non-local flux arising from the cooperation of atoms p and 3 releases energy into the environment. Pumping energy into the chain has two notable consequences. Firstly, the magnitude of this collective interaction is increased. Secondly, the direction of the energy flow is reversed: the non-local flux increases the energy of the atomic pair instead of decreasing it. Although atoms p and 3 release a large amount of their energy to the field through the local fluxes $\dot{Q}_{\text{loc}}^{(p)}$ and $\dot{Q}_{\text{loc}}^{(3)}$, this is not the case for its totality, and therefore their energy increases. As shown previously, this is also the case for atom 2, which absorbs energy from the field, but there arises a remarkable difference between the pair $(p, 3)$ and atom 2. Indeed, Fig. 2.11 shows that the amount of energy conceded by atom 2 via hopping is increased, meaning that the latter plays the role of an antenna: it absorbs energy from the field and transmits it within the chain. On the contrary, the hopping fluxes of atoms p and 3 decrease in the presence of pumping: instead of transmitting their energy, they rather ‘store’ it, therefore increasing their probability of being in the excited state, as shown in Fig. 2.9 ($1 - p^{(\alpha)} > 1 - p_0^{(\alpha)}$ for $\alpha = p, 3$).

Summarizing, this is what follows from the investigation of the dynamics. Starting from a thermal state where the atomic populations are equally distributed, extraction is performed on the last atom of the chain, which quickly approaches its ground state. Consequently, in the attempt of bringing the system back to an homogeneous population distribution, complex coherences arise, whose imaginary parts induce hopping fluxes allowing interatomic energy exchanges. When the effects of the thermal environment enter into play, a new balance between local, non-local and hopping fluxes is established, until the effect of pumping manifests itself. At this moment, the mechanism of the excitation injector sets up. The individual and collective interactions of atoms p and 3 with the environment strengthen, notably due the increase of the real parts of their coherences. This results in the enhancement of their probability of being in the excited state. In the mean time, atom 2 has more freedom to interact with the field from which it absorbs thermal energy. Despite this absorption, this atom is closer to its ground state than atoms p and 3 because it concedes a considerable amount of its energy to the rest of the chain, and in particular to the extraction atom, therefore increasing the energy extracted from the chain in the presence of pumping, and thus, the energy-transport efficiency.

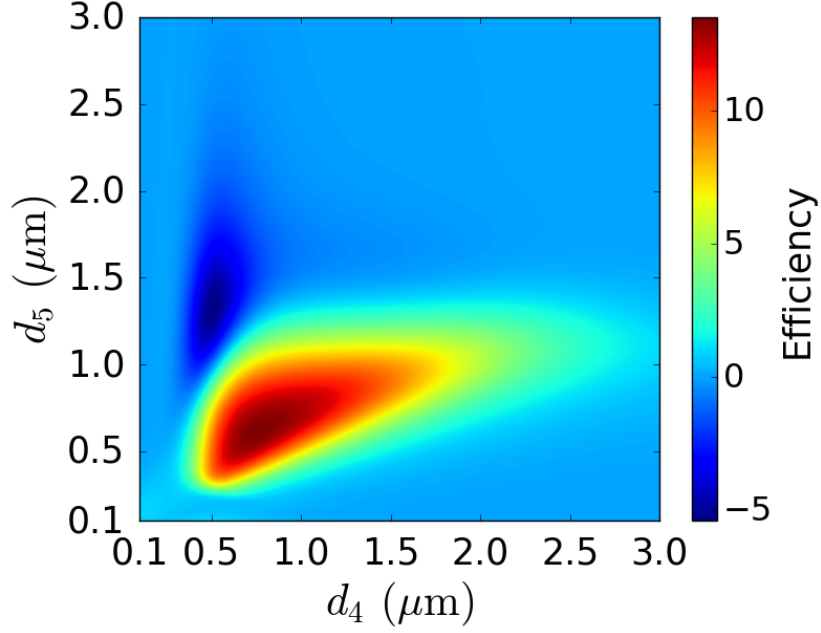


Figure 2.13: Stationary energy-transport efficiency of a five-atom chain as a function of d_4 and d_5 , corresponding to the distance between atoms (3,4) and (4, e), respectively.

2.8 Chains with more atoms

Figure 2.5 showed us that moving away the last atom of the chain produces an amplification of the efficiency only when $N = 4$. After investigating this specific case, we have shown that each atom composing the chain plays an essential role in the energy transport: the atomic triplet $(p, 2, 3)$ acts as an excitation injector and the fourth one is the atom from which energy is extracted. In this section, similarly to Fig. 2.5, we also explore the stationary energy-transport efficiency with $N = 5, 6, 7$, but with different constraints on the geometry of the chain. Having in mind to take advantage of the excitation injector, we keep fixed the positions of atoms $(p, 2, 3)$ by separating them with a step of $a = 0.1 \mu\text{m}$. The degrees of freedom we will explore are the atomic positions of atoms $4, \dots, N$. Moreover, in the following, we will fix $T = 361 \text{ K}$.

We begin our study with a five-atom chain, the atoms being labeled $\{p, 2, 3, 4, e\}$. The stationary transport efficiency is shown in Fig. 2.13 as a function of d_4 and d_5 , denoting the distance between atoms 3 and 4, and the one between 4 and e , respectively. In analogy with the four-atom chain, there is a wide region where the efficiency reaches values greater than 1, suggesting that the excitation injector still plays his role despite the presence of an additional atom. More remarkably, the best value of efficiency reaches $\chi = 13.52$, which is even better than in the case $N = 4$.

Let us continue our investigations with chains of $N = 6$ and $N = 7$ atoms. In these cases,

N	$d_4(\mu\text{m})$	$d_5(\mu\text{m})$	$d_6(\mu\text{m})$	$d_7(\mu\text{m})$	χ
5	0.763	0.618	—	—	13.518
6	0.556	1.076	0.578	—	13.982
	0.782	0.564	0.518	—	13.631
7	0.768	0.581	0.380	0.419	13.908

Table 2.1: Table regrouping the optimized transport efficiencies of N -atom chains ($N > 4$), which has been realized with respect to the atomic positions of atoms $4, \dots, N$ within the interval $[0.1, 2] \mu\text{m}$ by using a genetic algorithm. Each generation of the algorithm is formed of 10^3 individuals. The portion of this population surviving the selection process is the half of it producing the best efficiency, and the portion that is subject to mutation after the mating step is 20% (randomly chosen). Two criteria were chosen to determine the convergence of the algorithm: the relative differences between both the best 20 efficiencies and each couples of the associated positions had to be lower than 10^{-3} (10^{-2} for $N = 7$). For $N \geq 6$, the optimized efficiencies are local maxima, i.e., a set of atomic positions producing an even higher efficiency could exist.

the number of variables is such that the efficiency cannot be plotted similarly to $N = 4$ or $N = 5$, and trying to determine the best efficiency by varying only one or two parameters at a time might be a laborious task. To overcome this, we used a genetic algorithm [59] to determine the optimized values of χ as a function of the atomic positions (the first three atoms still being at a fixed distance $a = 0.1 \mu\text{m}$).

The genetic algorithm is a stochastic optimization process based on Darwin's theory of species evolution. In our case, we identify a species individual as a chain configuration, such that atomic positions can be viewed as genetic code. To initialize the algorithm, a set of individuals is created randomly, thus forming the population of the first generation. Hereafter begins a series of three steps that is repeated generation after generation. Step 1 is the selection process. This is realized with the help of the function to be optimized, in our case the energy-transport efficiency. This function is applied to all the population, and the individuals selected to survive are the ones producing the best values of the function. After that comes step 2: the members of the surviving population are divided in pairs, each of which will play the role of parents. Indeed, the mating of each couple generates two children whose genetic code is based on the ones of their two parents. The step 3 consists in mutating a small portion of the population by randomly modifying its genetic code. From these three steps results a new population mixing parents and offspring, and involving a few mutated members. Applying iteratively these three steps on the successive generations leads to populations more and more refined until convergence toward the global maximum of the function is finally reached.

The results of these optimizations are presented in Tab. 2.1, where it can be seen that,

remarkably, the best efficiency values have improved with respect to the cases $N = 4$ and $N = 5$. Moreover, it is worth stressing that these values correspond to local maxima, meaning that there are potentially other configurations producing equal or even better energy-transport efficiency. Finally, in addition to the improvement of efficiency, the increase of the number of atoms is also accompanied by a widening of the transport range, notably with considerable atomic separations. For example, the case $N = 7$, which produces an efficiency of $\chi \sim 14$, corresponds to a chain of length $L = 2.35 \mu\text{m}$.

2.9 Conclusion

In this chapter, we investigated the energy transport properties of N -atom chains embedded in an electromagnetic field at temperature T . More specifically, we compared how efficiently the chain transports energy when artificial pumping and extraction are performed at each edge of the chain, respectively.

We have shown that for specific geometric configurations, the transport efficiency can be drastically larger than 100%, reaching in some cases 1400%. The investigation of a four-atom chain both at stationarity and during dynamics has allowed us to unveil the mechanism producing such efficiency amplification.

This is due to the atomic triplet $(p, 2, 3)$ which has the role of an excitation injector. More precisely, pumping energy into the system intensifies the interactions of atoms p and 3 with their environment, not only individually, but also collectively: the magnitude of both their local fluxes and their shared non-local flux are considerably enhanced. Although the energy balance between these fluxes does not induce directly a significant modification of the energy extracted, the privileged interaction between these two atoms has for effect to give more freedom to atom 2, on the one hand, to absorb energy from the thermal field, and on the other hand, to transmit energy by hopping to atom e .

The amount of energy extracted from the chain in the presence of pumping has two contributions: the pumped energy that has been transmitted by hopping from an atom to its neighbor, and the energy absorbed by the chain. Within the efficiency-amplification regime, due to the excitation injector, this amount of energy can largely surpass the one of pumped in, leading to an efficiency larger than 100%, and as mentioned previously, sometimes reaching 1400%.

Analyzing the fluxes dynamics in this regime has highlighted the importance of the coherences rising in the chain density matrix. On the one hand, their imaginary parts induce hopping fluxes allowing interatomic energy exchanges. On the other hand, their real parts give birth to the non-local fluxes, and in particular to the one related to the couple $(p, 3)$, whose essential role in the mechanism of efficiency amplification has been discussed above.

An important aspect of the efficiency amplification effect regarding practical realizations are its properties related to the chain geometry. Indeed, there exists a large number of

configurations that produce an efficiency larger than 100%. In addition, the robustness of the efficiency against small displacements of the last atom ensures the possibility to observe this effect despite potential lack of precision on atomic positions due to experimental difficulties. Finally, the range of the efficiency amplification regime offers the possibility to transport energy over considerable distances. For example, we have shown that a regular chain is required to obtain an efficiency of 100% at low temperature, while around room temperature, on the other hand, the same efficiency can be reached with (nonregular) chains up to 8 times larger.

Energy transport in atomic chains close to photonic topological insulators

Contents

3.1	Introduction	43
3.2	Physical system	44
3.3	Generalized master equation and basic example	47
3.4	Transport-efficiency enhancement induced by unidirectional-SPP . .	50
3.5	Practical advantages	52
3.6	Physical insight with two-atom chains	56
3.7	Conclusion	59

3.1 Introduction

Topological insulators (TIs) are materials that have drawn a tremendous attention in the last few years, reaching its paroxysm with the attribution of the Nobel Prize to Thouless, Haldane and Kosterlitz in 2016. One of the main interests of these insulators comes from the existence of chiral edge states crossing the gap between their valence and conduction bands, which are backscattering immune. These singular properties stem from the non-trivial topology of the TIs band structures, and offer a new paradigm in numerous practical applications, ranging from spintronics to quantum information [60].

Analogously to electronic edge states, it has been shown that unidirectional electromagnetic states can exist at the interface of the so-called *photonic topological insulators* (PTIs). Similarly to TIs, these materials are characterized by a photonic band structure of non-trivial topology, generated by materials with either broken time-reversal or inversion symmetry. At the interface between a PTI and a topologically-trivial medium, there can exist unidirectional electromagnetic states protected from backscattering. The existence of these states was firstly predicted in systems involving photonic crystals with broken time-reversal symmetry [61, 62],

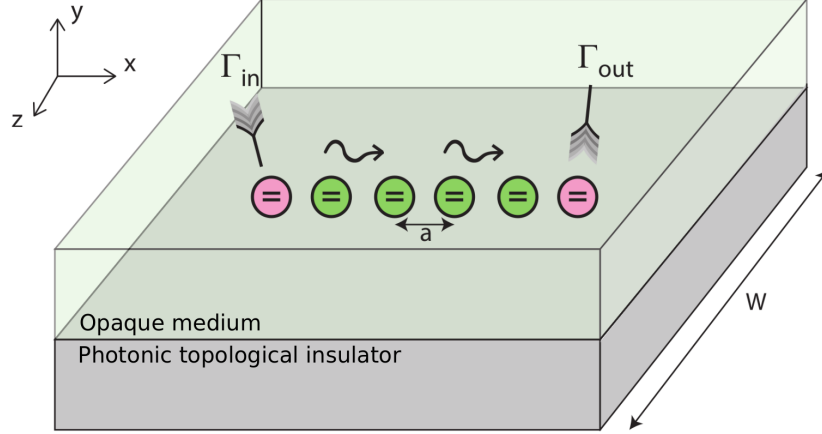


Figure 3.1: Physical system: chain of N two-level emitters located at the interface between a biasable plasma (being a PTI in the presence of biasing field) and an opaque medium ($\epsilon = -2$). The chain step is called a , and the interface width is denoted by W . Energy is pumped into the first atom of the chain and extracted from the last one.

and has been experimentally observed afterwards through different protocols based on periodic structures [63–66]. Furthermore, the existence of such states has been extended to continuous media, e.g., with magnetized plasma [67].

Besides, chiral quantum systems have recently been drawing an increasing attention [68–75]. These are systems where the photon-emission process of quantum emitters (‘atoms’) is anisotropic, which can be used to control interatomic interactions, e.g., in the aim of producing entanglement [68, 70, 71, 73].

In the same spirit as Chap. 2, this chapter will be dedicated to the investigation of energy-transport efficiency along a unidirectional chain of two-level atoms which, in this case, will be located in a nonreciprocal environment. More precisely, the environment will consist of a unidirectional surface-plasmon-polariton (SPP) generated at the interface between a PTI and an opaque medium. We will see that due to unidirectionality, the energy-transport efficiency can be enhanced by one or more orders of magnitude with respect to reciprocal environments. In addition, we will demonstrate the robustness of unidirectional transport against the presence of interface deformation. Moreover, we will also highlight that through the tunability of the SPP reciprocity properties, the energy transport can be controlled to a certain extent. The results of this chapter are presented in Ref. [21].

3.2 Physical system

The system under investigation in this chapter is a chain of N two-level quantum emitters, located at the interface between a biasable plasma and an opaque medium, as illustrated in

Fig. 3.1. The emitters are regularly distributed along the x axis, with a step of a , such that the i -th atom has for position $\mathbf{r}_i = (i-1)a\hat{\mathbf{x}}$. Moreover, they all have the same transition frequency $\nu_0 = \omega_0/2\pi = c/\lambda_0 = 200$ THz, as well as similar transition dipole moment $\boldsymbol{\mu} = |\boldsymbol{\mu}|\hat{\mathbf{y}}$, pointing orthogonally to the interface with a magnitude of $|\boldsymbol{\mu}| = 60$ D. In order to quantify the energy-transport efficiency, energy will be pumped into the first atom, which we call atom p , and extracted from the last one, atom e . The atoms are thus labeled $\{p, 2, \dots, N-1, e\}$. As we will see, the chain energy-transport properties will drastically change depending on the atomic environment, and in particular, on its topological properties.

The description of PTIs is based on the notion of photonic-band-structure topology [61, 62]. To be more specific, the bulk band diagram of a PTI exhibits a band gap, and each of its branches is characterized by a topological invariant, the Chern number. This number is an integer differing from zero when the band topology is non-trivial. This occurs in materials where either time-reversal [64, 76, 77] or inversion [78, 79] symmetry is broken. Then, at the interface between a PTI and another medium with a common band gap, there can exist gap-crossing one-way edge modes. The number of these modes is determined by the difference between the gap Chern numbers of the two media. For each medium, the gap Chern number is obtained by summing the Chern numbers of every branch below the band gap. We note that in the case of two topologically-identical media, the gap Chern numbers are equal, and therefore there is no gap-crossing edge mode. Thus, to observe these modes, the two media must have different topologies. In our system, aside the biasable plasma, which will be treated in the next paragraph, the opaque medium (OM) in the region $y > 0$ is topologically trivial, and characterized by a relative permittivity $\varepsilon = -2$, so that propagation in its bulk is prevented.

When a static magnetic field is applied to the biasable plasma, time-reversal symmetry is broken, thereby generating a non-trivial topology for the bulk band structure, which, in addition, exhibits a band gap. Then, the biased plasma (BP) is a PTI, whereas in the absence of magnetic field, the unbiased plasma (UP) is gap-less and topologically trivial. Let us elaborate a bit more on this. The biasable plasma we will consider throughout this work has a permeability $\mu = 1$, and is characterized by a relative permittivity which varies depending on the presence of a biasing magnetic field, $\mathbf{B} = B_z\hat{\mathbf{z}}$ in our case. This permittivity is an Hermitian tensor

$$\boldsymbol{\varepsilon}(\omega) = \begin{pmatrix} \varepsilon_{11} & \varepsilon_{12} & 0 \\ \varepsilon_{21} & \varepsilon_{22} & 0 \\ 0 & 0 & \varepsilon_{33} \end{pmatrix}, \quad (3.1)$$

having for components

$$\varepsilon_{11} = \varepsilon_{22} = 1 - \frac{\omega_p^2}{\omega^2 - \omega_c^2}, \quad \varepsilon_{33} = 1 - \frac{\omega_p^2}{\omega^2}, \quad \varepsilon_{12} = -\varepsilon_{21} = i \frac{-\omega_c \omega_p^2}{\omega(\omega^2 - \omega_c^2)},$$

where $\omega_c = B_z q_e / m_e$ is the cyclotron frequency induced by the biasing field, and q_e and m_e the electron charge and mass, respectively. Moreover, $\omega_p = N_e q_e^2 / \varepsilon_0 m_e$ is the plasma frequency,

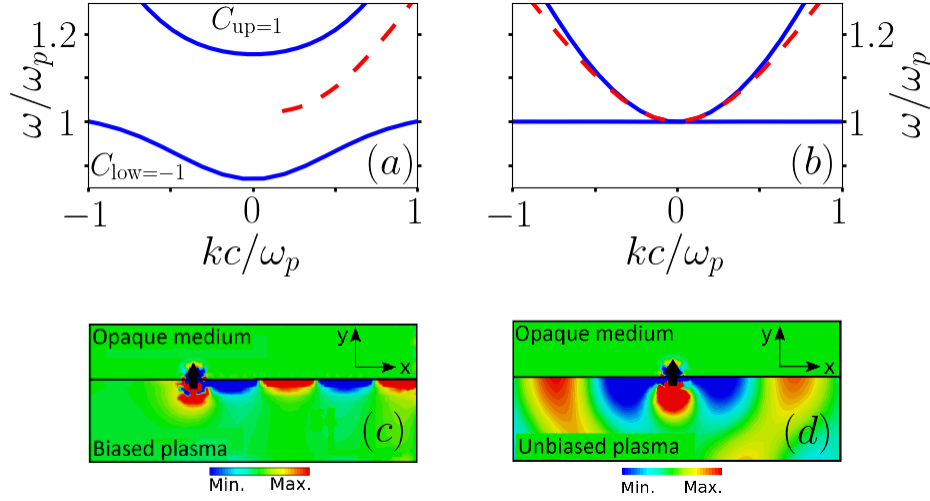


Figure 3.2: Panels (a) and (b): bulk band diagrams of the biased and unbiased plasmas, respectively, along with the dispersions of the SPPs existing at their interfaces with the opaque medium. In the presence of bias [panel (a)], each branch is characterized by a non-trivial Chern number. Panels (c) and (d): Electric profiles generated by a point-source dipole (black arrow) oriented along the y axis at the BP/OM and UP/OM interfaces, respectively. The interface width is $W \rightarrow \infty$, and the plasma frequency is $\omega_p/\omega_0 = 0.95$. In the biased (unbiased) plasma configuration, the cyclotron frequency is $\omega_c/\omega_0 = 0.21$ ($\omega_c/\omega_0 = 0$).

N_e being the free-electron density. When $B_z \neq 0$, the BP bulk supports a TE and a TM mode [80]. The TE mode having a single branch (not shown) of Chern number $C_{\text{TE}} = 0$, it is topologically trivial and will not be considered in the following. The bulk band diagram of the TM mode is represented in Fig. 3.2(a), showing the existence of two branches separated by a band gap. The lower (upper) branch is characterized by a Chern number of $C_{\text{low}} = -1$ ($C_{\text{up}} = 1$) [67, 81]. The gap Chern numbers of the two media are $C_{\text{gap}}^{\text{BP}} = C_{\text{low}} = -1$ and $C_{\text{gap}}^{\text{OM}} = 0$, such that $\Delta C_{\text{gap}} = C_{\text{gap}}^{\text{OM}} - C_{\text{gap}}^{\text{BP}} = 1$, indicating the presence of a single one-way SPP (edge mode) at the BP/OM interface, whose dispersion is also represented in Fig. 3.2(a). Remarkably, this unidirectional SPP is backscattering immune: the propagation channel of opposite direction (reflection) is forbidden and, in addition, being operated in a band gap shared by the two media, radiation into the bulks is prevented. Then, in the presence of imperfections at the interface, the SPP has no other possibility than to remain confined at the interface and to preserve its propagation direction. We note that the SPP propagates along the x axis, along which the atoms are distributed. When $B_z = 0$, on the other hand, the UP is topologically trivial, the bulk TM mode has no band gap, and the UP/OM interface supports a reciprocal SPP [Fig. 3.2(b)].

In Fig. 3.2, the electric profiles generated by a point-source dipole in panels (c) and (d) illustrate the difference between the two configurations with and without biasing field, respec-

tively. It is clear in panel (c) that the SPP propagates unidirectionally and remains confined at the interface, while on the other hand, in panel (d), it propagates in both directions. We note that throughout this chapter, the electric profiles and the electric Green function, which will be needed later, are computed numerically using finite-element method.

3.3 Generalized master equation and basic example

The atoms being located at the interface between the biasable plasma and the opaque medium, their environmental electric field will depend on the SPP propagation properties, which will affect the interactions between atoms, and therefore, the energy-transport properties of the quantum system. To investigate these effects, we turn to the chain dynamics.

By denoting with $|g_i\rangle$ and $|e_i\rangle$, respectively, the ground and excited states of the i -th atom with $i \in \{1, \dots, N\}$, the corresponding lowering operator is $\sigma_i = |g_i\rangle\langle e_i|$. The free Hamiltonian of the chain reads $H_S = \hbar\omega_0 \sum_{i=1}^N \sigma_i^\dagger \sigma_i$, and the total Hamiltonian of the system is

$$H_{\text{tot}} = H_S + H_E + H_{\text{int}}, \quad (3.2)$$

where H_E and H_{int} characterize the free Hamiltonian of the environment and the interaction Hamiltonian, respectively. Being $\mathbf{E}(\mathbf{r})$ the electric field at point \mathbf{r} , the interaction between each atom and its environment under the dipole approximation is expressed as $H_{\text{int}} = -\sum_{i=1}^N (\sigma_i + \sigma_i^\dagger) \boldsymbol{\mu} \cdot \mathbf{E}(\mathbf{r}_i)$. We note that this system is very similar to the one of Ref. [27], where entanglement between a pair of two-level atoms at proximity of a PTI has been investigated with the help of a Markovian quantum master equation. Since our system is identical (similar environment, atomic transition frequency and dipole magnitude), the time scales are the same: the relaxation of the open system is of the order of $\tau_R \sim 10^{-8}$ s in the worst configuration, while its intrinsic evolution time scale is $\tau_S \sim 2.5 \times 10^{-14}$ s and the bath relaxation time scale is $\tau_B \sim 10^{-11}$ s, such that the Born-Markov and rotating-wave approximations can be safely applied here too. Similarly to Ref. [27], in order to describe appropriately the dynamics of the open system by taking into account the potential presence of unidirectional SPP, we have to use the generalized master equation Eq. (1.29), which is valid for both reciprocal and nonreciprocal environments. As a remark, it has been shown [27] that this equation is also suited to describe the dynamics of systems chirally coupled to their environment [82, 83]. In addition, our aim being to investigate the energy-transport properties of the quantum system, we consider energy pumping and extraction on the first and last atoms of the chain, respectively. We also note that thermal effects are negligible here, such that no thermal-photon absorption takes part to the dynamics (differently from the results shown in the other chapters). The pumping process is thus the only way for the chain to gain energy. By denoting $\rho(t)$ the chain reduced density matrix, and introducing the super-operator $\hat{\mathcal{D}}(\sigma_i, \sigma_j)[\rho(t)] = [\sigma_j \rho(t), \sigma_i^\dagger] + [\sigma_i, \rho(t) \sigma_j^\dagger]$, the master equation describing the chain

dynamics reads

$$\begin{aligned} \dot{\rho}(t) = & -\frac{i}{\hbar}[\mathbf{H}_S, \rho(t)] + \left\{ \sum_{i,j=1}^N \frac{\Gamma_{ij}}{2} \tilde{\mathcal{D}}(\sigma_i, \sigma_j) + \sum_{i \neq j} S_{ij} \tilde{\mathcal{D}}(\sigma_i, i\sigma_j) \right. \\ & \left. + \frac{\Gamma_{\text{in}}}{2} \tilde{\mathcal{D}}(\sigma_p^\dagger, \sigma_p^\dagger) + \frac{\Gamma_{\text{out}}}{2} \tilde{\mathcal{D}}(\sigma_e, \sigma_e) \right\} [\rho(t)], \end{aligned} \quad (3.3)$$

where Γ_{in} and Γ_{out} are the pumping and emission rates, respectively. The coefficients associated to the other interactions are [27]

$$S_{ij} = \frac{\omega_0^2}{\varepsilon_0 \hbar c^2} \text{Re}[\boldsymbol{\mu} \cdot \mathbf{G}(\mathbf{r}_i, \mathbf{r}_j, \omega_0) \cdot \boldsymbol{\mu}], \quad \Gamma_{ij} = \frac{2\omega_0^2}{\varepsilon_0 \hbar c^2} \text{Im}[\boldsymbol{\mu} \cdot \mathbf{G}(\mathbf{r}_i, \mathbf{r}_j, \omega_0) \cdot \boldsymbol{\mu}], \quad (3.4)$$

where $\mathbf{G}(\mathbf{r}, \mathbf{r}', \omega)$ is the electric Green function of the system, characterizing the medium response at point \mathbf{r} to a point-source dipole located at \mathbf{r}' . The coefficients Γ_{ij} and S_{ij} correspond to, respectively, $\Gamma_{\text{em}}^{(ij)}(\omega)$ and $S_+^{(ij)}(\omega)$ of Eq. (1.29). As usual, the rate of photon emission Γ_{ij} involves either a single atom ($i = j$) or a pair ($i \neq j$) of atom(s), and characterizes an energy exchange between the quantum system and the environmental field. On the other hand, S_{ij} is associated to a non-dissipative interaction, where energy is transferred from atom j to atom i without modifying the internal energy of the whole quantum system.

It is crucial to point out that these coefficients inherit the reciprocity properties of the environment through the Green function. More specifically, a reciprocal environment is characterized by the relation $\mathbf{G}(\mathbf{r}, \mathbf{r}', \omega) = \mathbf{G}(\mathbf{r}', \mathbf{r}, \omega)$, leading to $\Gamma_{ij} = \Gamma_{ji}$ and $S_{ij} = S_{ji}$. In this case, the master equation Eq. (3.3) reduces to the reciprocal master equation Eq. (1.30) (in the absence of thermal effects). When the environment is nonreciprocal, the Green function is such that $\mathbf{G}(\mathbf{r}, \mathbf{r}', \omega) \neq \mathbf{G}(\mathbf{r}', \mathbf{r}, \omega)$, yielding $\Gamma_{ij} \neq \Gamma_{ji}$ and $S_{ij} \neq S_{ji}$, and the master equation Eq. (3.3) differs from Eq. (1.30). Moreover, in the particular case of a nonreciprocal environment being *unidirectional* in the direction $\mathbf{r} \rightarrow \mathbf{r}'$, then $\mathbf{G}(\mathbf{r}, \mathbf{r}', \omega) = 0$ and $\mathbf{G}(\mathbf{r}', \mathbf{r}, \omega) \neq 0$. It follows that at the BP/OM interface, which supports a unidirectional SPP propagating toward increasing x , the coefficients associated to the chain interactions are such that for atoms $i < j$ with $i, j \in \{1, \dots, N\}$: $\Gamma_{ij} = S_{ij} = 0$, $\Gamma_{ji} \neq 0$ and $S_{ji} \neq 0$. As a remark, we note that although in nonreciprocal systems the generalized master equation has a different structure than standard Markovian quantum master equations (see Chap. 1), numerical simulations have shown that the right-hand side of Eq. (3.3) is trace preserving, and that the resulting density matrix is Hermitian with non-negative diagonal elements summing to 1, consistently with quantum mechanics [82, 84].

Before going further, let us illustrate with a basic example the difference between reciprocal and unidirectional environments regarding the chain dynamics. To this end, in Fig. 3.3, we compare the time evolution of a four-atom chain ($N = 4$) in both configurations: $B_z \neq 0$ and $B_z = 0$. To simplify the system, pumping and extraction processes are switched off by setting

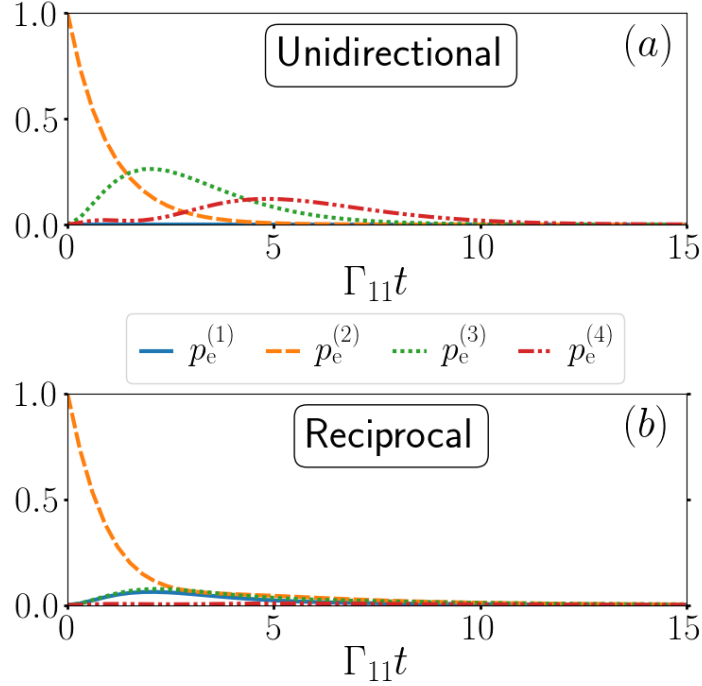


Figure 3.3: Panels (a) and (b): Dynamics of the excited atomic populations of a four-atom chain ($p_e^{(i)}(t)$, with $i \in \{1, 2, 3, 4\}$) in the presence and absence of bias, respectively. No pumping nor extraction is performed here, and the interface width is $W \rightarrow \infty$.

$\Gamma_{\text{in}} = \Gamma_{\text{out}} = 0^1$. The initial state we choose is $|\psi(t=0)\rangle = |g_1 e_2 g_3 g_4\rangle$, where atom 2 is in its excited state while the others are in their ground states. In both configurations, we call $\rho(t)$ the chain density matrix. To track the energy propagation across the different subparts of the atomic system, we consider, for each atom i , the excited population $p_e^{(i)}(t) = \text{Tr}(\sigma_i^\dagger \sigma_i \rho(t))$. The dynamics of these populations are shown in Fig. 3.3 for each configuration. In the presence of biasing field [$B_z \neq 0$, Fig. 3.3(a)], when the SPP is unidirectional, the excitation is clearly traveling throughout the chain. The unidirectionality is highlighted by the fact that atom 1, being located at $x_1 < x_j$ for $j \in \{2, 3, 4\}$, remains unaffected by the presence of the excitation ($\Gamma_{1j} = S_{1j} = 0$). However, as a remark, it must be pointed out that $\Gamma_{j1} \neq 0$ and $S_{j1} \neq 0$: having $p_e^{(1)}(t) \neq 0$, e.g., with different initial conditions, would lead this atom to participate to the processes of dissipation and interatomic energy transfer. In the UP configuration [$B_z = 0$, Fig. 3.3(b)], the SPP is reciprocal, such that $\Gamma_{ij} = \Gamma_{ji}$ and $S_{ij} = S_{ji}$. In particular, atom 2 can transfer energy to its neighbors on both sides, including atom 1, as can be seen. On the other hand, atom 4 is almost unaffected by the excitation, as most of the energy is dissipated before reaching it. This example clearly illustrates that SPP-assisted energy transport is more advantageous in the unidirectional case, as the energy flow

¹Pumping and extraction being not present in this example, we temporarily drop the notation $\{p, 2, 3, e\}$ and rather use $\{1, 2, 3, 4\}$ to name the atoms.

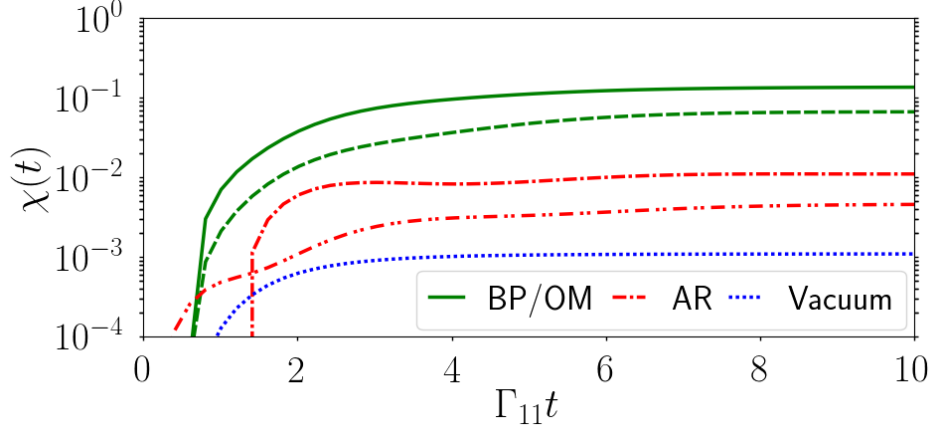


Figure 3.4: Dynamics of the energy-transport efficiency for different environments and interface widths (see the main text). The chain step is $a/\lambda_0 = 0.9$.

is oriented along the chain direction. In the following, we quantify the difference between the two environmental configurations in terms of energy-transport efficiency.

3.4 Transport-efficiency enhancement induced by unidirectional-SPP

In this section, considering a four-atom chain, we show that energy transport assisted by one-way SPP is drastically more efficient than with a reciprocal SPP. Remarkably, as we will see, the enhancement factor between these two configurations is of one order of magnitude.

The definition of energy-transport efficiency we will use throughout this Chapter is the one defined in Chap. 2 through Eq. (2.14), which we recall:

$$\chi(t) = \frac{E(t) - E_0(t)}{P(t)}, \quad (3.5)$$

where $E_0(t)$ [$E(t)$] corresponds to the flux of energy extracted from the last atom of the chain, atom e , in the absence (presence) of pumping, whereas $P(t)$ is the energy flux pumped into the first atom, atom p . In the present chapter, these fluxes are expressed as

$$\begin{aligned} E_0(t) &= -\frac{\Gamma_{\text{out}}}{2} \text{Tr} \left(H_S \tilde{\mathcal{D}}(\sigma_e, \sigma_e) [\rho_0(t)] \right), \\ E(t) &= -\frac{\Gamma_{\text{out}}}{2} \text{Tr} \left(H_S \tilde{\mathcal{D}}(\sigma_e, \sigma_e) [\rho(t)] \right), \\ P(t) &= \frac{\Gamma_{\text{in}}}{2} \text{Tr} \left(H_S \tilde{\mathcal{D}}(\sigma_p^\dagger, \sigma_p^\dagger) [\rho(t)] \right), \end{aligned}$$

where $\rho_0(t)$ and $\rho(t)$ are the chain density matrices in the absence and presence of pumping,

respectively. We recall that in contrast with Chap. 2, there is no thermal effects here: energy is absorbed by the chain only through the pumping process, such that the efficiency is up bounded by $\chi_{\max}(t) = 1$, for any t . During the time evolution, the lower bound to $\chi(t)$ depends on the chain initial state. However, since in the absence of pumping the chain energy can only decrease, this leads to $E_0(\infty) = \lim_{t \rightarrow \infty} E_0(t) = 0$. Thus, the stationary efficiency $\chi(\infty) = \lim_{t \rightarrow \infty} \chi(t)$ is such that $0 \leq \chi(\infty) \leq 1$. We note that in the following, unless specified otherwise, the pumping and extraction rates will be arbitrarily fixed at $\Gamma_{\text{in}} = \Gamma_{\text{out}} = 1.5\Gamma_{11}$.

Before starting the comparison between reciprocal and unidirectional chain environments, it is important to raise the following point. Setting the biasing-field magnitude to $B_z = 0$ or $B_z \neq 0$ leads to the generation of SPPs that differ not only with regards to their propagation properties, but also with respect to other features (intensity, confinement factor, etc.). If, on the one hand, the comparison between these two configurations is relevant, as they both characterize systems with realistic parameters, on the other hand, focusing on the effect of one-wayness on energy transport requires a fair comparison, i.e., between SPPs of equivalent properties (other than propagation direction). To this end, based on a unidirectional SPP calculated with realistic parameters, for which $S_{ij} = 0$ and $\Gamma_{ij} = 0$ for atoms $i < j$, we introduce an artificially-reciprocal (AR) SPP by setting $S_{ij} = S_{ji}$ and $\Gamma_{ij} = \Gamma_{ji}$, and by multiplying Γ_{ii} by a factor 2 [83]. In this way, the transport efficiencies assisted by the unidirectional and AR SPPs can be fairly compared to highlight the effects of one-wayness.

Figure 3.4 shows the transport-efficiency dynamics of a four-atom chain ($N = 4$) for a BP/OM interface of width W (green curves) and its corresponding AR environment (red curves) (vacuum is also shown through the blue line). The comparison between the two environments is realized for two different interface widths: $W/\lambda_0 = 1.2$ (solid green and dot-dashed red lines) and $W \rightarrow \infty$ (dashed green and double-dotted-dashed lines). In all these cases, the initial state is $|\psi(t=0)\rangle = |g_1 g_2 g_3 e_4\rangle$, and the efficiency dynamics is roughly identical: at the beginning of the time evolution, as long as the difference between the pumping and no-pumping scenarios has not appeared, the efficiency is $\chi(t) = 0$. As soon as this difference manifests itself, then $\chi(t) \neq 0$, and eventually the system reaches stationarity. Let us focus on the comparison of the stationary efficiency between unidirectional- and reciprocal-SPP-assisted energy transport, starting with the finite-width-interface configuration ($W/\lambda_0 = 1.2$). It appears clear that the unidirectional environment is much more advantageous, producing a transport efficiency amplified by more than one order of magnitude with respect to the reciprocal case. To be more specific, the fraction of pumped energy transported to the end of the chain in the AR environment is negligible, being of $\chi(\infty) \sim 0.01$, while on the other hand, the BP/OM interface leads to a significant transport efficiency: $\chi(\infty) \sim 0.14$. In the configuration with $W \rightarrow \infty$, the difference between the two configurations is of the same order, although the efficiencies are smaller than their respective finite-width-interface counterpart. In any case, all of these configurations realize a more efficient energy transport than vacuum (free-space).

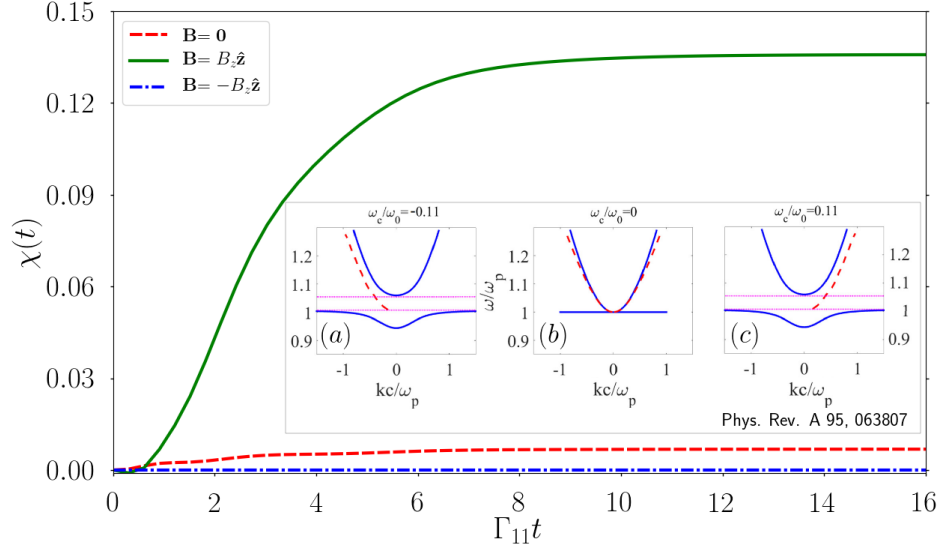


Figure 3.5: Panels (a-c): Examples of bulk band diagrams and SPP dispersions for different bias. Main figure: Dynamics of the energy-transport efficiency of a four-atom chain for different bias. The chain step is $a/\lambda_0 = 0.9$ and the interface width is $W/\lambda_0 = 1.2$.

Thus, the one-wayness character of the SPP assisting energy transport along the chain leads to a drastic amplification of the energy-transport efficiency with respect to an equivalent reciprocal atomic environment. Although the values of efficiency presented in these results might seem relatively low, we stress that efficiency optimization is not our purpose here. A maximization of $\chi(\infty)$ with respect to relevant parameters (chain step, atomic frequency, etc.) could lead to considerably-larger efficiencies.

3.5 Practical advantages

In this section, we will mainly focus on realistic configurations, i.e., where reciprocal and unidirectional SPPs are both calculated from realistic parameters. This will allow us to point out several properties which are interesting with regards to practical realizations of PTI-based energy transport.

We start our investigation by the control of energy transport through the tuning of the biasing magnetic field. As discussed previously, setting either $B_z = 0$ or $B_z \neq 0$ changes the propagation properties of the SPP at the interface between the biasable plasma and the OM, due to topological properties. In particular, when $B_z \neq 0$, it must be pointed out that the direction of the biasing field determines the propagation direction of the unidirectional SPP. As an example, Fig. 3.5 shows the bulk band diagram of the biasable plasma along with the SPP dispersion for different bias: $\mathbf{B} = -B_z \hat{z}$, $\mathbf{B} = \mathbf{0}$ and $\mathbf{B} = B_z \hat{z}$, in panels (a), (b) and (c), respectively. We note that these diagrams stem from Ref. [27], where an

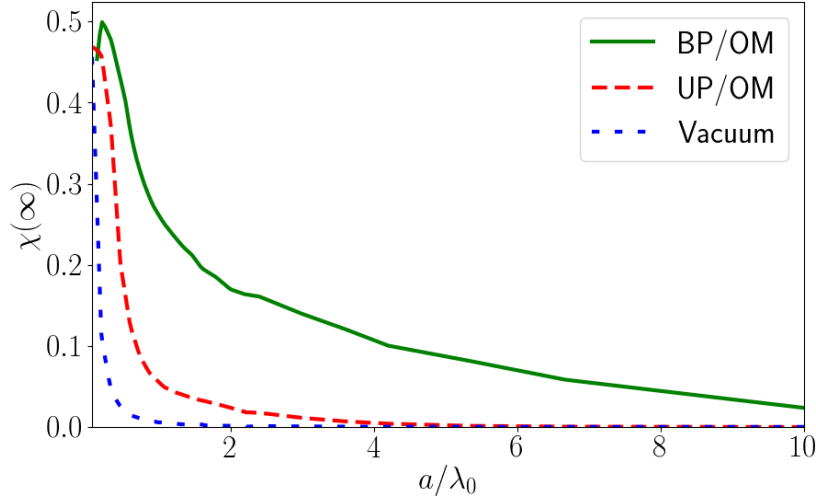


Figure 3.6: Stationary energy-transport efficiency of a two-atom chain as a function of the chain step (i.e. the distance between the two atoms) in different environments. The interface width is $W/\lambda_0 = 1.2$.

interface similar to ours is involved. In our case, having $\pm B_z$ settles whether the unidirectional SPP is propagating toward increasing (B_z) or decreasing ($-B_z$) x . The transport efficiency corresponding to these different biasing fields is shown in the main part of Fig. 3.5 in the case of a four-atom chain ($N = 4$). Let us concentrate on the stationary efficiency. In the absence of biasing field ($B_z = 0$, dashed red line), the fraction of pumped energy reaching the extraction atom is negligible ($\chi(\infty) \sim 0.007$). On the other hand, with $\mathbf{B} = B_z \hat{\mathbf{z}}$ (solid green line), the unidirectional SPP propagating in the chain direction $p \rightarrow e$ amplifies significantly the transport efficiency: $\chi(\infty) \sim 0.14$. More remarkably, when $\mathbf{B} = -B_z \hat{\mathbf{z}}$ (dot-dashed blue line), the efficiency remains strictly null: $\chi(t) = 0$, for any t . This comes from the fact that the energy pumped into atom p cannot be transmitted to the other atoms of the chain ($\Gamma_{j1} = S_{j1} = 0$, where the index 1 stands for atom p , and with $j \in \{2, 3, 4\}$), and has no other possibility than to be dissipated into the environment ($\Gamma_{11} \neq 0$). Then, whether pumping is performed or not, the energy extracted from atom e is the same [$E(t) = E_0(t)$], leading to $\chi(t) = 0$, for any t . It follows from this analysis that energy transport can be tuned, to a certain extent, by simply modifying the biasing field: in the absence of bias, starting from a low-efficiency transport at the reciprocal UP/OM interface, one can choose either to enhance it by one order of magnitude or to completely switch it off.

Another advantage of the BP/OM interface comes from the enhancement of the interatomic-interaction range. Figure 3.6 shows the stationary efficiency $\chi(\infty)$ of a two-atom chain ($N = 2$) as a function of a/λ_0 , characterizing the distance between the two atoms (chain step). The transport efficiency has been computed for three different atomic environments: UP/OM (dashed red line) and BP/OM (solid green line) interfaces, and vacuum (dotted blue

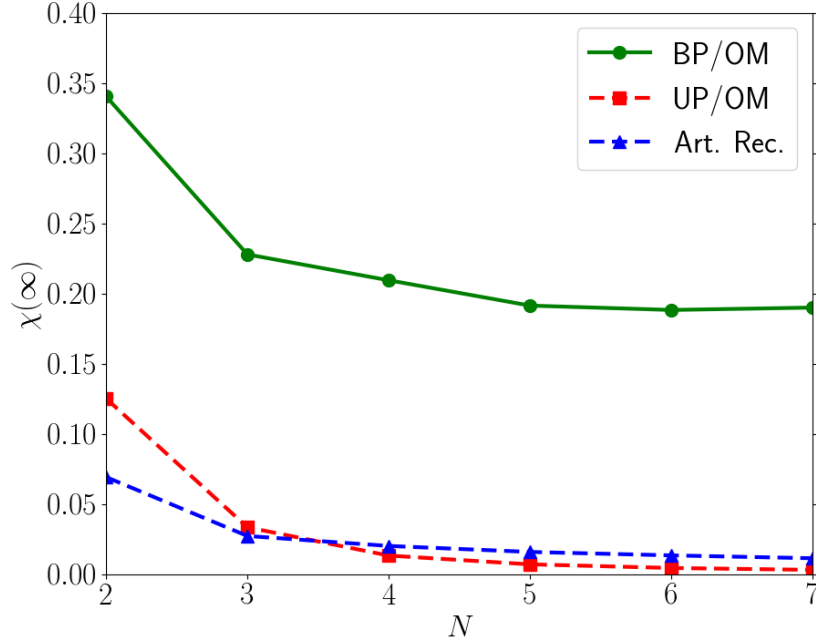


Figure 3.7: Stationary energy-transport efficiency as a function of the number of atoms composing the chain for different environments. The chain step is fixed at $a/\lambda_0 = 0.6$ and the interface width is $W/\lambda_0 = 1.2$.

line). The unidirectional SPP proves to be the best (in terms of energy transport) for two reasons. Firstly, for any chain step, it produces the greater transport efficiency. Secondly, $\chi(\infty)$ remains significant for atomic separations which are considerably larger than in the two other configurations. For example, realizing energy transport with $\chi(\infty) = 0.1$ with the UP/OM interface requires $a/\lambda_0 \simeq 0.7$, whereas in the case of a BP/OM interface, the same value of efficiency is achieved with a chain step approximately 6 times larger.

A different strategy to enhance the transport range, which necessitates to increase the chain length, is to increase the number of atoms, rather than increasing the distance between them. The behavior of the stationary efficiency as a function of N is shown in Fig. 3.7, where for each N -atom chain, the step is fixed at $a/\lambda_0 = 0.6$. The atomic environments in this plot are BP/OM (green line) and UP/OM (red line) interfaces, as well as the AR environment (blue line) obtained from the BP/OM interface, similarly to Fig. 3.4. Once again, the unidirectional SPP leads to a transport efficiency significantly greater than the two reciprocal configurations, for each N . Moreover, with the atom number increasing, $\chi(\infty)$ decreases slowly in the nonreciprocal case, producing considerable values of transport efficiency up to at least $N = 7$, $\chi(\infty) \simeq 0.2$, which is larger than any N -atom chain ($N \leq 7$) in the reciprocal configurations. On the contrary, with the UP/OM interface and the AR environment, the efficiency decreases to negligible values very quickly.

Last but not least, we now turn to the energy-transport properties with regards to one

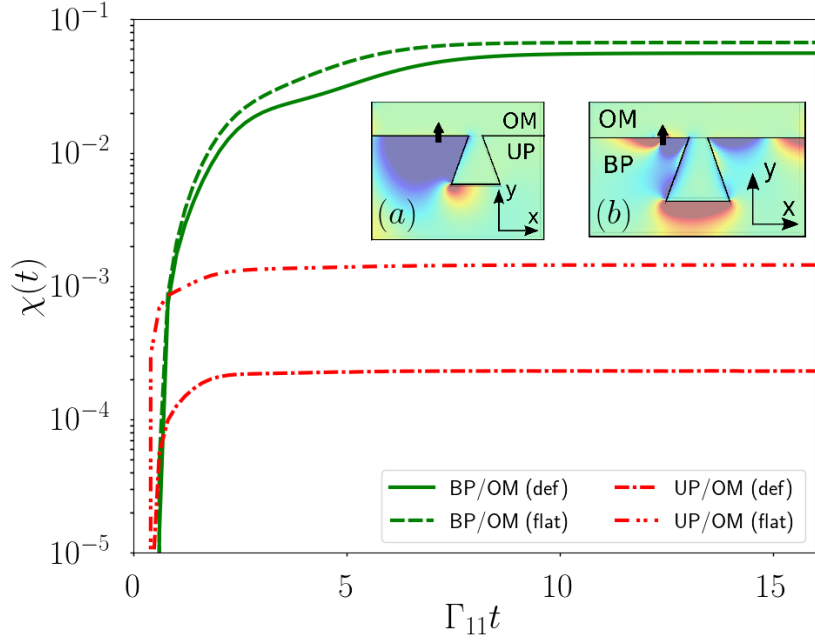


Figure 3.8: Panels (a) and (b): Electric profiles generated by a point-source dipole (black arrow) at the defected (deformed) BP/OM and UP/OM interfaces, respectively. Main part: Dynamics of the energy-transport efficiency of a four-atom chain for flat and defected BP/OM and UP/OM interfaces (see the main text). The chain step is $a/\lambda_0 = 0.9$ and the interface width is $W \rightarrow \infty$.

of the most celebrated features stemming from the PTIs: robustness of the SPP propagation against backscattering. Indeed, as shown in Fig. 3.2(a), the SPP propagating at the BP/OM interface cannot reach the bulks of the two media, and therefore remains confined at the interface. In addition, the SPP is unidirectional, and as such, in the presence of a defect (deformation/imperfection) at the interface, reflection cannot occur since the propagation channel of opposed direction is closed. Then, from the combination of these two properties, it follows that the SPP has no other possibility than to bypass the obstacle. This is illustrated with the electric profiles of the UP/OM and BP/OM interfaces, shown in Figs. 3.8(a) and (b), respectively, where the defect consists in a trapezoidal-shaped interface deformation of contour length $\simeq 1.8\lambda_0$. We note that there is no bulk band gap in the UP band structure [Fig. 3.2(b)]. The dynamics of transport efficiency corresponding to these configurations is shown in Fig. 3.8, for an interface of infinite width. The chain is composed of $N = 4$ atoms, and the defect is located in between the positions of atoms 2 and 3, i.e. in the middle of the chain. As expected from the electric profiles, the BP/OM interface (green lines) generates a robust energy-transport efficiency. More precisely, the defected interface (solid green line) produces a stationary efficiency $\chi(\infty) \simeq 0.056$, which is barely lower than the flat interface (dashed green line), for which $\chi(\infty) \simeq 0.067$. On the contrary, at the UP/OM interface, the

stationary transport efficiency is strongly sensitive to the presence of defect, diminishing of almost one order of magnitude. Moreover, in the defected-interface configuration, which is more likely to occur in practical realizations (e.g., due to fabrication errors), the efficiency amplification from UP to BP is of more than 2 orders of magnitude.

3.6 Physical insight with two-atom chains

In this section, we will consider a chain composed of $N = 2$ atoms. Instead of considering a specific environment, as we did previously with the biasable plasma of permittivity ϵ [Eq. (3.1)], we will rather manipulate the coefficients of the master equation describing the chain dynamics, regardless of the physical system likely to generate them. To be more specific, we will determine the coefficients which produce the best efficiency in reciprocal and unidirectional environments, respectively. This will help us to understand why the latter are more favorable for energy transport.

To begin with, we make the assumption that the main contribution to the Green's function comes from the SPP [27, 85], and based on Eqs. (3.4), we parametrize the master-equation coefficients as

$$\begin{aligned} S_{ij} &= 0.5X \cos(\phi), \\ \Gamma_{ij} &= X \sin(\phi), \end{aligned}$$

where both parameters $X > 0$ and $\phi \in [0, 2\pi]$ depend on the atomic separation such that $\lim_{a \rightarrow 0} \Gamma_{ij} = \Gamma_{ii}$. Moreover, we assume that $\Gamma_{11} = \Gamma_{22}$, which amounts to presume that the two atoms have exactly the same environment, such that the parametrization only affects their SPP-mediated interaction. To model a reciprocal environment, the coefficients must verify $S_{12} = S_{21}$ and $\Gamma_{12} = \Gamma_{21}$, whereas for a unidirectional one, $S_{12} = \Gamma_{12} = 0$. As mentioned above, our goal here is to determine the values of these parameters which result in the maximum transport efficiency, for each environment.

Our first step toward this maximization will be to determine the value of the parameter ϕ . To this end, Fig. 3.9 shows the stationary efficiency as a function of this parameter, when X is fixed. The solid (dashed) lines correspond to the reciprocal (unidirectional) configuration, for different values of X . As can be seen, the reciprocal environment always produces a maximized efficiency when $\phi = \pi/2 \bmod \pi$, whereas in the unidirectional case, $\chi(\infty)$ is insensitive to variations of ϕ . Then, in the following, we will settle $\phi = \pi/2$. The corresponding master-equation coefficients are $S_{12} = S_{21} = 0$ for both environments, and $\Gamma_{12} = \Gamma_{21} = X$ ($\Gamma_{12} = 0$ and $\Gamma_{21} = X$) for the reciprocal (unidirectional) case. This constitutes the *dissipative regime*, where the atoms only exchange energy with their environment, and not between each other. Moreover, it is worth pointing out that, for both environments, the efficiency increases along with X . To maximize the efficiency, we then have to determine the maximum value attainable

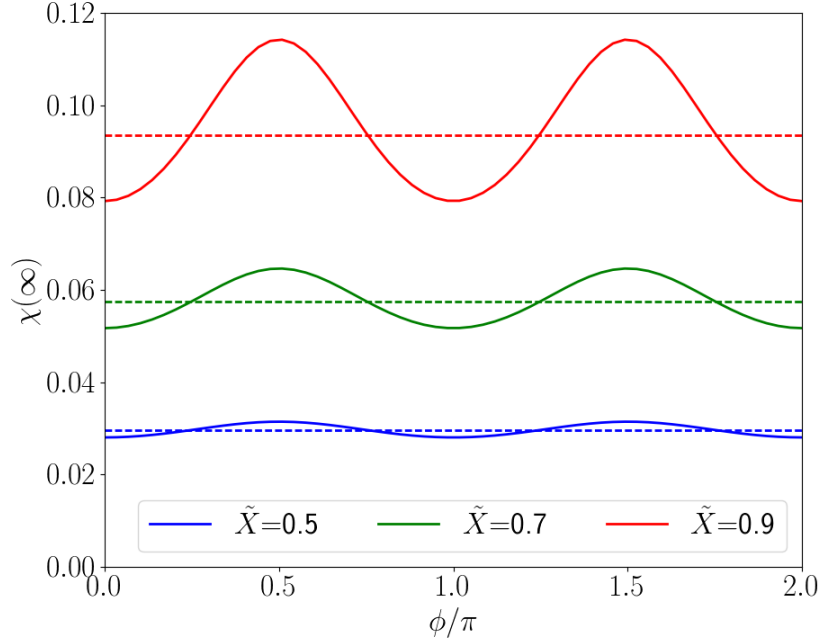


Figure 3.9: Stationary energy-transport efficiency of a two-atom chain as a function of the parameter ϕ for different values of $\tilde{X} = X/\Gamma_{11}$. The solid lines correspond to a reciprocal environment, and the dashed lines to a unidirectional one.

for X , which, within the dissipative regime, amounts to find the upper bound to Γ_{21} .

To have a valid reciprocal master equation, the dissipative rates involved in the diagonal form of the master equation (see Chap. 1) must be non-negative [24]. For a system composed of a pair of two-level atoms, these coefficients are $\Gamma_{\pm} = \Gamma_{11} \pm \sqrt{\Gamma_{12}\Gamma_{21}} \geq 0$ ($\Gamma_{11} = \Gamma_{22}$ being assumed), which leads to the relation $\Gamma_{21} \leq \Gamma_{11}$, since $\Gamma_{12} = \Gamma_{21}$ holds for reciprocal systems. Thus, Γ_{11} is an upper bound to Γ_{21} , as confirmed by Fig. 3.10. This plot shows Γ_{21} as a function of the distance between the two atoms, for several environments. For now, we are only interested in the reciprocal ones: UP/OM interface, vacuum, vacuum–dielectric material of permittivity $\varepsilon = +2$ and vacuum–dielectric material of permittivity $\varepsilon = -2$. The two last ones have been chosen as representatives of typical reciprocal environments. As can be seen, in all of these cases, the condition $\Gamma_{21} \leq \Gamma_{11}$ is verified. Thus, we now have the values of the parameters maximizing the efficiency in the reciprocal case: $(X, \phi) = (\Gamma_{11}, \pi/2)$. On the other hand, for nonreciprocal environments, the master-equation structure is different from the reciprocal one, and the property $\Gamma_{21} \leq \Gamma_{11}$ is not necessarily required. This is confirmed by the example of the BP/OM interface shown in Fig. 3.10, where Γ_{21} reaches values up to 7 times larger than Γ_{11} , which is considerable. This difference of allowed values for Γ_{21} marks a strong distinction between reciprocal and unidirectional systems, since the atomic coupling can be significantly stronger in the latter case. Moreover, it is worth stressing that the maximum coupling in the reciprocal case, $\Gamma_{21} = \Gamma_{11}$, is only obtained in the unrealistic

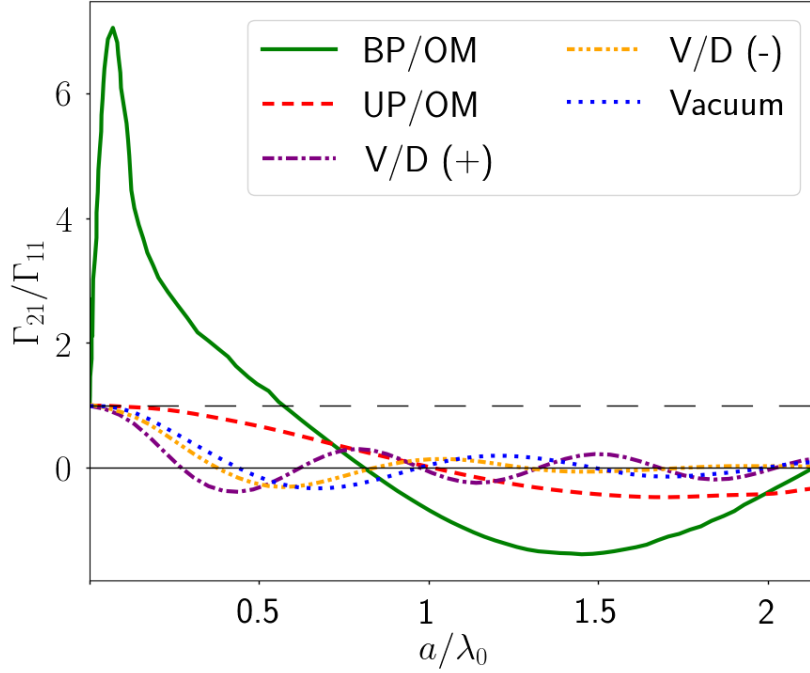


Figure 3.10: Master-equation coefficient Γ_{21} as a function of the distance between the two atoms, resulting from numerical simulations of different environments (see main text).

limit $a \rightarrow 0$, whereas there is a large number of atomic separations in the unidirectional configuration that produce $\Gamma_{21} > \Gamma_{11}$.

Figure 3.11 shows the stationary efficiency in the reciprocal case when Γ_{21}/Γ_{11} is increased, in the purely-dissipative regime ($\phi = \pi/2$, $S_{12} = S_{21} = 0$, $\Gamma_{12} = \Gamma_{21} = X$). As already hinted by Fig. 3.9, $\chi(\infty)$ increases along with Γ_{21}/Γ_{11} , until the limiting case $\Gamma_{21}/\Gamma_{11} = 1$ is reached, where the maximum transport efficiency achievable in this configuration is produced: $\chi(\infty) \simeq 0.12$. In addition to this reciprocal environment, we consider an artificially-unidirectional system, in the same spirit as for Fig. 3.4, this time by setting $\Gamma_{12} = 0$ and dividing the local rates $\Gamma_{11} = \Gamma_{22}$ by 2. In this way, a fair comparison between reciprocal and unidirectional environments can be done within $\Gamma_{21}/\Gamma_{11} \in [0, 1]$. In this interval, the unidirectional configuration produces a better energy-transport efficiency than the reciprocal one, and additionally, the gap between their efficiencies increases with Γ_{21} . At the reciprocal limiting case ($\Gamma_{21}/\Gamma_{11} = 1$), the unidirectional efficiency ($\chi(\infty) \simeq 0.39$) is more than 3 times greater than the reciprocal one. More remarkably, when $\Gamma_{21}/\Gamma_{11} > 1$, which corresponds to a region strictly forbidden to reciprocal systems, the efficiency keeps increasing and takes on significant values, reaching $\chi(\infty) = 0.83$ in the best configuration.

In summary, by comparing equivalent reciprocal and unidirectional environments in the dissipative regime, which is the more favorable for energy transport, we have demonstrated that unidirectional systems are considerably much more favorable than reciprocal ones with

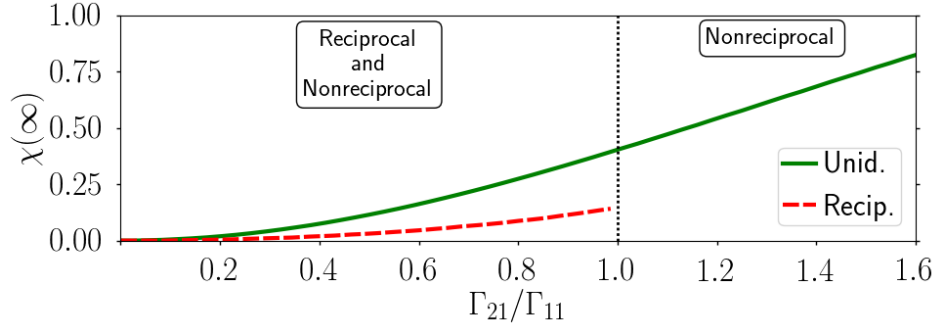


Figure 3.11: Stationary energy-transport efficiency of a two-atom chain as a function of Γ_{21} within the dissipative regime ($\phi = \pi/2$) in reciprocal and unidirectional environments. The latter is obtained artificially from the reciprocal case (see main text). The reciprocal configuration is restricted to $\Gamma_{21} \leq \Gamma_{11}$, unlike the unidirectional one.

respect to energy transport. This is the case not only in terms of transport efficiency, but also with regards to practical aspects. Indeed, the maximum reciprocal efficiency is reached in the limiting case of infinitely close atoms, while unidirectional systems produce a larger efficiency for number of realistic atomic separations. Then, unidirectional systems offer the possibility to transport energy more efficiently and over larger distances than comparable reciprocal environments, which is possible due to the stronger atomic coupling that they are able to produce.

3.7 Conclusion

In this chapter, we have investigated the energy-transport efficiency of an atomic chain composed of N two-level atoms, located at the interface between a PTI and an opaque medium. Due to the PTI properties, this interface supports a unidirectional SPP which is backscattering immune. By comparing SPP-assisted energy transport along the chain between reciprocal and unidirectional SPPs, we have shown that the effect of one-wayness is to amplify the transport efficiency by one order of magnitude.

In addition, we have highlighted several energy-transport features stemming from PTI properties, making them particularly advantageous in the perspective of practical realizations of environment-assisted energy transport along an atomic chain. More specifically, we have shown that the transport efficiency can be tuned through the magnitude and the orientation of the magnetic field biasing the plasma: starting from the reciprocal configuration (unbiased plasma), the transport efficiency can be either strictly switched off, or enhanced by one order of magnitude.

Besides, we have discussed the enhancement of the transport range induced by the unidirectional SPP: for a two-atom chain, the unidirectional transport efficiency remains signif-

icant for considerably larger distances than its reciprocal counterpart. Moreover, we have considered chains with different atom numbers. With reciprocal environments, increasing this number quickly leads to a transport efficiency which is negligible, whereas it remains significant up to at least seven-atom chains in the unidirectional case.

We have also shown that the backscattering-immune property of the unidirectional SPP is of major interest regarding energy transport. Indeed, despite the presence of considerable defect on its path, the unidirectional SPP remains confined at the interface and bypasses the obstacle, while on the other hand, in the reciprocal case, the SPP propagation is strongly affected by the defect. This leads to a transport efficiency in the unidirectional case that is amplified by two orders of magnitude with respect to the reciprocal one.

Finally, in order to determine the best efficiency achievable in reciprocal and unidirectional configurations, we have parametrized the coefficients of the master equation associated to a two-atom chain. With the help of this parametrization, we have shown that in both environments, the efficiency is always better in the dissipative regime. In this regime, we have determined an upper bound to the non-local transition rate Γ_{21} , which only applies to reciprocal environments. Below this threshold, the transport efficiency is always larger in the unidirectional environment. In addition, the upper bound to Γ_{21} does not hold for the unidirectional SPP, and this parameter can take larger values, corresponding to a stronger dissipative coupling between the two atoms, which leads to an even better transport efficiency. Moreover, such a coupling, unattainable in reciprocal environments, is achievable for a large number of geometrical configurations, thereby highlighting a supplementary advantage of using unidirectional SPPs to assist energy transport rather than reciprocal ones.

Quantum thermal machine out of thermal equilibrium

Contents

4.1	Introduction	61
4.2	Physical system	63
4.3	Open quantum system and out-of-thermal-equilibrium environment .	64
4.3.1	General model and master equation	64
4.3.2	Auto-correlation functions of the OTE EM field	66
4.4	Three-level atom as quantum thermal machine	71
4.4.1	Environmental and population temperatures	71
4.4.2	Three-level atom in an OTE field as thermal machine	74
4.5	Role of correlations in thermodynamic tasks	75
4.6	Robustness of thermal tasks	84
4.7	Tuning thermodynamical tasks	86
4.8	Variation of the number of qubits	89
4.9	Conclusion	92

4.1 Introduction

Quantum thermodynamics is a field of research that has been under investigation since the 1950's [86], for which interest has only been growing over the last decades [22, 23, 86–121]. For example, the formulation of thermodynamics laws in the quantum regime has been investigated [114, 122], as well as the foundations of statistical thermodynamics based on quantum effects. One can also mention the study of fluctuations theorems of nonequilibrium quantum systems [116, 117, 123–126], quantum phase transitions in condensed matter physics [127, 128], or also work extraction from quantum systems [129–131].

A number of these investigations have been performed based on physical systems capable of performing thermal tasks in the quantum regime [22, 23, 86–110, 112, 114, 118–120], offering the opportunity to investigate multiple aspects of quantum thermodynamics, such as

entropy production and irreversibility [92, 116, 117, 121], or also entangled quantum thermal machines [91]. In addition, inspired by classical thermal machines reduced down to the microscopic scale, e.g. with single ion [132] or single colloidal particle [133] in Paul traps, multiple experimental schemes have been proposed for the realization of quantum thermal machines [108–110, 134]. This could be of interest not only to confront theoretical predictions with experiments, but also to pave the way for future applications, ranging from nano-technologies [135] to molecular biology [12].

Among the different models of quantum thermal machines, the so-called ‘self-contained’ quantum machines have drawn a considerable attention [22, 23, 86, 100–110], being able to perform thermal tasks without external driving. Specifically, a *quantum absorption refrigerator* is a quantum system able to establish a stationary heat flux from a macroscopic colder bath to a hotter one, by absorbing energy from a third bath. However, practical realizations of such quantum thermal machines are usually not easy. The main reason for this is that different transitions of the same quantum system are required to be coupled with each other while simultaneously being in thermal contact with independent macroscopic thermal baths.

To overcome this difficulty, it has been shown that a single out-of-thermal-equilibrium (OTE) environment is a promising framework for realistic implementations of quantum absorption thermal machines [18]. In this case, the role of the machine is played by a three-level quantum emitter (‘atom’) interacting with a single OTE electromagnetic (EM) field. Due to the OTE character of the environment, different transitions of the machine can be seen as interacting with different effective macroscopic thermal baths. It has been shown that this physical set up provides the machine with the ability to perform a task on a target body consisting in a single two-level atom (‘qubit’), in this sense that the qubit energy can be either increased (\equiv heating) or decreased (\equiv cooling) by the machine. This first result is encouraging in the perspective of manipulating energy within quantum systems composed of a very few atoms.

In this chapter, we push a step further this investigation by considering a target body being a multipartite quantum system. To be more precise, we will investigate OTE configurations involving $N = 2, \dots, 6$ qubits in addition to the machine. We will notably demonstrate that the machine is able to deliver thermal tasks of strong intensities on systems of increasing size (in terms of Hilbert-space dimension). Moreover, we will discuss several possibilities for tuning these thermal tasks, not only on the whole qubits system, but also on each qubit individually. The role of correlations will be discussed, and the robustness of the task delivery will be confronted to variations of several parameters. The results presented in this chapter have been published in Refs. [22, 23].

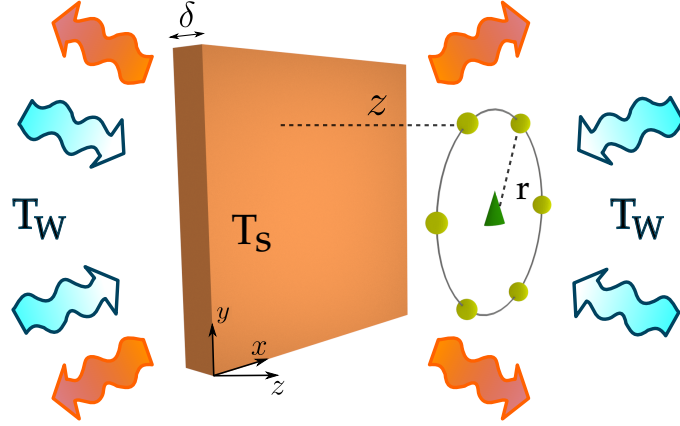


Figure 4.1: Physical system: quantum emitters embedded in an out-of-thermal-equilibrium electromagnetic field, which is produced by a blackbody radiation at T_W and a dielectric slab at $T_S \neq T_W$. The quantum system is located at a distance z from the slab, which is made of sapphire, and has thickness $\delta = 50$ nm.

4.2 Physical system

In this Chapter, we analyze the energy exchanges occurring within a specific quantum system which is embedded in an out-of-thermal-equilibrium electromagnetic field. More precisely, this quantum system is composed of $N + 1$ quantum emitters (referred to as ‘atoms’): N identical qubits (i.e. two-level atoms), with $N = 1, \dots, 6$, and a single three-level atom (the ‘machine’). Previous studies have characterized the energy distribution of a single n -level atom ($n \geq 2$) interacting with an OTE EM field [28]. Furthermore, considering two interacting atoms in such a field, it has been shown that a three-level atom can significantly modify the energy distribution of a qubit ($N = 1$) [18]. This analysis has been performed with a quantum thermodynamical approach, where the three-level atom can be identified as a quantum thermal machine delivering a task on a target body, the qubit.

As shown in Fig. 4.1, the quantum system is located in proximity of a dielectric slab at temperature T_S . In our case, the slab will have a thickness of $\delta = 50$ nm, and will be made of sapphire, which has a resonance frequency of $\omega_S = 0.81 \times 10^{14} \text{ rad} \cdot \text{s}^{-1}$. The quantum system and the slab are both irradiated by a blackbody radiation emitted by distant walls at temperature T_W . When the two temperatures involved are equal, the EM field surrounding the atoms is at thermal equilibrium at $T_{\text{eq}} = T_S = T_W$. However, this will generally not be the case in our investigations: the temperatures will differ ($T_S \neq T_W$), thereby producing an OTE EM field. In any case, it must be stressed that the two temperatures are fixed in time, such that the EM field is stationary. The geometry of the quantum system can be understood with the help of Figs. 4.1 and 4.2. All the atoms belong to the xy -plane, which is parallel to the slab surface. The distance between this plane and the slab is characterized by the coordinate z . The qubits, labeled $\{1, \dots, N\}$, form a regular polygon of radius r centered on

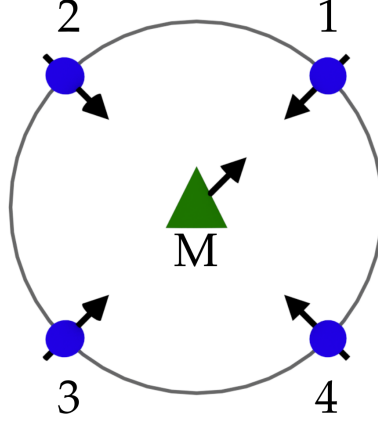


Figure 4.2: Geometrical configuration of the quantum system when $N = 4$. The green triangle (blue discs) represents the three-level atom, labeled M (qubits, labeled $\{1, 2, 3, 4\}$). The black arrows indicate the induced dipole directions of the emitters.

the machine. As will be detailed in the following, an essential parameter in all the system energy exchanges is the dipole moment associated to each atomic transition, through both its orientation and magnitude. While the dipole orientations will be variable parameters in this chapter, the magnitudes, on the other hand, will all be fixed at the value $10^{-30} \text{ C} \cdot \text{m}$.

4.3 Open quantum system and out-of-thermal-equilibrium environment

4.3.1 General model and master equation

The Hamiltonian characterizing the time evolution of the total system (quantum system and electromagnetic field) has the form

$$H_{\text{tot}} = H_S + H_E + H_{\text{int}}, \quad (4.1)$$

where H_S is the free Hamiltonian of the atomic system, H_E the one of the electromagnetic field, and H_{int} is the Hamiltonian describing the atoms-field interactions. Let us start focusing on the atomic system. The free Hamiltonian eigenstates of the three-level atom (the machine) are labeled $|0\rangle$, $|1\rangle$ and $|2\rangle$. To these states are associated three atomic transitions, indexed by $\tau \in \{1, 2, 3\}$, where $\tau = 1$ corresponds to the transition between states $|0\rangle$ and $|1\rangle$, $\tau = 2$ between $|1\rangle$ and $|2\rangle$, and $\tau = 3$ between $|0\rangle$ and $|2\rangle$. Using the index M to denote the machine, the corresponding lowering operators are $\sigma_1^{(M)} = |0\rangle\langle 1|$, $\sigma_2^{(M)} = |1\rangle\langle 2|$, and $\sigma_3^{(M)} = |0\rangle\langle 2|$. The transition frequencies are designated by ω_τ , and the hierarchy of the energy levels is such that $\omega_3 = \omega_1 + \omega_2$. Moreover, ω_3 is chosen to be in resonance with the slab resonance frequency,

$\omega_3 = \omega_S$, thereby being resonant with the EM-field mode the most affected by the presence of the slab. The ground and excited states of the i -th qubit are $|g_i\rangle$ and $|e_i\rangle$, respectively, and the corresponding lowering operator is $\sigma_q^{(i)} = |g_i\rangle\langle e_i|$, with $i \in \{1, \dots, N\}$. All qubits share the same transition frequency ω_q , which is also identical to the machine transition $\tau = 2$: $\omega_q = \omega_2$. Then, using the indexes $\tau = \{1, 2, 3, q\}$ and $a \in \{M, 1, \dots, N\}$, the free Hamiltonian of the quantum system reads

$$\begin{aligned} H_S &= \sum_{\tau} \sum_a \hbar \omega_{\tau} \sigma_{\tau}^{(a)\dagger} \sigma_{\tau}^{(a)}, \\ &= \hbar \omega_1 \sigma_1^{(M)\dagger} \sigma_1^{(M)} + \hbar \omega_q \left(\sigma_2^{(M)\dagger} \sigma_2^{(M)} + \sum_{i=1}^N \sigma_q^{(i)\dagger} \sigma_q^{(i)} \right) + \hbar \omega_S \sigma_3^{(M)\dagger} \sigma_3^{(M)}. \end{aligned} \quad (4.2)$$

As discussed above, to each atomic transition corresponds a transition dipole moment induced by the electromagnetic field: the dipole related to the transition τ of atom a is labeled $\boldsymbol{\mu}_{\tau}^{(a)}$. Moreover, the position of atom a is noted by \mathbf{r}_a , and the electric field at this point is $\mathbf{E}(\mathbf{r}_a)$. Under the dipolar approximation, the Hamiltonian describing the interactions between the set of atomic transitions and the environmental electromagnetic field is

$$H_{\text{int}} = - \sum_{\tau} (\sigma_{\tau}^{(a)} + \sigma_{\tau}^{(a)\dagger}) \boldsymbol{\mu}_{\tau}^{(a)} \cdot \mathbf{E}(\mathbf{r}_a). \quad (4.3)$$

The system parameters are such that the quantum-system-field interactions can be treated in the weak-coupling limit, and the Born-Markov and rotating-wave approximations can be applied, as detailed in Chapter 1. More precisely, the configuration producing the smallest relaxation time scale occurs for the smallest slab-atoms distance and the larger slab temperature that we will be considering, which are $z = 0.1 \mu\text{m}$ and $T_S = 900 \text{ K}$. In this case, the transition ω_3 has the smallest relaxation time: $\tau_R \sim 3.2 \times 10^{-4} \text{ s}$, while ω_2 corresponds to the larger environmental decay time $\tau_B = \omega_2^{-1} \sim 1.2 \times 10^{-13} \text{ s}$, and to the larger $\tau_S \sim (2\omega_2)^{-1} \sim 6 \times 10^{-14} \text{ s}$. Then the two conditions $\tau_R \gg \tau_B$ and $\tau_R \gg \tau_S$ hold such that the Born-Markov and rotating-wave approximations can be applied. Thus, starting from the general Hamiltonian (4.1), the following Markovian quantum master equation can be used to determine the time evolution of $\rho(t)$, the reduced density matrix of the quantum system,

$$\frac{d\rho(t)}{dt} = -\frac{i}{\hbar} [H_S + H_{\Lambda}, \rho(t)] + \sum_a \sum_{\tau} \mathcal{D}_{\tau}^{(a)}[\rho(t)] + \sum_{a \neq b} \mathcal{D}_{\text{res}}^{(ab)}[\rho(t)] \quad (4.4)$$

where $a, b \in \{M, 1, \dots, N\}$. Let us briefly identify the different contributions involved in this equation. First of all, the operator H_{Λ} appearing in the commutator describes the field-induced coherent dipole-dipole interactions between two resonant transitions, which operate energy exchanges between subparts of the quantum system, conserving the energy of the total

system. This operator is expressed as

$$H_\Lambda = \hbar \sum_{i=1}^N \Lambda^{(Mi)}(\omega_q) \sigma_2^{(M)\dagger} \sigma_q^{(i)} + \text{H.c.} \\ + \hbar \sum_{i < j} \Lambda^{(ij)}(\omega_q) \sigma_q^{(i)\dagger} \sigma_q^{(j)} + \text{H.c.} \quad (4.5)$$

This expression involves interactions between the machine transition $\tau = 2$ and each qubit (first line), as well as between each pair of qubits (second line). Their strength is determined by the coefficient $\Lambda^{(ab)}(\omega_q)$ (with $a, b \in \{M, 1, \dots, N\}$), whose expression will be detailed later. The master-equation contributions not involved in the commutator describe dissipative processes, i.e., energy exchanges between the quantum system and the EM field. More precisely, the dissipation inherent to each individual transition reads

$$\mathcal{D}_\tau^{(a)}[\rho(t)] = \mathcal{D}_{\text{em}}^{(a)}(\omega_\tau)[\rho(t)] + \mathcal{D}_{\text{abs}}^{(a)}(\omega_\tau)[\rho(t)], \quad (4.6)$$

where $a \in \{M, 1, \dots, N\}$ and $\tau \in \{1, 2, 3, q\}$. On the other hand, $\mathcal{D}_{\text{res}}^{(ab)}$ with $a, b \in \{M, 1, \dots, N\}$, describes a collective behavior of a resonant-transition pair, and is defined as

$$\mathcal{D}_{\text{res}}^{(ab)}[\rho(t)] = \mathcal{D}_{\text{em}}^{(ab)}(\omega_q)[\rho(t)] + \mathcal{D}_{\text{abs}}^{(ab)}(\omega_q)[\rho(t)]. \quad (4.7)$$

These dissipative processes involve the absorption and emission super-operators whose definitions are given in Eqs. (1.33) and (1.34), respectively. Analogously to $\Lambda^{(ab)}(\omega_\tau)$ for the coherent interaction, the transition rates $\Gamma_{\text{abs}}^{(ab)}(\omega_\tau)$ and $\Gamma_{\text{em}}^{(ab)}(\omega_\tau)$ characterize the strength of the corresponding energy exchanges. These different coefficients originate from the correlations of the OTE EM field, which have been computed in Ref. [136] in terms of the slab scattering operators, and have been used in the framework of Casimir-Lifshitz force and heat transfer in OTE systems. In the following subsection, we briefly present the essential points of the derivation of these coefficients, which are crucial to determine the time evolution of the quantum system.

4.3.2 Auto-correlation functions of the OTE EM field

As discussed in Chap. 1, the different energy-exchange mechanisms occurring within the open system stem from the auto-correlation functions of the environmental EM field, through the coefficients $\Gamma_{\text{em}}^{(ab)}$, $\Gamma_{\text{abs}}^{(ab)}$ and $\Lambda^{(ab)}$ (for two generic atoms a, b). At thermal equilibrium, including $T = 0$ K, these functions can be deduced from the fluctuation-dissipation theorem. In the specific case of free-space, i.e. in the absence of matter, their analytical expressions are well-known and given by Eqs. (2.6) to (2.11) of Chap. 2. However, when the system is OTE, as is the case when $T_S \neq T_W$, the fluctuation-dissipation theorem does not hold, and the calculation of the electric field and its correlation functions is not trivial. Nonetheless,

their derivation has been performed in Ref. [136], based on the assumption of *local thermal equilibrium*. Each body, the walls and the slab in our case, is assumed to have a constant temperature, despite the presence of another (far-away) body of different temperature. The assumption consists in stating that the field emitted by each body is the same it would emit if it was at thermal equilibrium at its own temperature. The total EM field at any point in space results from the sum of the EM fields emitted by each body. In Ref. [136], which was dedicated to the study of Casimir-Lifshitz force and heat transfer OTE, the total EM field and its auto-correlation functions have been derived in the case of two bodies at different temperatures, having arbitrary shapes and dielectric properties, and both of them being embedded in a blackbody radiation at a third temperature. In the following, we express the auto-correlation functions in the simpler case of a single body in a blackbody radiation, firstly of arbitrary geometric and dielectric properties, and then in the specific case of a dielectric slab. Moreover, we will express the auto-correlation functions in terms of the body reflection and transmission operators, \mathcal{R} and \mathcal{T} , respectively.

Starting from the expression of the electric field at an arbitrary point \mathbf{r} (outside the body) and time t , $\mathbf{E}(\mathbf{r}, t)$, it can be decomposed with respect to frequency as

$$\mathbf{E}(\mathbf{r}, t) = 2\text{Re} \left[\int_0^{+\infty} \frac{d\omega}{2\pi} e^{-i\omega t} \mathbf{E}(\mathbf{r}, \omega) \right]. \quad (4.8)$$

Considering a transition of frequency ω_τ , this decomposition leads to the expression of the coefficients $\Gamma_{\text{em}}^{(ab)}(\omega_\tau)$, $\Gamma_{\text{abs}}^{(ab)}(\omega_\tau)$ and $\Lambda^{(ab)}(\omega_\tau)$ under the form [25]

$$\Gamma_{\text{em}}^{(ab)}(\omega_\tau) = \frac{1}{\hbar^2} \sum_{i,j} [\boldsymbol{\mu}_\tau^{(a)}]_i [\boldsymbol{\mu}_\tau^{(b)}]_j \langle E_i(\mathbf{r}_a, \omega_\tau) E_j^\dagger(\mathbf{r}_b, \omega_\tau) \rangle, \quad (4.9)$$

$$\Gamma_{\text{abs}}^{(ab)}(\omega_\tau) = \frac{1}{\hbar^2} \sum_{i,j} [\boldsymbol{\mu}_\tau^{(a)}]_i [\boldsymbol{\mu}_\tau^{(b)}]_j \langle E_i^\dagger(\mathbf{r}_a, \omega_\tau) E_j(\mathbf{r}_b, \omega_\tau) \rangle, \quad (4.10)$$

$$\Lambda^{(ab)}(\omega_\tau) = \frac{1}{\hbar^2} \sum_{i,j} [\boldsymbol{\mu}_\tau^{(a)}]_i [\boldsymbol{\mu}_\tau^{(b)}]_j \left[\mathcal{P} \int_0^{+\infty} \frac{d\omega'}{2\pi} \left(\frac{\langle E_i(\mathbf{r}_a, \omega') E_j^\dagger(\mathbf{r}_b, \omega') \rangle}{\omega_\tau - \omega'} + \frac{\langle E_i^\dagger(\mathbf{r}_a, \omega') E_j(\mathbf{r}_b, \omega') \rangle}{\omega_\tau + \omega'} \right) \right], \quad (4.11)$$

where \mathcal{P} indicates the principal part of the integral, and with the indexes a, b referring to generic atoms sharing a transition τ of frequency ω_τ . For $k = a, b$, and with $i, j \in \{x, y, z\}$, $[\boldsymbol{\mu}_\tau^{(k)}]_i$ and $E_i(\mathbf{r}_k, \omega_\tau)$ stand for the i -th Cartesian component of the dipole transition and of the electric-field mode at position \mathbf{r}_k , respectively. Following [25, 136], the anti-normally and normally ordered correlation functions between electric-field components of frequency ω at

points \mathbf{r}_a and \mathbf{r}_b , read

$$\langle E_i(\mathbf{r}_a, \omega) E_j^\dagger(\mathbf{r}_b, \omega) \rangle = \frac{\hbar \omega^3}{3\pi \varepsilon_0 c^3} \left\{ \left(1 + n(\omega, T_W)\right) [\alpha_W^{(ab)}(\omega)]_{ij} + \left(1 + n(\omega, T_S)\right) [\alpha_S^{(ab)}(\omega)]_{ij} \right\}, \quad (4.12)$$

$$\langle E_i^\dagger(\mathbf{r}_a, \omega) E_j(\mathbf{r}_b, \omega) \rangle = \frac{\hbar \omega^3}{3\pi \varepsilon_0 c^3} \left\{ n(\omega, T_W) [\alpha_W^{(ab)*}(\omega)]_{ij} + n(\omega, T_S) [\alpha_S^{(ab)*}(\omega)]_{ij} \right\}, \quad (4.13)$$

where it has been assumed that the two points $\mathbf{r}_a = (\mathbf{r}_a^\perp, z_a)$ and $\mathbf{r}_b = (\mathbf{r}_b^\perp, z_b)$ are located on the right side of the body ($z_a, z_b > 0$). It is worth stressing that the two temperatures involved in the system are contributing through $n(\omega, T) = [\exp(\hbar\omega/k_B T) - 1]^{-1}$, which characterizes the mean number of thermal photons at frequency ω and temperature T . Additionally, the coefficients $[\alpha_S^{(ab)}(\omega)]_{ij}$ and $[\alpha_W^{(ab)}(\omega)]_{ij}$ have been introduced: they correspond to the contribution of the body (α_S) and of the walls (α_W) to the correlation functions. They are expressed in terms of the body scattering operators, \mathcal{R} and \mathcal{T} , which encapsulate the body dielectric and geometric properties.

Before giving the explicit expression of these two coefficients, it is necessary to decompose the electric field in terms of plane waves propagating along the z -axis, upon which the scattering operators will act. Each plane wave is characterized by its frequency ω and its wave vector $\mathbf{K}^\phi = (\mathbf{k}, \phi k_z \hat{\mathbf{z}})$, where $\mathbf{k} = (k_x \hat{\mathbf{x}}, k_y \hat{\mathbf{y}})$ denotes the transverse wave vector. The parameter $\phi \in \{+, -\}$ describes the propagation direction along the z -axis: $\phi = +$ ($\phi = -$) for waves propagating towards increasing- z (decreasing- z). Finally, the wave polarization is described by $p \in \{1, 2\}$, with $p = 1$ ($p = 2$) standing for transverse-electric (TE) [transverse-magnetic (TM)] polarization. A single mode of the electric field is entirely identified by the parameters $(\omega, \mathbf{k}, p, \phi)$, where $k_z^2 = \frac{\omega^2}{c^2} - k^2$, and with $k = |\mathbf{k}|$. Then, the wave-vector decomposition of an electric-field frequency component reads

$$\mathbf{E}(\mathbf{r}, \omega) = \sum_\phi \sum_p \int_{-\infty}^{+\infty} \frac{d^2 \mathbf{k}}{(2\pi)^2} e^{i \mathbf{K}^\phi \cdot \mathbf{r}} \hat{\mathbf{e}}_p^\phi(\mathbf{k}, \omega) E_p^\phi(\mathbf{k}, \omega), \quad (4.14)$$

with $E_p^\phi(\mathbf{k}, \omega)$ denoting the mode amplitude, and with the polarization unit vectors $\hat{\mathbf{e}}_1^\phi(\mathbf{k}, \omega) = \hat{\mathbf{e}}_{\text{TE}}^\phi(\mathbf{k}, \omega)$ and $\hat{\mathbf{e}}_2^\phi(\mathbf{k}, \omega) = \hat{\mathbf{e}}_{\text{TM}}^\phi(\mathbf{k}, \omega)$, defined as

$$\hat{\mathbf{e}}_{\text{TE}}^\phi(\mathbf{k}, \omega) = \hat{\mathbf{z}} \times \hat{\mathbf{k}} = \frac{1}{k} (-k_y \hat{\mathbf{x}} + k_x \hat{\mathbf{y}}), \quad (4.15)$$

$$\hat{\mathbf{e}}_{\text{TM}}^\phi(\mathbf{k}, \omega) = \frac{c}{\omega} \hat{\mathbf{e}}_{\text{TE}}^\phi(\mathbf{k}, \omega) \times \mathbf{K}^\phi = \frac{c}{\omega} (-k \hat{\mathbf{z}} + \phi k_z \hat{\mathbf{k}}). \quad (4.16)$$

The operators \mathcal{R} and \mathcal{T} act on each components of the field impinging the body, and result in an outgoing field in agreement with its scattering properties. A specific example will be given further, when the role of the body is played by a slab. Before that, the coefficients $[\alpha_W^{(ab)}(\omega)]_{ij}$ and $[\alpha_S^{(ab)}(\omega)]_{ij}$ introduced above, valid for a body of arbitrary shape and dielectric properties,

can be expressed

$$\begin{aligned}
 [\alpha_W^{(ab)}(\omega)]_{ij} = & \frac{3\pi c}{2\omega} \sum_{p,p'} \int \frac{d^2 \mathbf{k}}{(2\pi)^2} \int \frac{d^2 \mathbf{k}'}{(2\pi)^2} e^{i(\mathbf{k} \cdot \mathbf{r}_a^\perp - \mathbf{k}' \cdot \mathbf{r}_b^\perp)} \langle p, \mathbf{k} | \\
 & \times \left\{ e^{i(k_z z_a - k'_z z_b)} [\hat{\epsilon}_p^+(\mathbf{k}, \omega)]_i [\hat{\epsilon}_{p'}^+(\mathbf{k}', \omega)]_j^* (\mathcal{T} \mathcal{P}_{-1}^{(\text{pw})} \mathcal{T}^\dagger + \mathcal{R} \mathcal{P}_{-1}^{(\text{pw})} \mathcal{R}^\dagger) \right. \\
 & + e^{i(k_z z_a + k'_z z_b)} [\hat{\epsilon}_p^+(\mathbf{k}, \omega)]_i [\hat{\epsilon}_{p'}^-(\mathbf{k}', \omega)]_j^* \mathcal{R} \mathcal{P}_{-1}^{(\text{pw})} \\
 & + e^{-i(k_z z_a + k'_z z_b)} [\hat{\epsilon}_p^-(\mathbf{k}, \omega)]_i [\hat{\epsilon}_{p'}^+(\mathbf{k}', \omega)]_j^* \mathcal{P}_{-1}^{(\text{pw})} \mathcal{R}^\dagger \\
 & \left. + e^{-i(k_z z_a - k'_z z_b)} [\hat{\epsilon}_p^-(\mathbf{k}, \omega)]_i [\hat{\epsilon}_{p'}^-(\mathbf{k}', \omega)]_j^* \mathcal{P}_{-1}^{(\text{pw})} \right\} |p', \mathbf{k}'\rangle, \quad (4.17)
 \end{aligned}$$

$$\begin{aligned}
 [\alpha_S^{(ab)}(\omega)]_{ij} = & \frac{3\pi c}{2\omega} \sum_{p,p'} \int \frac{d^2 \mathbf{k}}{(2\pi)^2} \int \frac{d^2 \mathbf{k}'}{(2\pi)^2} e^{i(\mathbf{k} \cdot \mathbf{r}_a^\perp - \mathbf{k}' \cdot \mathbf{r}_b^\perp)} \langle p, \mathbf{k} | e^{i(k_z z_a - k'_z z_b)} [\hat{\epsilon}_p^+(\mathbf{k}, \omega)]_i \\
 & \times [\hat{\epsilon}_{p'}^+(\mathbf{k}', \omega)]_j^* \left\{ \mathcal{P}_{-1}^{(\text{pw})} - \mathcal{R} \mathcal{P}_{-1}^{(\text{pw})} \mathcal{R}^\dagger + \mathcal{R} \mathcal{P}_{-1}^{(\text{ew})} - \mathcal{P}_{-1}^{(\text{ew})} \mathcal{R}^\dagger - \mathcal{T} \mathcal{P}_{-1}^{(\text{pw})} \mathcal{T}^\dagger \right\} |p', \mathbf{k}'\rangle. \quad (4.18)
 \end{aligned}$$

Both of these coefficients depend on the separation between quantum-emitter coordinates \mathbf{r}_a and \mathbf{r}_b . In addition, the parameters z_a and z_b take into account the distance between each emitter and the body. The operators $\mathcal{P}_{-1}^{(\text{pw})}$ and $\mathcal{P}_{-1}^{(\text{ew})}$ are defined through

$$\langle p, \mathbf{k} | \mathcal{P}_{-1}^{(\text{pw})} | p', \mathbf{k}' \rangle = (k_z)^{-1} \langle p, \mathbf{k} | \Pi^{(\text{pw})} | p', \mathbf{k}' \rangle, \quad (4.19)$$

$$\langle p, \mathbf{k} | \mathcal{P}_{-1}^{(\text{ew})} | p', \mathbf{k}' \rangle = (k_z)^{-1} \langle p, \mathbf{k} | \Pi^{(\text{ew})} | p', \mathbf{k}' \rangle, \quad (4.20)$$

where $\Pi^{(\text{pw})}$ and $\Pi^{(\text{ew})}$ are projectors into the propagative ($\omega/c \geq k$) and evanescent ($k > \omega/c$) sectors, respectively. By considering the atomic transition τ , we introduce the coefficients

$$\alpha_W^{(ab)}(\omega_\tau) = \sum_{i,j} [\hat{\boldsymbol{\mu}}_\tau^{(a)}]_i^* [\hat{\boldsymbol{\mu}}_\tau^{(b)}]_j [\alpha_W^{(ab)}(\omega_\tau)]_{ij}, \quad (4.21)$$

$$\alpha_S^{(ab)}(\omega_\tau) = \sum_{i,j} [\hat{\boldsymbol{\mu}}_\tau^{(a)}]_i^* [\hat{\boldsymbol{\mu}}_\tau^{(b)}]_j [\alpha_S^{(ab)}(\omega_\tau)]_{ij}, \quad (4.22)$$

which take into account the dipole orientations of atoms a and b through $\hat{\boldsymbol{\mu}}_\tau^{(k)} = \boldsymbol{\mu}_\tau^{(k)} / |\boldsymbol{\mu}_\tau^{(k)}|$ for $k = a, b$. Finally, the transition rates can be expressed as

$$\boxed{\Gamma_{\text{em}}^{(ab)}(\omega_\tau) = \sqrt{\gamma_0^{(a)}(\omega_\tau) \gamma_0^{(b)}(\omega_\tau)} \left([1 + n(\omega_\tau, T_W)] \alpha_W^{(ab)}(\omega_\tau) + [1 + n(\omega_\tau, T_S)] \alpha_S^{(ab)}(\omega_\tau) \right), \quad (4.23)$$

$$\boxed{\Gamma_{\text{abs}}^{(ab)}(\omega_\tau) = \sqrt{\gamma_0^{(a)}(\omega_\tau) \gamma_0^{(b)}(\omega_\tau)} \left(n(\omega_\tau, T_W) \alpha_W^{(ab)}(\omega_\tau)^* + n(\omega_\tau, T_S) \alpha_S^{(ab)}(\omega_\tau)^* \right), \quad (4.24)$$

where $\gamma_0^{(k)}(\omega_\tau) = \frac{|\boldsymbol{\mu}_\tau^{(k)}|^2 \omega_\tau^3}{3\pi \hbar \epsilon_0 c^3}$ for $k = a, b$, is the rate of spontaneous emission in vacuum, involving the dipole magnitudes.

Concerning the strength of the hopping flux [Eq. (1.45)], it can be decomposed as the sum of a free-space and a matter contributions [25], $\Lambda_0^{(ab)}(\omega_\tau)$ and $\Lambda_{\text{ref}}^{(ab)}(\omega_\tau)$, the latter originating from reflection on the body surface:

$$\Lambda^{(ab)}(\omega_\tau) = \Lambda_0^{(ab)}(\omega_\tau) + \Lambda_{\text{ref}}^{(ab)}(\omega_\tau). \quad (4.25)$$

The free-space contribution is [25, 26]

$$\begin{aligned} \Lambda_0^{(ab)}(\omega_\tau) = & -\frac{3}{4} \sqrt{\gamma_0^{(a)}(\omega_\tau) \gamma_0^{(b)}(\omega_\tau)} \left\{ 2(\hat{\boldsymbol{\mu}}^{(a)*} \cdot \hat{\mathbf{r}}_{ab})(\hat{\boldsymbol{\mu}}^{(b)} \cdot \hat{\mathbf{r}}_{ab}) f(\tilde{r}_{ab}) \right. \\ & \left. + \left[\hat{\boldsymbol{\mu}}^{(a)*} \cdot \hat{\boldsymbol{\mu}}^{(b)} - (\hat{\boldsymbol{\mu}}^{(a)*} \cdot \hat{\mathbf{r}}_{ab})(\hat{\boldsymbol{\mu}}^{(b)} \cdot \hat{\mathbf{r}}_{ab}) \right] g(\tilde{r}_{ab}) \right\}, \\ f(x) = & \frac{\cos x + x \sin x}{x^3}, \quad g(x) = \frac{(x^2 - 1) \cos x - x \sin x}{x^3}. \end{aligned} \quad (4.26)$$

where $\mathbf{r}_{ab} = \mathbf{r}_b - \mathbf{r}_a$, $\hat{\mathbf{r}}_{ab} = \mathbf{r}_{ab}/|\mathbf{r}_{ab}|$ and $\tilde{r}_{ab} = r_{ab}\omega_\tau/c$. In the case of identical dipoles ($\boldsymbol{\mu}_\tau^{(a)} = \boldsymbol{\mu}_\tau^{(b)}$), this equation reduces to Eq. (2.6) of Chap. 2. The body contribution to the coherent interaction is

$$\Lambda_{\text{ref}}^{(ab)}(\omega_\tau) = \sum_{i,j} \boldsymbol{\mu}_i^{(a)*} \boldsymbol{\mu}_j^{(b)} \left[\Lambda_{\text{ref}}^{(ab)}(\omega_\tau) \right]_{ij}, \quad (4.27)$$

where the coefficient $\left[\Lambda_{\text{ref}}^{(ab)}(\omega_\tau) \right]_{ij}$ is expressed in terms of the reflection operator. For a generic frequency ω , it reads

$$\begin{aligned} \left[\Lambda_{\text{ref}}^{(ab)}(\omega) \right]_{ij} = & -\frac{i\omega^2}{4\varepsilon_0 \hbar c^2} \sum_{p,p'} \int \frac{d^2 \mathbf{k}}{(2\pi)^2} \int \frac{d^2 \mathbf{k}'}{(2\pi)^2} e^{i(\mathbf{k} \cdot \mathbf{r}_a^\perp - \mathbf{k}' \cdot \mathbf{r}_b^\perp)} \langle p, \mathbf{k} | \\ & \times \left\{ e^{i(k_z z_a + k'_z z_b)} [\hat{\boldsymbol{\epsilon}}_p^+(\mathbf{k}, \omega)]_i [\hat{\boldsymbol{\epsilon}}_{p'}^-(\mathbf{k}', \omega)]_j^* \mathcal{R} \mathcal{P}_{-1}^{(\text{pw})} \right. \\ & - e^{-i(k_z z_a + k'_z z_b)} [\hat{\boldsymbol{\epsilon}}_p^-(\mathbf{k}, \omega)]_i [\hat{\boldsymbol{\epsilon}}_{p'}^+(\mathbf{k}', \omega)]_j^* \mathcal{P}_{-1}^{(\text{pw})} \mathcal{R}^\dagger \\ & \left. + e^{i(k_z z_a - k'_z z_b)} [\hat{\boldsymbol{\epsilon}}_p^+(\mathbf{k}, \omega)]_i [\hat{\boldsymbol{\epsilon}}_{p'}^+(\mathbf{k}', \omega)]_j^* (\mathcal{R} \mathcal{P}_{-1}^{(\text{ew})} + \mathcal{P}_{-1}^{(\text{ew})} \mathcal{R}^\dagger) \right\} |p', \mathbf{k}' \rangle. \end{aligned} \quad (4.28)$$

It is worth pointing out that unlike the dissipative rates (4.23) and (4.24), the coherent interaction does not depend on the temperatures involved in the system.

As discussed before, Eqs. (4.23), (4.24) and (4.28) introduced above are suitable for a body with arbitrary geometry and dielectric properties since the operators \mathcal{R} and \mathcal{T} , which encapsulate these properties, are general. In the specific case of a dielectric slab of permittivity $\varepsilon(\omega)$, these operators connect two modes of the EM field as

$$\begin{aligned} \langle p, \mathbf{k} | \mathcal{R} | p', \mathbf{k}' \rangle &= (2\pi)^2 \delta(\mathbf{k} - \mathbf{k}') \delta_{pp'} \rho_p(\mathbf{k}, \omega), \\ \langle p, \mathbf{k} | \mathcal{T} | p', \mathbf{k}' \rangle &= (2\pi)^2 \delta(\mathbf{k} - \mathbf{k}') \delta_{pp'} \tau_p(\mathbf{k}, \omega), \end{aligned} \quad (4.29)$$

where the coefficients $\rho_p(\mathbf{k}, \omega)$ and $\tau_p(\mathbf{k}, \omega)$ are defined as

$$\rho_p(\mathbf{k}, \omega) = r_p(\mathbf{k}, \omega) \frac{1 - e^{2ik_{zm}\delta}}{1 - r_p^2(\mathbf{k}, \omega)e^{2ik_{zm}\delta}}, \quad \tau_p(\mathbf{k}, \omega) = \frac{(1 - r_p^2(\mathbf{k}, \omega))e^{i(k_{zm}-k_z)\delta}}{1 - r_p^2(\mathbf{k}, \omega)e^{2ik_{zm}\delta}}, \quad (4.30)$$

where $k_{zm} = \sqrt{\varepsilon(\omega)\omega^2/c^2 - k^2}$ is the z -component of the wave vector inside of the medium. Equations (4.30) correspond to the slab coefficients of reflection and transmission, taking into account its finite thickness δ , and stem from the Fresnel coefficients

$$r_{\text{TE}}(\mathbf{k}, \omega) = \frac{k_z - k_{zm}}{k_z + k_{zm}}, \quad r_{\text{TM}}(\mathbf{k}, \omega) = \frac{\epsilon(\omega)k_z - k_{zm}}{\epsilon(\omega)k_z + k_{zm}}, \quad (4.31)$$

To summarize, we have expressed the coefficients involved in the master equation of the system, each of them being associated to a specific interaction (photon emission/absorption, hopping). All of these coefficients depend on the slab material and thickness, and the dissipative processes also depend on the walls and slab temperatures. Moreover, the spatial coordinates as well as the dipole magnitudes and orientations are also relevant, as they affect the interactions both between the environment and the system, and inside the system, between atoms.

4.4 Three-level atom as quantum thermal machine

4.4.1 Environmental and population temperatures

In classical physics, according to the first law of thermodynamics, the energy variation of a system can be expressed as the sum of a work and a heat contributions. In Chap. 1, we have shown that a quantum version of this law can be formulated once the notions of heat and work have been defined in the quantum framework. Moreover, we have demonstrated that, no work being involved in the systems we are considering, any energy variation occurs through a heat flux. In classical physics, the notion of heat flux is deeply related to the one of temperature: a heat flux spontaneously arises between two bodies at different temperatures, transferring energy from the hotter one to the colder one, until thermal equilibrium is reached. Although we have introduced a definition of quantum heat flux, the notion of temperature in the quantum framework still needs to be specified. This section is dedicated to the introduction of two different definitions of temperatures: one will be associated to an atomic transition, and the other one to the field mode interacting with this transition. These will help us describing and understanding the interplay of energy fluxes taking place in our system.

These two temperatures are based on the property mentioned above, namely the appearance of a (quantum) heat flux between two bodies at different temperatures, flowing from the hotter one to the colder one. To this end, we consider the local heat flux of a generic atom a ,

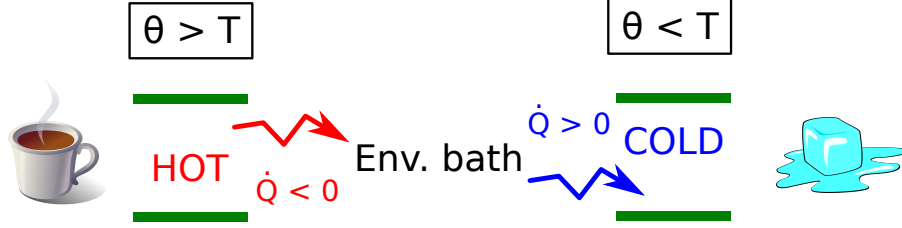


Figure 4.3: Illustrations of hot and cold transitions: When the population temperature of the transition is greater than the environmental temperature of EM-field mode at this frequency ($\theta > T$), a heat flux arises and releases energy from the transition to the field, thereby decreasing the quantum-system energy ($\dot{Q} < 0$). In the opposite case ($\theta < T$), the transition absorbs energy from the field which increases the open-system energy ($\dot{Q} > 0$).

between its transition τ and the environmental EM field, which can be put under the form

$$\dot{Q}_{\text{loc}}^{(a)}(\omega_\tau) = X(\omega_\tau) \left(e^{\hbar\omega_\tau/k_B\theta_\tau^{(a)}} - e^{\hbar\omega_\tau/k_BT_\tau^{(a)}} \right), \quad (4.32)$$

with $X(\omega_\tau) > 0$, and where the two quantities $T_\tau^{(a)}$ and $\theta_\tau^{(a)}$ are the two different temperatures we will be considering. Not only they both have the dimension of a temperature, but also the relation between them ($T_\tau^{(a)} \gtrless \theta_\tau^{(a)}$) settles the sign of the heat flux $\dot{Q}_{\text{loc}}^{(a)}(\omega_\tau)$, as required. The expressions and physical interpretations of these temperatures are detailed below.

On the one hand, the so-called *environmental temperature* reads

$$T_\tau^{(a)} = \frac{\hbar\omega_\tau}{k_B \ln \left[\Gamma_{\text{em}}^{(a)}(\omega_\tau) / \Gamma_{\text{abs}}^{(a)}(\omega_\tau) \right]}. \quad (4.33)$$

It characterizes the temperature of the EM-field mode at frequency ω_τ , and depends on the transitions rates $\Gamma_{\text{abs/em}}^{(a)}(\omega_\tau)$, which stem from the complex structure of the field. $T_\tau^{(a)}$ is an effective temperature, associable to the thermal-equilibrium temperature of an effective bath producing the same transition rates. When the system is OTE, in general, two different field modes have different environmental temperatures. For example, the three machine transitions $\tau = \{1, 2, 3\}$ usually interact with field modes having different environmental temperatures: $T_1^{(M)} \neq T_2^{(M)} \neq T_3^{(M)}$, such that each transition can be viewed as interacting with an effective bath at thermal equilibrium at $T_1^{(M)}$, $T_2^{(M)}$ and $T_3^{(M)}$, respectively. In the particular case of thermal equilibrium between the slab and the walls ($T_S = T_W = T_{\text{eq}}$), all of the environmental temperatures reduce to T_{eq} ($T_1^{(M)} = T_2^{(M)} = T_3^{(M)} = T_{\text{eq}}$). On the other hand, the function $\theta_\tau^{(a)}$ characterizes the *population temperature*, defined as

$$\theta_\tau^{(a)} = \frac{\hbar\omega_\tau}{k_B \ln \left[p_g^{(a)}(\omega_\tau) / p_e^{(a)}(\omega_\tau) \right]}, \quad (4.34)$$

where $p_g^{(a)}(\omega_\tau)$ and $p_e^{(a)}(\omega_\tau)$ are the ground and excited state populations of transition τ , respectively. $\theta_\tau^{(a)}$ describes the energy distribution of a transition. More specifically, in the limit of a transition in its ground state, namely $p_g^{(a)}(\omega_\tau) \rightarrow 1$, then $\theta_\tau^{(a)} \rightarrow 0$ K. With the increase of the excited population, the temperature increases as well, until it diverges in the case of equally populated states [$p_g^{(a)}(\omega_\tau) = p_e^{(a)}(\omega_\tau)$]. It is worth stressing that this definition may lead to a negative $\theta_\tau^{(a)} < 0$ K. This condition indicates as usual that the transition is under population inversion: the excited state is more populated than the ground one [$p_g^{(a)}(\omega_\tau) < p_e^{(a)}(\omega_\tau)$].

As mentioned before, and stemming from Eq. (4.32), the heat-flux direction between a transition and its environment (i.e. the field mode at the same frequency) is determined by the relation between population and environmental temperatures Fig. 4.3. More precisely, we speak of *hot transition* when $\theta_\tau^{(a)} > T_\tau^{(a)}$, in which case the transition loses energy to the EM field ($\dot{Q}^{(a)}(\omega_\tau) < 0$), whereas for a *cold transition* ($\theta_\tau^{(a)} < T_\tau^{(a)}$), energy is drawn from the field to the transition ($\dot{Q}^{(a)}(\omega_\tau) > 0$). Finally, in case of thermal equilibrium between the transition and its environment ($\theta_\tau^{(a)} = T_\tau^{(a)}$), each photon emission is compensated by a photon absorption [$\Gamma_{\text{em}}^{(a)}(\omega_\tau)p_e^{(a)}(\omega_\tau) = \Gamma_{\text{abs}}^{(a)}(\omega_\tau)p_g^{(a)}(\omega_\tau)$], such that the mean value of energy exchanged is $\dot{Q}^{(a)}(\omega_\tau) = 0$.

It is worth stressing the distinction between thermal equilibrium of slab and walls temperatures ($T_S = T_W = T_{\text{eq}}$) and in terms of population and environmental temperatures ($\theta_\tau^{(a)} = T_\tau^{(a)}$). The former describes thermal equilibrium of the EM field surrounding the quantum system. In this peculiar configuration, the emission and absorption rates of all atomic transitions depend only on the temperature T_{eq} , such that all the environmental temperatures collapse to T_{eq} . It follows that the atomic energy-level populations follow a Boltzmann distribution ($p^{(a)}(\omega_\tau) = \exp(-\hbar\omega_\tau/k_B T_{\text{eq}})/Z$, where Z is the partition function), in which case $\theta_\tau^{(a)} = T_\tau^{(a)}$. Then, $T_S = T_W = T_{\text{eq}}$ necessarily induces thermal equilibrium between the transitions and their environment: $\theta_\tau^{(a)} = T_\tau^{(a)} = T_{\text{eq}}$. On the other hand, the OTE configuration $T_S \neq T_W$ does not necessarily lead to $\theta_\tau^{(a)} \neq T_\tau^{(a)}$. For example, let us consider a single qubit embedded in the OTE EM field. The corresponding environmental temperature $T_\tau^{(a)}$ is an effective quantity, depending on both T_S and T_W . Nevertheless, the energy distribution of the transition is only regulated by $T_\tau^{(a)}$, leading to the thermalization of the population temperature to the environmental one ($\theta_\tau^{(a)} = T_\tau^{(a)}$). However, in the case of an atom with more than two levels, each transition has generally its own environmental temperature, as illustrated previously with the machine example. Then, the atomic populations do not follow a Boltzmann distribution, and $\theta_\tau^{(a)} \neq T_\tau^{(a)}$.

In the following sections, we use these notions of temperatures, and hot/cold atomic transitions to discuss the interactions between the machine and the qubit(s).

4.4.2 Three-level atom in an OTE field as thermal machine

In this section, we briefly explain the functioning of the three-level atom acting as a thermal machine, performing at steady state a thermal task on a single qubit. The analysis of this system, and its interpretation in the framework of quantum thermodynamics, has been performed in Ref. [18]. We will focus on the specific case where M plays the role of refrigerator, cooling down the qubit, but the mechanism of the reverse process (heating) is similar.

To begin with an even more elementary system, we temporarily put aside the qubit, and start focusing on a system where only the machine is present. Let us consider the case where the EM field surrounding the machine is OTE ($T_S \neq T_W$), such that the machine transitions perceive different environmental temperatures: $T_1^{(M)} \neq T_2^{(M)} \neq T_3^{(M)}$. We dedicate our attention to the system at stationarity, in which case the energy conservation imposes to the different machine energy exchanges to equilibrate. As discussed before, these are realized through heat fluxes, one for each transition, and their direction is settled by the relation between their corresponding population and environmental temperatures, namely $\theta_\tau^{(M)}$ and $T_\tau^{(M)}$, where here $\tau \in \{1, 2, 3\}$. We first focus to the flux related to the transition $\tau = 3$, i.e., the one with the largest energy ($\omega_3 = \omega_1 + \omega_2$). We make the assumption that the field-machine interactions have led to a stationary configuration where $\theta_3^{(M)} > T_3^{(M)}$. This is verified for a number of system setups, and we will see later that this amounts to assume that the machine is acting as a refrigerator. This relation tells us that the transition is hotter than its environment, therefore releasing energy into the EM field ($\dot{Q}_{\text{loc}}^{(M)}(\omega_3) < 0$). By energy conservation, the two other transitions draw energy from the field to compensate this loss: their respective heat fluxes are positive ($\dot{Q}_{\text{loc}}^{(M)}(\omega_\eta) > 0$, with $\eta = 1, 2$), meaning that they are both colder than their environment ($\theta_\eta^{(M)} < T_\eta^{(M)}$).

Let us now take into account the qubit, labeled 1. In the previous section, we explained that when such an atom is isolated in an EM field, its population temperature thermalizes to its environmental temperature ($\theta_q^{(1)} = T_q^{(1)}$), which depends on T_S and T_W . However, we are now considering a stationary system with both the machine and the qubit, involving the atomic transitions $\tau = \{1, 2, 3, q\}$. We recall that transitions $\tau = 2$ and $\tau = q$ are resonant ($\omega_2 = \omega_q$). Their dipoles and the atomic positions with respect to the slab are assumed to be equivalent, such that they interact similarly with the EM field: $T_2^{(M)} = T_q^{(1)}$. Moreover, if the dipoles are not orthogonal, this resonance allows the machine and atom 1 to interact with each other, thereby putting in contact the transition $\tau = q$, which would be at $\theta_q^{(1)} = T_q^{(1)} = T_2^{(M)}$ in the absence of the machine, with the machine transition $\tau = 2$, which is cold ($\theta_2^{(M)} < T_2^{(M)} = T_q^{(1)}$). As a consequence, a heat flux arises between them, a hopping flux, transferring energy from the qubit to the machine ($\dot{Q}_{\text{hop}}^{(M1)}(\omega_q) = -\dot{Q}_{\text{hop}}^{(1M)}(\omega_q) > 0$), in the attempt to equilibrate their energy distribution, or, in other words, to bring these transitions at thermal equilibrium, in terms of population temperatures. This mechanism leads to a stationary configuration where $\theta_q^{(1)} < T_q^{(1)}$: the transition of atom 1 is maintained cold under

the action of the machine. The population temperature of transition $\tau = 2$, on the other hand, is poorly affected by the energy drawn from the qubit. This is due to the fluxes interplay involving the other machine transitions: the absorbed energy is released into the environment through the flux of transition $\tau = 3$.

Three remarks are in order concerning the mechanism described above. Firstly, when we considered the machine in the absence of qubit, the transition $\tau = 2$ gained energy exclusively by local heat flux. Here, in the presence of atom 1, this flux is still active but is less intense, and its reduction is compensated by the energy drawn by hopping. Secondly, to be rigorous, the non-local heat flux between the couple $(M, 1)$ and the field must also be taken into account. In most of the cases we will consider in this Chapter, the energy involved with this flux does not play a significant role, and thus can be neglected in the description of the cooling process. However, it must be noted that this flux takes part in the expression of the Carnot efficiency associated to this system [18]. Finally, the hopping flux between the machine and atom 1 is proportional to the imaginary part of the quantum coherence between the states $|1e_1\rangle$ and $|2g_1\rangle$ [Eq. (1.45)].

An analogy can be drawn between our quantum system and a classical refrigerator, highlighted in Fig. 4.4. A classical refrigerator transfers energy, with the help of an energy supply (usually work, but not necessarily [137]), from a cold reservoir (the food) into a hot reservoir (the kitchen), under the form of heat. In our case, the food is identified to the transition of the qubit, while the machine transition $\tau = 3$ corresponds to the fridge spiral through which energy is released to the kitchen, the field mode characterized by the temperature T_3 . The hopping flux between transitions $\tau = 2$ and $\tau = q$ performs the thermal task, i.e., transfers energy from atom 1 to transition $\tau = 3$. The energy supply is provided by the local fluxes of both transitions $\tau = 1$ and $\tau = 2$. Moreover, the transition $\tau = 2$ also corresponds to the inside of the refrigerator, as it is in contact with the food. In Ref. [18], considering the machine acting on a single qubit, it has been shown that the efficiency at maximum power can reach values remarkably close to the Carnot efficiency, in which case quantum discord between the qubit and the machine is particularly pronounced.

Finally, instead of cooling down the qubit, the machine can instead yield energy to it, thereby heating it up. In this case, the heat flux direction of each transition is reversed. In other words, the relation between population and environmental temperatures of each transition is the following: transition $\tau = 3$ is cold, while in counterpart $\tau = 2$ and $\tau = 1$ are hot, allowing them to release the energy absorbed by $\tau = 3$, either in the field (for both transitions) or to atom 1 (only for $\tau = 2$), the latter case corresponding to the heating process.

4.5 Role of correlations in thermodynamic tasks

Let us now investigate how the machine can affect the temperature of the target body when the latter is composed of $N > 1$ qubits. More precisely, we will start focusing on the case $N = 4$,

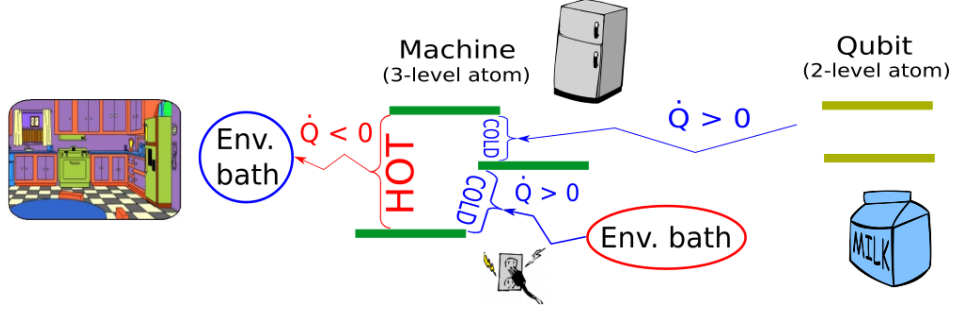


Figure 4.4: Illustration of the analogy between the three-level atom and a classical refrigerator. The two smallest transitions of the machine ($\tau = 1, 2$) are cold, and thus absorb energy from the field (Fig. 4.3). The smallest machine transition ($\tau = 2$) is also identified to the inside of the fridge. The qubit transition (the food) is resonant with the machine transition $\tau = 2$, inducing a heat flux transferring energy from the qubit to the machine. As a consequence, the qubit population temperature lowers: the qubit is refrigerated by the machine. The energy absorbed by the machine is released through its largest transition (the fridge spiral) to the EM-field mode (the kitchen) having the same frequency as the transition.

whose spatial distribution is represented in Fig. 4.2. In the numerical simulations presented throughout this Section, unless specified otherwise, the slab and walls temperatures have been chosen to $T_S = 900$ K and $T_W = 300$ K, respectively, and the machine–qubits distance set to $r = 0.8 \mu\text{m}$.

Although in the following we will essentially investigate temperatures $(T_\tau^{(a)}, \theta_\tau^{(a)}, \dots)$, we will not deal with them on their raw form, but rather with their inverse, for convenience (see further). In addition, being mainly interested in the resonant transitions $\tau = \{2, q\}$, we define $T_M^{-1} = T_2^{(M)-1}$, $\beta_M = \theta_2^{(M)-1}$ and $\beta_i = \theta_q^{(i)-1}$ for $i \in \{1, \dots, N\}$. In this way, the divergence occurring in the population temperatures [Eq.(4.34)] when $p_g^{(a)}(\omega_\tau) = p_e^{(a)}(\omega_\tau)$ disappears, corresponding to $\beta_a = 0$, for $a \in \{M, 1, \dots, N\}$. Moreover, we multiply these quantities by -1 to facilitate their interpretation: $-\beta_a$ increases with the transition energy, and population inversion corresponds to $-\beta_a > 0$. Also, notice that what we defined as hot (cold) transition, namely when $\theta_\tau^{(a)} > T_\tau^{(a)}$ ($\theta_\tau^{(a)} < T_\tau^{(a)}$), verifies $-\beta_a > -T_a^{-1}$ ($-\beta_a < -T_a^{-1}$). For all these reasons, we will work with $-T_M^{-1}$ and $-\beta_a$, which will be called ‘temperatures’, with a slight abuse of notation.

In the previous Section, we discussed the flux interplay leading the three-level atom to function either as a refrigerator or as a heating machine. This role is fixed by the interactions between this atom and the OTE EM field, as they determine whether the transition in contact with the qubits is hot or cold. Following [18], we explore a large number of configurations with different atom–field interactions by changing the parameter z , namely the distance between the slab and the plan containing the atomic system. Figure. 4.5 shows population and environmental temperatures of all the resonant transitions for $z \in [0.1, 100] \mu\text{m}$. This figure being very rich, we will decline its analysis in two steps, in order to have a clear comprehen-

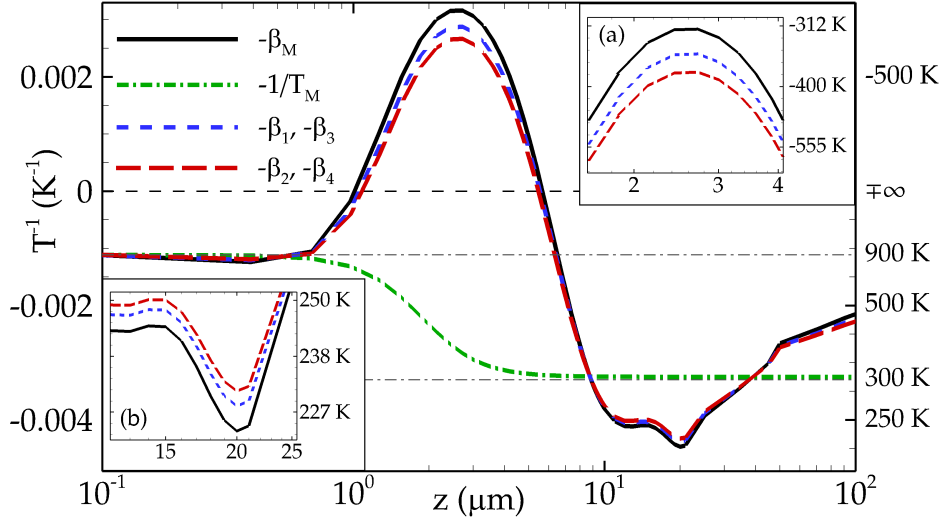


Figure 4.5: Left scale: Inverted population temperatures of all the resonant transitions ($-\beta_a$, $a \in \{M, 1, 2, 3, 4\}$), and machine environmental temperature ($-T_M^{-1}$), as a function of the slab-atom distance. Right scale: Temperatures in correspondence with the left scale. The slab and walls temperatures are represented by horizontal dash-dotted grey lines. Panels (a) and (b): zooms into the regions where heating and cooling regimes are the strongest, respectively.

sion. Firstly, we will investigate the z -dependence of the machine temperatures exclusively, and secondly, focus on the relations between these temperatures and the ones of the qubits.

Figure 4.5 pictures both environmental and population temperatures of the machine transition $\tau = 2$, namely, $-T_M^{-1}$ and $-\beta_M$, respectively. Let us start analyzing the environmental one with respect to z . When the quantum system is close to the slab ($z < 0.6 \mu\text{m}$), the contribution of the latter to the OTE EM field is much larger than the contributions coming from the walls, which is negligible. Consequently, the atomic environment is similar to an EM field at thermal equilibrium with the slab, leading to $T_M \simeq T_S$. On the other hand, the opposite scenario takes place when $z > 10 \mu\text{m}$: the field emitted by the slab eventually vanishes, in which case only the walls contribute to the EM field, such that $T_M \simeq T_W$. Between these two regions, when $z \in [0.6, 10] \mu\text{m}$, slab and walls contribute comparably to the field, leading to a smooth variation of T_M from T_S to T_W , as z increases.

Let us now compare $-T_M^{-1}$ to the population temperature of the machine, pictured by $-\beta_M$. In the region $z < 0.6 \mu\text{m}$, since the EM field is comparable to a thermal field at $T_M = T_S$, the transition $\tau = 2$ is at thermal equilibrium with its environment ($-\beta_M = -T_M^{-1}$). When z increases, however, the EM field is not similar to a field at thermal equilibrium anymore, and each machine transition has a different environmental temperature ($T_1^{(M)}$ and $T_3^{(M)}$ are not shown here). Consequently, the machine transitions are not at thermal equilibrium with their environments, and a heat-flux interplay arises. More specifically, when $z \in [0.6, 10] \mu\text{m}$, the

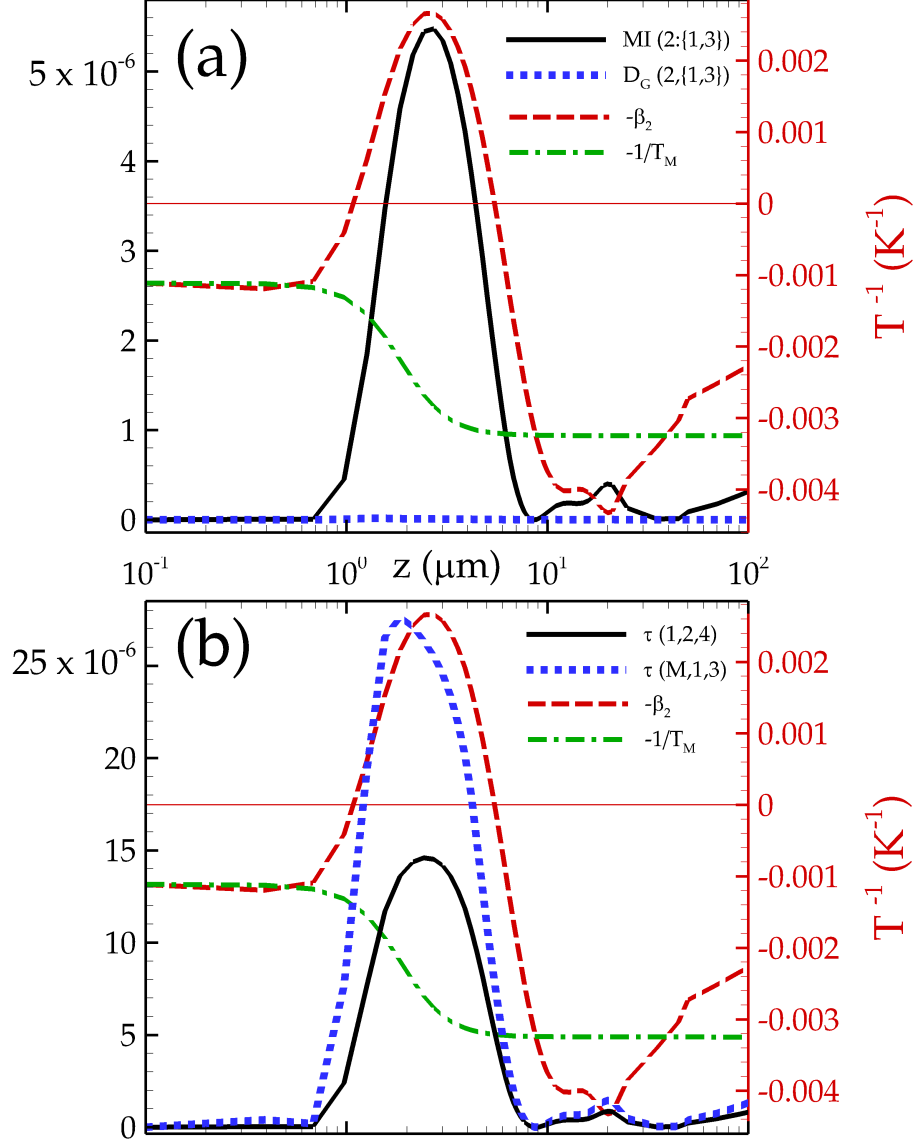


Figure 4.6: Panel (a): Left scale: Mutual information and geometric quantum discord of the bipartition $\{2 : (1,3)\}$. Panel (b): Left scale: tripartite mutual information of partitions $(M,1,3)$ and $(1,2,4)$. Both panels: Horizontal axis: slab-atoms distance. Right scale: Inverted population temperature of atom 2, and machine environmental temperature.

transition $\tau = 2$ enters a hot regime ($-\beta_M > -T_M^{-1}$). More remarkably, in the subinterval $z \in [1, 7] \mu\text{m}$, the quantity $-\beta_M$ is positive, signifying that the transition is undergoing population inversion: the excited state is more populated than the ground state [$p_e^{(M)}(\omega_2) > p_g^{(M)}(\omega_2)$]. On the other hand, within $z \in [10, 40] \mu\text{m}$, the hierarchy between environmental and population temperatures is reversed ($-\beta_M^{-1} < -T_M^{-1}$), such that the machine transition enters a cold regime. Notice that there are regions of z where $-\beta_M^{-1}$ reaches temperatures that are beyond the thresholds fixed by slab and walls temperatures. This is only obtainable in an OTE configuration, since the best one can do at thermal equilibrium is $-\beta_M = -T_{\text{eq}}^{-1}$, with either $T_{\text{eq}} = T_S$ or $T_{\text{eq}} = T_W$. Moreover, it is worth stressing that the drastic population-temperature variation between hot and cold regimes has been obtained only by tuning the slab-atoms distance, leaving T_W and T_S unchanged.

Let us now turn to the analysis of the relations between machine and qubit temperatures. Firstly, it must be pointed out that all of the transitions $\tau = \{2, q\}$ have equivalent dipoles, and that the corresponding atoms positions have the same z coordinate. Then, they all interact similarly with the EM field, and thereby they all have the same environmental temperatures: $T_M = T_q^{(i)}$ with $i \in \{1, 2, 3, 4\}$. Moreover, let us recall that a single qubit ($N = 1$) in an OTE field thermalizes to its environmental temperature. On the other hand, in the presence of the machine, interatomic interactions breaks the thermal equilibrium between the qubit and its environment: its population temperature tends to the one of the machine transition $\tau = 2$, which is either hot ($-\beta_M > -T_M^{-1}$) or cold ($-\beta_M < -T_M^{-1}$). Now, turning to the case when $N > 1$, as shown in Fig 4.5, it appears clear that all of the qubit population temperatures are driven by $-\beta_M$. In other words, the machine is able to deliver a thermal task not only on a single qubit, but on at least four of them. More specifically, in the hot-regime interval ($z \in [0.6, 10] \mu\text{m}$), the machine heats up the qubits by increasing their population temperatures, whereas refrigeration occurs within the cold regime ($z \in [10, 40] \mu\text{m}$). The strength of the Hamiltonian atom-atom interactions being much stronger than the atom(s)-field ones ($\Lambda^{(Mi)} \gg \Gamma_{\text{abs/em}}^{(ij)}$, $i, j \in \{1, 2, 3, 4\}$), the population temperatures of the qubits get much closer to $-\beta_M$ than to $-T_M^{-1}$. In particular, even when $-\beta_M$ undergoes drastic variations, as is the case during the population-inversion regime, then $-\beta_i$ with $i \in \{1, 2, 3, 4\}$ go through similar variations as well, with an intensity only slightly reduced.

To have a deeper insight, let us analyze more specifically the atomic interactions producing these results. In particular, it is important to stress that the hopping flux [Eq. (1.45)], through which the thermal tasks are delivered, is a dipole-dipole interaction. As such, the relative orientations of the interacting dipoles is an essential parameter, crucially affecting the coupling strength. Two limiting cases of relative dipole orientations exist. The first one is when the two dipoles are aligned, as is the case for the couples $(M, 1)$ and $(M, 3)$: it produces a maximal coupling, which explains why $-\beta_1$ and $-\beta_3$ are driven by $-\beta_M$. Moreover, we have $-\beta_1 = -\beta_3$ for symmetry reasons. The second limiting configuration occurs when the dipoles are orthogonal to each other. Then, the atoms are fully decoupled, and their interaction

vanishes. For this reason, the machine *interacts* neither with atom 2 nor 4. Nonetheless, as can be seen on Fig. 4.5, $-\beta_2$ and $-\beta_4$ are clearly affected by the presence of the machine. To explain this, the interactions between qubits must be taken into account. Focusing on the pair (1, 2), the two dipoles are not orthogonal to each other, and then the atoms are coupled. This is also the case for the pair (2, 3), and by symmetry, atom 4 interacts with both atoms 1 and 3, similarly to atom 2. From these interactions between qubits (*‘indirect channel’*), it follows that the thermal tasks undergone by atoms 1 and 3, due to their interaction with the machine (*‘direct channel’*), are relayed to atoms 2 and 4, which explains the variations of $-\beta_2$ and $-\beta_4$, although these two atoms are completely decoupled from M . In the following, we will refer to this mechanism as the *task-distribution mechanism*.

To reinforce this analysis, in Fig. 4.6, we investigate several correlation quantifiers, which witness interactions between different subparts of the quantum system. More specifically, we focus on the indirect channel through the bipartition composed of, on the one hand, the pair (1, 3), and on the other hand, the single atom 2. The correlations between these subsystems are described by the mutual information $\text{MI}(2 : \{1, 3\})$ [Eq. (1.46)], shown in Fig. 4.6(a). To facilitate the figure reading, $-\beta_2$ and $-T_M^{-1}$ have been incorporated (right scale). When no thermal task is performed, i.e., in the region $z < 0.6 \mu\text{m}$ when $-\beta_2 \simeq -T_M^{-1}$, the correlations vanish, witnessing the absence of interactions between the two partitions. On the other hand, when the machine is achieving either heating or cooling, $\text{MI}(2 : \{1, 3\})$ varies at the same values of z as $-\beta_2$, and with an intensity reflecting the temperature variations. In particular, the extrema of the population temperature correspond to the maxima of mutual information, suggesting that the subsystems are interacting the most at these points. This confirms that indeed, the interactions between qubits redistribute the thermal task delivered by the machine, such that, despite atom 2 is decoupled from M , its population is still affected by it. By symmetry, this is also the case for atom 4.

The correlations described by the mutual information encapsulate both classical and quantum correlations. It is legitimate to wonder in what proportions the correlations necessary to relay the thermal tasks are of classical/quantum nature. To determine this, we used the geometrical discord [Eq. (1.51)], which characterizes the quantum correlations of the bipartition $(2 : \{1, 3\})$. As can be seen, this quantity, noted $\mathcal{D}(2 : \{1, 3\})$, is close to (when not exactly) zero throughout the entire interval of z , which leads us to conclude that these correlations are of classical nature.

The interplay of the two different channels, direct and indirect, is highlighted in Fig. 4.6(b) through a many-body perspective, using tripartite correlations [Eq. (1.47)]. The direct channel is characterized by the tripartition $(M, 1, 3)$, whereas the indirect one is represented by $(1, 2, 4)$. Both $\tau(M, 1, 3)$ and $\tau(1, 2, 4)$ follow a behavior similar to the one of the population temperatures. Note that, while $\tau(M, 1, 3)$ encapsulates all of the interactions involved in the direct channel, on the other hand, the total tripartite correlations of the indirect one are $\tau(1, 2, 4) + \tau(3, 2, 4)$. Then, the task-distribution mechanism can be expressed in terms of

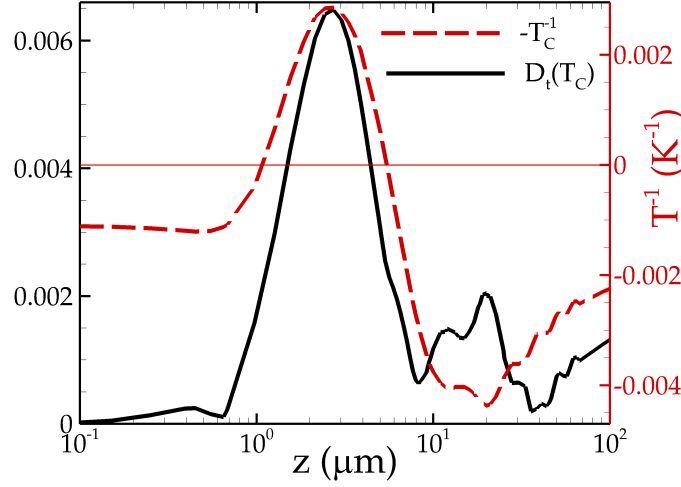


Figure 4.7: Left scale: Trace distance between the reduced state involving only the qubits and its closest thermal state, which has for temperature T_C , as a function of the slab–atoms distance. Right scale: Inverted temperature $-T_C^{-1}$.

tripartite correlations through $\tau(M, 1, 3) = \tau(1, 2, 4) + \tau(3, 2, 4)$. Moreover, by symmetry of the system, we have that $\tau(1, 2, 4) = \tau(3, 2, 4)$, leading to $\tau(M, 1, 3) \simeq 2\tau(1, 2, 4)$, which is clearly the case when the correlations are the strongest ($z \simeq 2.7 \mu\text{m}$).

Until now, our analysis has been focused on the effect of the machine on each individual qubit. An interesting aspect arising from the multipartite character of our system comes from the possibility to consider the target body, namely the qubits, as a whole, and to evaluate the thermal task performed by the machine upon it. To this end, we calculated the quantity $D_t(T_C)$, corresponding to the trace distance [Eq. (1.48)] between the density operator involving exclusively the qubits, $\rho_Q = \text{Tr}_M(\rho)$, and its closest thermal state $\rho_{\text{TS}}(T_C)$. The latter has been obtained from the family of thermal states $\rho_{\text{TS}}(T) = \exp(-H_Q/k_B T)/Z$, where $H_Q = \sum_{i=1}^N \hbar \omega_q |e_i\rangle\langle e_i|$, and Z is the partition function. A minimization of the trace distance between the states ρ_Q and $\rho_{\text{TS}}(T)$ has been realized with respect to T . The temperature minimizing this trace distance is noted by T_C , and accordingly, $\rho_{\text{TS}}(T_C)$ is by definition the closest thermal state to ρ_Q . Figure 4.7 shows both $D_t(T_C)$ and $-T_C^{-1}$ as a function of z . The first thing to point out is that $-T_C^{-1}$ has a behavior similar to the individual population temperatures of the qubits ($-\beta_i$, $i \in \{1, 2, 3, 4\}$, in Fig. 4.5). Besides, as discussed previously, in the absence of task delivery, the qubits thermalize to their environment, inducing a stationary configuration where they do not interact with each other. In this case, ρ_Q is not different from a thermal state, and $D_t(T_C) = 0$. On the other hand, when the machine is performing a task, it is relayed across the qubit subsystem through the indirect channel. Then, the corresponding density operator is not diagonal, and ρ_Q cannot be a thermal state, leading to $D_t(T_C) \neq 0$. Indeed, one can see that $D_t(T_C)$ varies accordingly with the magnitude of

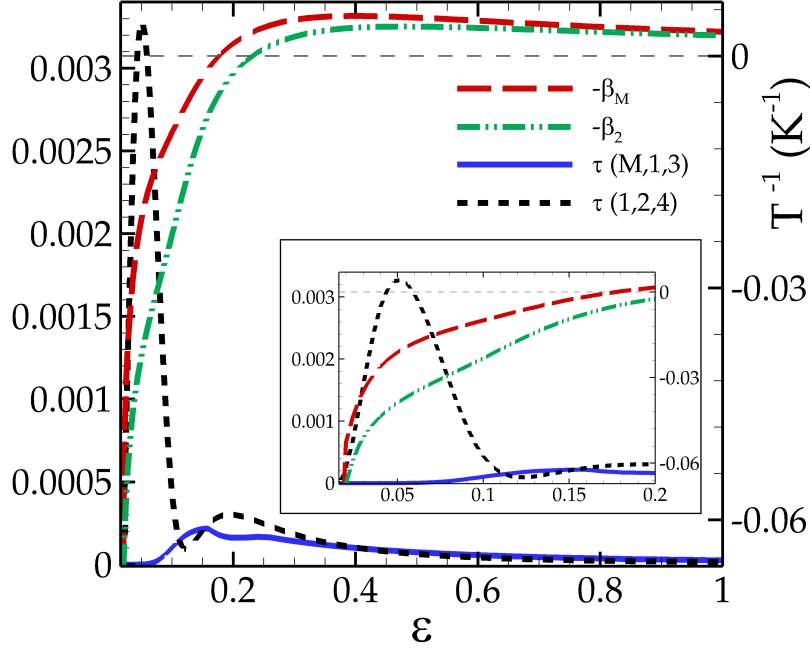


Figure 4.8: Left scale: tripartite mutual information of the partitions $(M, 1, 3)$ and $(1, 2, 4)$ as a function of ε , which parametrizes the slab and walls temperatures. Right scale: Inverted population temperatures of the machine and atom 2. Inset: Zoom into the region $\varepsilon \in [0, 0.2]$.

the population-temperature variations of the qubits. In any case, although for a number of configurations this trace distance differs from 0, it remains low, reaching at most 6×10^{-3} (recall that $0 \leq D_t(T) \leq 1, \forall T$). This means, recalling the meaning of trace distance in terms of experimental distinguishability of two quantum states, that ρ_Q is almost undistinguishable from a thermal state at T_C . Thus, it can reasonably be considered that the subsystem formed by the qubits is at thermal equilibrium with an effective environment at T_C , which is close to $\theta_2^{(M)}$, the temperature imposed by the machine. Therefore, the machine is able to perform a thermal task on a subsystem which, in terms of Hilbert space dimension, is much bigger than itself.

In the previous investigations of this Section, the environmental EM field interacting with the atomic system was modified through the slab-atoms distance. Let us now change this environment by setting $z = 2.7 \mu\text{m}$ and varying the slab and walls temperatures, T_S and T_W . This variation is performed through the parameter $\varepsilon \in [0, 1]$ as $T_S(\varepsilon) = \varepsilon T_S$ and $T_W(\varepsilon) = \varepsilon T_W$, where $\{T_W, T_S\} = \{300, 900\}$ K. The case $\varepsilon = 1$ corresponds to the configuration where the qubits are heated up the most (Fig. 4.5). In Fig. 4.8, the population temperatures of both the machine ($-\beta_M$) and atom 2 ($-\beta_2$) are pictured as a function of ε . Two regimes can be distinguished: the first one belongs (approximately) to the region

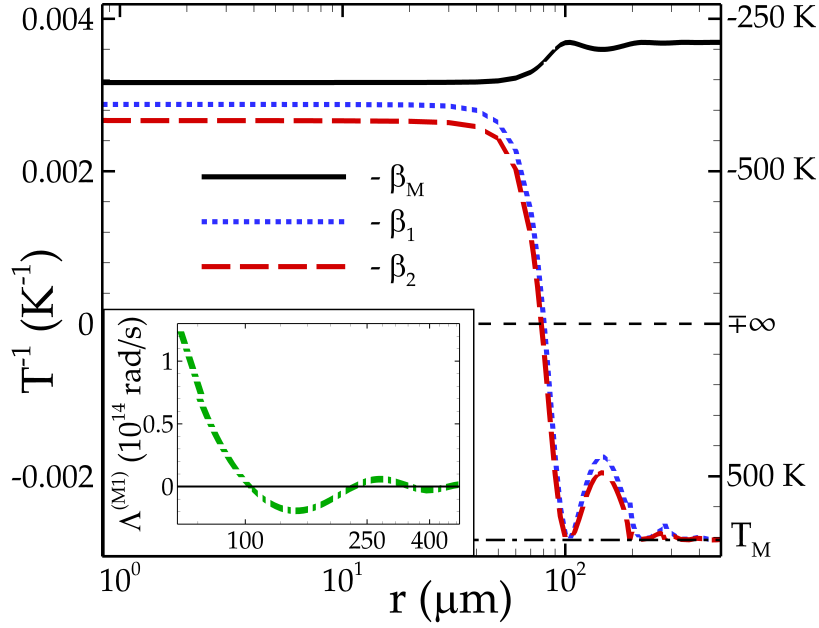


Figure 4.9: Left scale: Inverted population temperatures of the machine, atom 1 and atom 2, as a function of r , the machine-qubit distance. Right scale: Temperatures in correspondence with the left scale. Inset: Hopping strength between the machine and atom 1, as a function of r .

$\varepsilon \in [0.6, 1]$, where the two temperatures remain close to each other. This witnesses the occurrence of the task-distribution mechanism, involving direct and indirect channels, without which $-\beta_2$ would not be driven by $-\beta_M$. Moreover, it is worth pointing out that the task intensity is almost constant, despite the relatively large temperature variation, ranging from $\{T_S(0.6), T_W(0.6)\} = \{540, 180\}$ K to $\{T_S(1), T_W(1)\} = \{900, 300\}$ K. The second regime exists when $\varepsilon \leq 0.6$, where the difference between $-\beta_M$ and $-\beta_2$ increases as ε decreases, indicating the weakening of the (indirect) coupling between M and atom 2. Finally, in the limit $\varepsilon \rightarrow 0$, the EM is at thermal equilibrium, leading to the thermalization of the population temperatures to the environmental one.

To have a deeper understanding on the interplay between direct and indirect channels regarding these two regimes of ε , similarly to Fig. 4.6, we also plot in Fig. 4.8 the tripartite mutual information of $(M, 1, 3)$ and $(1, 2, 4)$. In the first regime, both functions are of the same order, and we have $\tau(M, 1, 3) > \tau(1, 2, 4)$, accordingly with the task-distribution mechanism. However, in the second regime, and more specifically within $\varepsilon \in [0.2, 0.6]$, the correlations between qubits increase significantly as ε decreases. Although $\tau(M, 1, 3)$ slightly increases as well, this occurs in a lesser extent, and the improvement of $\tau(1, 2, 4)$ indicates that the interactions between the atoms of this subsystem are enhanced. In particular, atom 1 privileges interacting with atoms 2 and 4, rather than with M and 3. As a consequence,

the thermal task is less and less delivered on atom 1, and then also on atoms 2 and 4. More remarkably, in the interval $\varepsilon \in [0, 0.15]$, $\tau(M, 1, 3)$ decreases along with ε , witnessing the reduction, and eventually the vanishing, of the interactions between the M, atom 1, and atom 3. Then, when the task-distribution mechanism is broken, the difference between $-\beta_M$ and $-\beta_2$ is the largest (see the inset), while on the other hand, the interactions between qubits are drastically enhanced, as suggest by the peak of $\tau(1, 2, 4)$. As a remark, again, recall that due to the system symmetry, the behaviors of atoms 3 and 4 are similar to the ones of atoms 1 and 2, respectively. It must be noted that entanglement between qubits with symmetric configurations in OTE environments similar to the present one has been investigated in Ref. [138].

4.6 Robustness of thermal tasks

The results of the previous Section have been obtained by considering idealized atomic positions and dipole orientations (Fig. 4.2, where the machine interactions with atoms 1 and 3 were optimized, and the ones with atoms 2 and 4 strictly zero. Having now highlighted the mechanisms producing the task delivery on the qubits, it is legitimate to wonder how robust these mechanisms are when the parameters are not ideal, similarly to realistic configurations. This is the topic of this section. In the following, the system of reference will be the one displayed in Fig. 4.2, with the distance between the slab and the atomic system being $z = 2.7 \mu\text{m}$. The slab and walls temperatures will be $T_S = 900 \text{ K}$ and $T_W = 300 \text{ K}$.

The first parameter under investigation is the distance between the machine and the qubits, noted by r . Figure 4.9 displays the population and environmental temperatures of the machine, $-\beta_M$ and $-T_M^{-1}$, as well as the population temperatures of atoms 1 and 2, $-\beta_1$ and $-\beta_2$. The slab-atoms distance being set to $z = 2.7 \mu\text{m}$, the first point in Fig. 4.9, being $r = 0.8 \mu\text{m}$, corresponds to the one of Fig. 4.5, where the qubits are heated up the most. As expected from the task-distribution mechanism, throughout the entire interval $r \in [0.8, 500] \mu\text{m}$, the inequality $-\beta_M \geq -\beta_1 \geq -\beta_2$ holds. More remarkably, the population temperatures remain on a plateau for $r \in [1, 20] \mu\text{m}$, the task delivery being then extremely robust in this entire interval. For larger values, however, machine and atoms start decoupling: $-\beta_1$ and $-\beta_2$ drop off with an oscillatory behavior, and eventually collapse to the environmental temperature, $-T_M^{-1}$.

The task-distribution mechanism occurring through hopping fluxes, having a deeper insight on the r -dependence of the tasks necessitates to look into the coefficients determining their strengths. Let us focus on the one between the machine and atom 1, namely $\Lambda^{(M1)}(\omega_q)$, shown in the inset of Fig. 4.9 (where it is denoted Λ_{M1}). According to Eq. (4.25), this term is the sum of a vacuum and a slab contributions, but numerical simulations have shown that the latter is negligible in all of our configurations. Thus, the analytical expression of the vacuum contribution can help us understanding the behavior of Λ_{M1} . From Eq. (4.26), this function

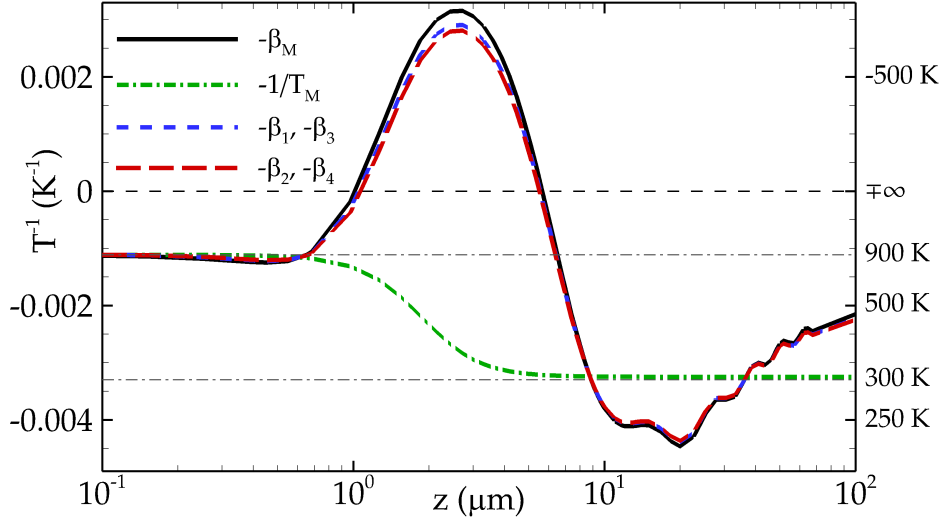


Figure 4.10: This plot is the mean of 10^3 realizations of system configurations where noise has been randomly introduced on the atomic positions (see main text). Left scale: Inverted population temperatures of all the resonant transitions, and machine environmental temperature, as a function of z . Right scale: Temperatures in correspondence with the left scale.

has an oscillatory behavior with an $1/r$ -envelop, clearly visible in the inset of Fig. 4.9. When $r \rightarrow \infty$, the amplitude of Λ_{M1} vanishes, in which case the task cannot be delivered, atoms M and 1 being decoupled. In the limit $r \rightarrow 0$, Λ_{M1} diverges, resulting in a saturation of the energy exchanges, such that the population temperatures remain constant. This saturation regime delimits the plateau region. The transition from the plateau to the oscillatory regime, i.e. when $-\beta_1$ and $-\beta_2$ begin to drop off, is determined by $r \sim c/\omega_q \simeq 37 \mu\text{m}$. In this regime, the local extrema of Λ_{M1} correspond to the ones of the population temperatures (minima for $-\beta_M$, maxima for $-\beta_1$ and $-\beta_2$).

Another important aspect we addressed is noise on the atomic positions, which we have artificially introduced on the system shown in Fig. 4.2. More specifically, we produced several realizations of the system. For each of them, the atomic positions in the plane parallel to the slab have been chosen randomly around their idealized position, with a Gaussian distribution of standard deviation $\sigma = 1 \mu\text{m}$. The dipoles of the qubits were still pointing toward the machine, whose dipole was fixed parallel to the direction joining M and atom 1 in the idealized case. Figure. 4.10 presents the atomic population temperatures as a function of z , obtained after averaging over 10^3 realizations. Remarkably, the averaged temperatures are very close to the ones of the regular configuration, except that the separation between $-\beta_1$ ($= -\beta_3$) and $-\beta_2$ ($= -\beta_4$) are slightly reduced. This result is encouraging as it reveals that, despite the non-idealized interactions due to the noisy atomic positions, the task delivery is still significant.

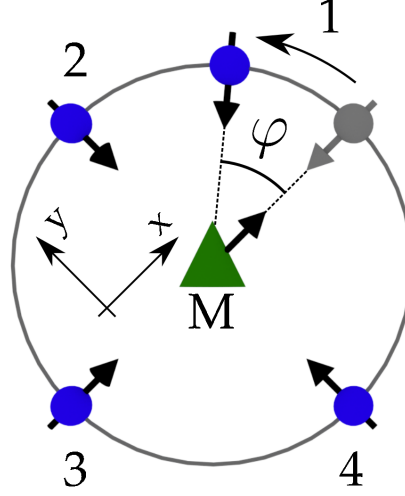


Figure 4.11: Scheme representing the rotation of atom 1 around the machine. Note that this rotation does not involve any dynamics: we consider successive steady configurations.

4.7 Tuning thermodynamical tasks

As discussed already, the task-distribution mechanism occurs through hopping fluxes. Thus, manipulating the parameters determining the strength of these fluxes offers the possibility to exert control on a thermal-task intensity. The goal of this Section is to present several methods to vary these parameters, and then, to tune a thermal task. Again, throughout this section, the slab and walls temperatures will be fixed at $T_S = 900$ K and $T_W = 300$ K, and the slab-atom distance is set to $z = 2.7 \mu\text{m}$.

Let us firstly address the situation where atom 1 is rotated around the machine, as pictured in Fig. 4.11. Its position on the circle of radius $r = 75 \mu\text{m}$ is noted by φ . Its dipole orientation varies along with φ , such that it is always pointing toward M. The case $\varphi = 0$ sets the regular configuration (Fig. 4.2), in which the system belongs to the heating regime (Fig. 4.9). Although the task intensity is not maximal ($r = 75 \mu\text{m}$ does not belong to the plateau regime of Fig. 4.9), working with this radius facilitates the manipulation of atomic positions with regards to potential practical realizations, but the following results also hold for smaller values of r . The atomic population temperatures corresponding to the rotation of atom 1 are shown in Fig. 4.12, as a function of φ (or $r\varphi$, on the upper axis). Note that the values $\varphi = \pi/2$, π , and $3\pi/2$, have not been attributed to atom 1, as they correspond to the positions of atoms 2, 3, and 4, respectively. Moreover, we stress that there is no dynamics here: the stationary solution to Eq. (4.4), from which stem the population temperatures, is computed for each value of φ .

Atom 1, similarly to atom 3, has a crucial role in the task-distribution mechanism, e.g., when $\varphi = 0$: it directly interacts with M, such that it undergoes the thermal task, and has

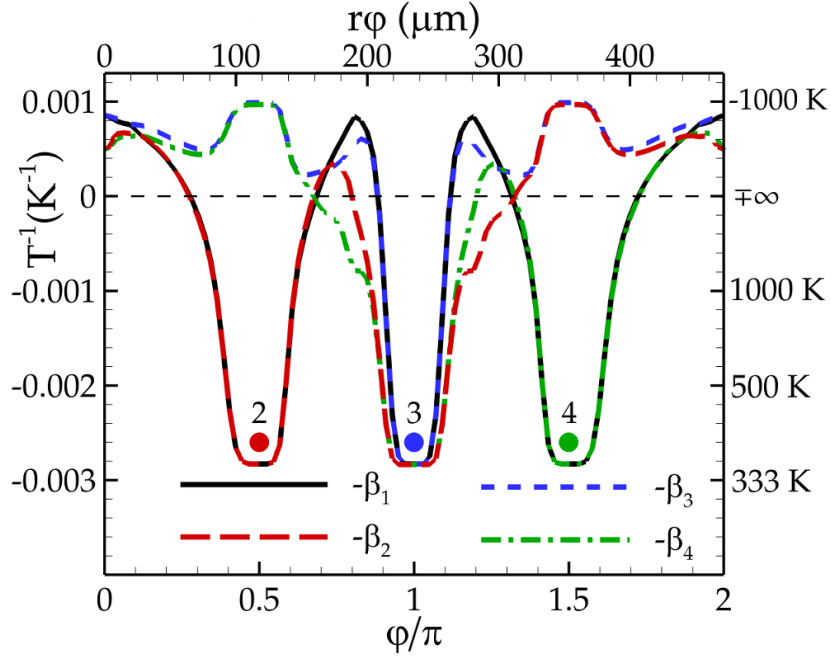


Figure 4.12: Left scale: Inverted population temperatures of the qubits. Right scale: Temperatures in correspondence with the left scale. Lower axis: angle setting the position of atom 1 around the machine. Upper axis: arc length in correspondence with the lower axis.

an interaction with both atoms 2 and 4, through which it relays the task. This privileged role comes from the fact that atom 1 interacts with all of the other atoms, which is due to its dipole orientation. When it is moved around the circle, however, this is not always the case, which has consequences on the task-distribution mechanism. In particular, when $\varphi \rightarrow \pi/2$, atoms 1 and 2 are extremely close to each other. They are decoupled from the machine, but not from atoms 3 and 4. Nonetheless, despite atom 3 is undergoing the task imposed by M, Fig. 4.12 shows that $-\beta_1$ and $-\beta_2$ both drop to the environmental temperature $-T_M^{-1}$ (not shown), witnessing that they are not affected by their interaction with atom 3. This is due to their dramatically strong coupling: on the one hand, their dipoles are (almost) aligned, such that their interaction is optimized. On the other hand, the small distance between them also induces a coupling much stronger than any other: $\Lambda^{(12)}(\omega_q) \gg \Lambda^{(1k)}(\omega_q) \simeq \Lambda^{(2k)}(\omega_q)$, for $k = 3, 4$. It follows that the subsystem (1,2) gets completely isolated from energy exchanges with the rest of the system, leading to the thermalization of $-\beta_1$ and $-\beta_2$ to $-T_M^{-1}$. On the other hand, this leaves more energy to be shared within the rest of the system, leading to larger values of $-\beta_3$ and $-\beta_4$ than in the regular configuration ($\varphi = 0$). Moreover, notice that the gap between them has almost vanished, even though only atom 3 is directly interacting with the machine. When $\varphi \rightarrow \pi$, a similar mechanism occurs between atoms 1 and 3. Their interaction dominates any other energy exchange, and thus they are decoupled from the rest of the system. In particular, there being no atom interacting with the machine, all of the

qubits thermalize to their environmental temperature: $-\beta_i = -T_M^{-1}$, for $i = 1, 2, 3, 4$. Finally, when $\varphi \rightarrow 3\pi/2$, the configuration is symmetric to the case $\varphi \rightarrow \pi/2$, where the roles of atoms 2 and 4 are swapped. In the spirit of thermal-task management, these three values of φ , namely π , $\pi/2$ and $3\pi/2$, are particularly interesting as they correspond to configurations where the thermal task is literally switched off from subparts of the system. The number of qubits affected by the machine can be either of four ($\varphi = 0$), two ($\varphi \rightarrow \pi/2, 3\pi/2$) or zero ($\varphi \rightarrow \pi$). It is worth pointing out that in these configurations, the temperatures are either close to $-\beta_M$ (not shown), for the subsystem interacting with the machine (directly or indirectly), or to $-T_M^{-1}$, for the atoms belonging to the switched-off subsystem. However, it must be stressed that intermediate values of φ are also interesting with regards to thermal-task control. As can be seen in Fig. 4.11, between two singular values of φ , the population temperatures vary smoothly between $-\beta_M$ and $-T_M^{-1}$, such that any temperature belonging to the interval defined by these two temperatures is achievable. Moreover, even small changes of φ can dramatically change the temperature distribution $(\theta_q^{(1)}, \theta_q^{(2)}, \theta_q^{(3)}, \theta_q^{(4)})$ (right scale of Fig. 4.12), as for example, passing from $(-1300, -1300, -1300, +1400)$ K for $\varphi = 0.73\pi$, to $(-1100, +1500, -1200, +1100)$ K, for $\varphi \simeq 0.8\pi$. Although the variation of φ might seem relatively small, it corresponds to an arc length of $r \times (0.8 - 0.73)\pi = 16.5 \mu\text{m}$, which is reasonable. From these two examples, it is clearly possible to produce configurations where some qubits share the same temperatures ($\varphi = 0.73\pi$), or on the contrary, systems where all of the temperatures differ for hundreds of Kelvin ($\varphi = 0.8\pi$).

Another approach for thermal-task tuning, rather than modifying atomic positions, is to manipulate the coupling between an atom and the rest of the system by changing its dipole orientation. In Fig. 4.13, we consider the system shown in Fig. 4.2, and focus on the dipole orientation of atom 4, denoted $\mu_q^{(4)}$. To this end, we introduce the angle α as the one between $\mu_q^{(4)}$ and the z axis. When $\alpha = 0$, $\mu_q^{(4)}$ points along the z axis, and thus is orthogonal to the other dipoles of the system. In this case, there possibly exists a coupling between atom 4 and the other ones, which is due to the matter contribution to the hopping strength [Eq.(4.25)]. However, according to numerical results, these interactions are negligible in comparison with the other atomic interactions involved. Then, it can be considered that atom 4 is decoupled from the system, as confirmed by $-\beta_4$, which, being isolated from the task-delivery mechanism, thermalizes to its environmental temperature. As α increases, the projection of $\mu_q^{(4)}$ on the atomic plan increases as well, which induces stronger interactions with the rest of the system. Consequently, the task-distribution mechanism begins to affect $-\beta_4$, which increases too. On the other hand, since the other atoms share their energy with atom 4, their population temperatures lower. In particular, the population temperature of atom 2, whose dipole is aligned with the atomic-plane component of $\mu_q^{(4)}$, is the most affected. Finally, when $\alpha = \pi/2$, the regular configuration is reached, where $-\beta_4 = -\beta_2$. Similarly to the previous method, the achievable temperatures belong to an interval wide of hundreds of Kelvins. In addition, one can independently tune the temperature of each atom, whereas the

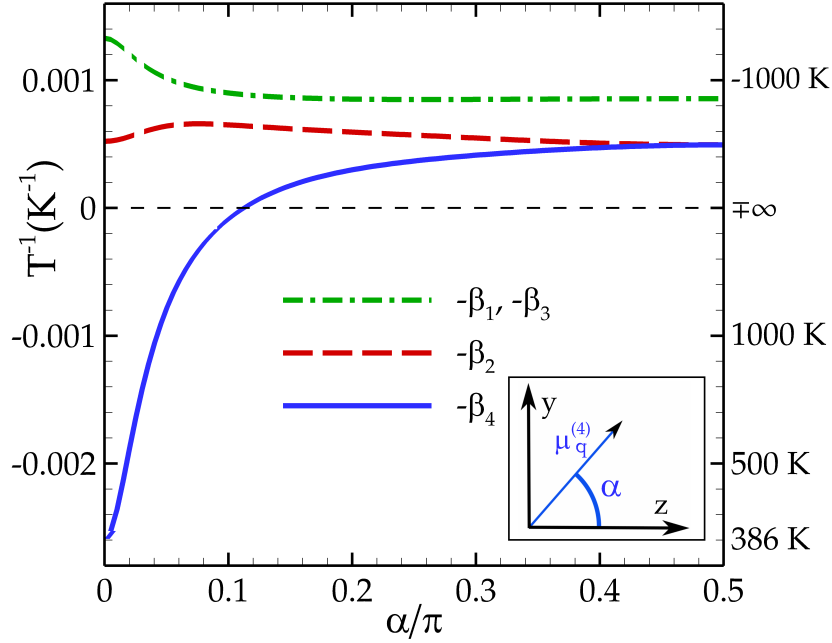


Figure 4.13: Left scale: Inverted population temperatures of the qubits as a function of α , the angle between the dipole of atom 4 and the z axis. Right scale: Temperatures in correspondence with the left scale.

previous technique induces a significant temperature modification for at least two atoms.

4.8 Variation of the number of qubits

To this point, we have only considered systems with four qubits. However, one can legitimately wonder if, with different values of N (and thus with different geometries), the task-distribution mechanism still occurs, and if it does, is the thermal task strongly affected by the size of the target body? We address these questions in the present Section.

To determine the dependence of the thermal tasks on the number of qubits, we look into the extrema of the population temperatures with respect to $z \in [0.1, 100] \mu\text{m}$. These have been determined for N varying from $N = 1$ to $N = 6$, where in each case, the qubits form a regular polygon of N edges of radius r centered to the machine. Their dipoles point toward M , while the machine dipole is always directed to atom 1. It must be stressed that for two different values of N , the temperature behaviors are extremely similar throughout the whole interval $z \in [0.1, 100] \mu\text{m}$ (e.g., see Fig. 4.5). This comes from the fact that the nature of the task performed by the machine is determined by the environmental EM field, which does not depend on N . In particular, independently of N , the maxima/minima of temperatures always occur at the same value of z .

Now turning to the analysis of Figs. 4.14(a) and 4.14(b), showing the maxima and minima

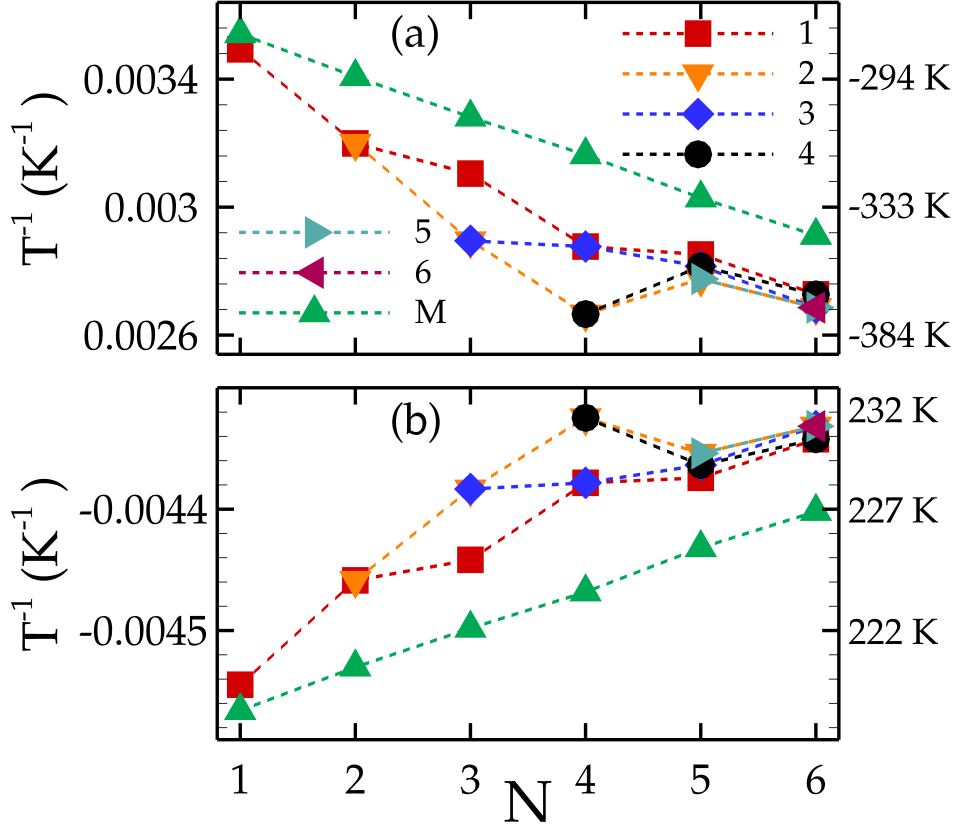


Figure 4.14: Left scale: Maximal [panel (a)] and minimal [panel (b)] population temperatures of the resonant transitions, as a function of the number of atoms present in the system, after optimization with respect to $z \in [0.1, 100] \mu\text{m}$. Right scale: Temperatures in correspondence with the left scale.

of temperatures, respectively, it appears in both cases that the machine population temperature varies linearly as N increases. This indicates that each supplementary qubit either draws or shares, depending on the role of the machine, the same amount of energy as the others already present. Let us concentrate on the heating regime [Fig. 4.14(a)]. The first aspect worth pointing out is that for each N , the population temperatures of the qubits are undergoing population inversion. This shows that not only the task-distribution mechanism is still active, but also that its intensity is large enough to significantly affect all of the qubit temperatures. When N increases, following M, these temperatures decrease as well, but not linearly. This comes from the system geometry, which is N -dependent. Indeed, according to the parity of N , the number of atoms directly interacting with the machine is either one or two, which is a parameter affecting the task-distribution mechanism. Nonetheless, this feature is relevant only when the number of atoms is rather small ($N \leq 4$): when N increases, the coupling between two neighboring atoms is reinforced, as their separation is reduced, and their dipole orientations are more favorable for interacting with each other. Then, the energy

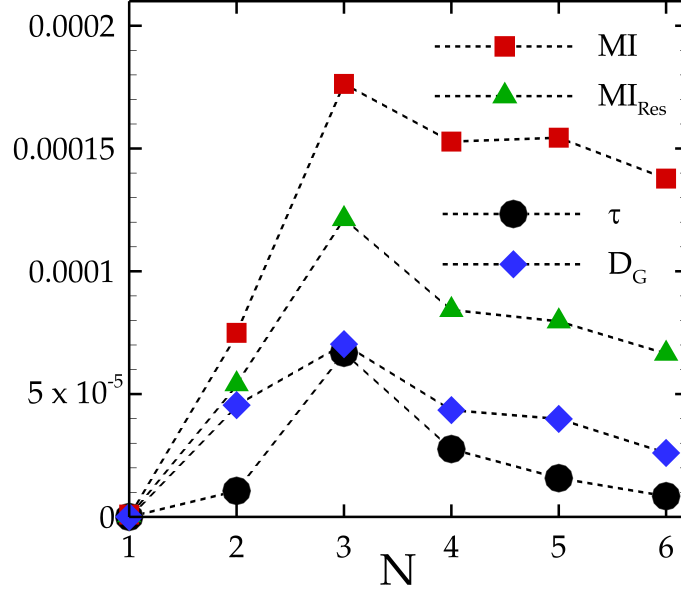


Figure 4.15: Maximal bipartite and tripartite mutual information, rescaled bipartite mutual information, and geometric quantum discord, as a function of the number of qubits present in the system. The maximization has been performed with respect to $z \in [0.1, 100] \mu\text{m}$, and over all the partitions accessible to each quantifier.

provided by the machine is distributed more evenly, leading to a population-temperatures distribution increasingly homogeneous. For example, $-\beta_1$ and $-\beta_2$ are clearly different when $N = 3$, while for $N = 5$, all of the qubit population temperatures are approximately equal. Analogous observations hold for the refrigeration case shown in Fig. 4.14(b).

To accompany the scaling of population temperatures with respect to N presented above, we also analyzed the corresponding correlations, as displayed in Fig. 4.15. The same quantifiers as the previous sections have been used, namely bi- and tri-partite mutual information, and geometric quantum discord. Let us recall that each quantifier characterizes the correlations between partitions having specific structures: any bi-(tri-)partitions for bi-(tri-)partite mutual information, and bipartition with dimensions $2 \times d$ for geometric quantum discord, where $d \in \mathbb{N}$. The number of partitions growing with N , after a first optimization over $z \in [0.1, 100] \mu\text{m}$, we selected the partitions providing the maximum values of correlations, for each quantifier. Moreover, we introduced the *rescaled mutual information*, for the following reason. The scaling of the mutual information characterizes how the correlations spread out among the system as the number of interaction channels is increased. However, its theoretical maximum value depends on the system size: for a generic bipartition AB, with dimensions d_A and d_B , this maximum is given by $\text{MI}_{\max}(\text{A:B}) = 2 \ln(\min(d_A, d_B))$. To describe the scaling of the correlations magnitude relatively to the system dimension, we de-

defined the rescaled mutual information as $MI_{\text{Res}}(A:B) = MI(A:B)/MI_{\text{max}}(A:B)$, which unlike the mutual information, belongs to $[0, 1]$, independently of N .

According to Fig. 4.15, when $N = 3$, only a single qubit has its dipole aligned with the machine dipole, such that this configuration constitutes the first system where the task-distribution mechanism is clearly occurring. This is confirmed by all the correlation quantifiers. After that, when N increases, the number of interaction channels is sufficiently large to dilute the correlations homogeneously throughout the system, inducing a diminution of the correlations.

4.9 Conclusion

In this chapter, we have investigated the energy exchanges of a quantum system composed of a three-level atom and N qubits, which is embedded in an OTE EM field. Following previous studies, we have introduced two different notions of atomic-transition temperatures, useful to investigate the energy exchanges of the system. More specifically, we have explained how the three-level atom can play the role of absorption quantum thermal machine, delivering a thermal task on a single qubit.

Pushing further the investigation, we have demonstrated that the machine is able to perform tasks of significant intensity on a target body composed of $N = 4$ qubits. Remarkably, this occurs despite the fact that two of them are completely decoupled from the machine, and comes from the *task-distribution mechanism*: the qubits interacting with the machine not only undergo the thermal task, but also relay it to the atoms non-interacting with the machine. We have supported this interpretation with the help of several correlation quantifiers. In particular, we have shown that the task-delivery mechanism produces atomic correlations of classical nature.

Besides, we have demonstrated that the qubit subsystem, when considered as a whole, is almost undistinguishable from a state at thermal equilibrium with an effective reservoir at the machine temperature. This witnesses the fact that the machine can deliver a thermal task not only on the qubits individually, but also on the subsystem composed of all the qubits, which is considerably bigger than the machine in terms of Hilbert space dimensions.

Another part of this chapter has been dedicated to the robustness of the thermal-task delivery with respect to different parameters, such as walls and slab temperatures, machine–qubits distance, or noise on the atomic positions. In all of these cases, we have shown that the machine can perform a significant task for number of configurations.

The tuning of thermal task has also been investigated, where two different strategies have been proposed. The first one consists in modifying the atomic positions, e.g., by rotating an atom around the machine. When $N = 4$, this strategy offers the possibility to switch off/on subsystems composed of 2 or 4 qubits, namely, to make them thermalize either to their environmental temperature or close to the machine population temperature, which can be

dramatically different. The second strategy achieves task tuning on individual qubits, which can be completely decoupled from the rest of the system by changing their dipole orientation. With both strategies, the tuning of the qubit population temperatures is achievable over interval wide of hundreds of Kelvin.

Finally, we have investigated the capacity of the machine to deliver thermal tasks on systems with different number of qubits, ranging from 1 to 6. In all of these configurations, the task performed by the machine is always significant, although losing in intensity with increasing N . Besides, the qubit population temperatures are sensitive to the system geometry when $N \leq 4$, whereas above that number, the energy is more and more evenly distributed throughout the qubit subsystem. This investigation has been supported by an analysis of the correlations as a function of N .

Conclusion

The results presented in this thesis have been obtained in the framework of investigations related to energy management at the atomic scale. Indeed, each of the three systems explored from Chap. 2 to Chap. 4 have revealed particularly interesting properties in the aim of manipulating energy exchanges in open quantum systems. Let us briefly summarize these different results.

In Chap. 1 we have considered a simple system composed of N two-level atoms weakly interacting with an environmental electric field. Under several assumptions, including the Born-Markov approximation, we have derived a Markovian quantum master equation describing the dynamics of the quantum system. From there, we have been able to introduce quantum-thermodynamical quantities, such as internal energy of the open system, as well as the quantum versions of heat and work. We have identified the different heat fluxes characterizing energy exchanges either between the environment and the open system, or between its different subparts.

Chapter 2 has been dedicated to energy-transport efficiency in chains of two-level atoms interacting with a blackbody radiation. We have shown that for specific (but reasonable) parameters, such as atomic positions, environment temperature, and number of atoms composing the chain, the efficiency could remarkably reach values up to 1400%. A detailed analysis of the heat fluxes at steady state and during the dynamics has revealed the role played by the excitation injector, an atomic triplet whose interactions result in the absorption of energy from the field, leading to an enhancement of the amount of energy extracted from the chain. We have discussed the robustness of efficiency amplification against small geometry variations. In addition, we have pointed out the fact that efficiency amplification is accompanied by a significant extension of the transport range, which can be increased by a factor 8 in some cases.

Energy-transport efficiency has been also the subject of Chap. 3, where a chain of two-level atoms is located at the interface between biasable plasma and an opaque medium. In the presence of magnetic field, the biased plasma is a photonic topological insulator, allowing the existence of a unidirectional SPP at its interface, propagating in the bulk bandgap and assisting energy transport along the chain. After comparison with energy transport assisted by reciprocal SPP, we have shown that the one-way SPP leads to a much better transport-efficiency, which is amplified by one or more order of magnitudes with respect to the bidirectional case. We have also highlighted that the unidirectional SPP transports energy over larger distances. In addition, due to properties of the PTI, the one-way SPP has the remarkable feature of being backscattering immune. As such, contrary to the reciprocal case, the presence of considerable defect at the interface barely affects its propagation, resulting in a transport efficiency almost as large as the one in the absence of defect. The possibility to

switch on/off the energy-transport process through the biasing field has also been discussed.

Finally, Chap. 4 has been dedicated to the study of a multipartite quantum system embedded in an out-of-thermal-equilibrium electromagnetic field, where a three-level atom functions as an absorption quantum thermal machine, heating up or cooling down the qubits located around it. We have shown that despite the increasing number of qubits, the machine is able to deliver thermal tasks on all of them with a considerable intensity, and in particular to bring them to population inversion. We have also pointed out geometric configurations involving four qubits, two of them being decoupled from the machine. Nevertheless, their population temperatures are still affected by the presence of the machine, revealing the existence of the task-distribution mechanism: the task is spread within the whole qubit system due to qubit–qubit interactions. This mechanism has been discussed in terms of bi- and tri-partite correlations, and we have demonstrated that bipartite geometric quantum discord remains negligible, independently of the task intensity. Moreover, thermal task delivery has proven to be robust against the variation of atomic positions, and of slab and walls temperature. Last but not least, we have pointed out methods for tuning thermal tasks by manipulating either the atomic positions or the qubits dipole orientations.

List of publications

The results presented in this thesis have been published in the following papers:

- B. Leggio, P. Doyeux, R. Messina and M. Antezza, *Distributed thermal tasks on many-body systems through a single quantum machine*, Europhysics Letters **112**, 40004 (2015)
- P. Doyeux, B. Leggio, R. Messina and M. Antezza, *Quantum thermal machine acting on a many-body quantum system: Role of correlations in thermodynamic tasks*, Physical Review E **92**, 022134 (2016)
- P. Doyeux, R. Messina, B. Leggio and M. Antezza, *Excitation injector in an atomic chain: Long-range transport and efficiency amplification*, Physical Review A **95**, 012138 (2017)
- P. Doyeux, S. A. Hassani Gangaraj, G. W. Hanson and M. Antezza, *Giant interatomic energy-transport amplification with nonreciprocal photonic topological insulators*, Physical Review Letter **119**, 173901 (2017)

Notes on the numerical results

This thesis contains all the equations and the physical parameters necessary to reproduce the presented numerical results. In particular, the dynamics of the miscellaneous systems are obtained from Markovian quantum master equations, such that two main steps can be identified to compute the systems dynamics: (i) the calculation of the coefficients involved in the master equations, (ii) the solution of the master equation. Step (i) is extremely system-dependent as the master-equation coefficients stem from the environment of the open quantum system. To be more explicit:

- Chapter 2: the quantum system is in *free space*, its dynamics is given by Eq. (2.2), and the corresponding coefficients can be obtained from Eqs. (2.6), (2.7) and (2.8),
- Chapter 3: the quantum system is located at a *PTI interface*, its dynamics is expressed by Eq. (3.3) and the corresponding coefficients are given by Eqs. (3.4). In this case, it is necessary to compute the Green's function solution to Eq. (2) of Ref. [75] with the permittivity given in Eq. (3.1) of this thesis. In the present work, it was computed using finite element method. For more details, please contact S. Ali Hassani Gangaraj (ali.gangaraj@gmail.com),
- Chapter 4: the environment of the quantum system is an *OTE electromagnetic field in the presence of a body*, the coefficients of the master equation Eq. (4.4) are given by Eqs. (4.23), (4.24), and (4.25). The numerical calculation of these coefficients can be relatively difficult. In particular, we would suggest to compute the integrals (4.17), (4.18) and (4.27) (with Eqs. (4.29) in the case where the body is a slab) using C/C++ routines (e.g., "gsl_integration_cquad").

Once step (i) has been achieved, in our case, we have realized step (ii) with the help of the Python-package QuTiP [139], which can give both the time evolution and the stationary state of the open quantum system. Different computers have been used to realize the simulations, all of them having approximately the following properties:

- Memory: 60 GiB
- Processor Intel Xeon (R) CPU ES-2680 v2 @ 2.80 GHz x40
- OS type: 64-bit

With these machines, the typical time to realize a full simulation, that is fulfill steps (i) and (ii) for a single system set up is only of a few minutes at most (except in the case of Chap. 3, where the Green's-function calculation can sometimes be tricky). Note that although these machines are relatively powerful, standard laptops can perfectly be used as well, with a computation time a bit longer but still reasonable.

Bibliography

- [1] Chris Monroe et al. “Demonstration of a fundamental quantum logic gate”. In: *Physical review letters* 75.25 (1995), p. 4714 (cit. on pp. v, xi).
- [2] Immanuel Bloch, Jean Dalibard, and Sylvain Nascimbene. “Quantum simulations with ultracold quantum gases”. In: *Nat Phys* 8.4 (Apr. 2012), pp. 267–276 (cit. on pp. v, xi).
- [3] John Clarke and Frank K. Wilhelm. “Superconducting quantum bits”. In: *Nature* 453.7198 (June 2008), pp. 1031–1042 (cit. on pp. v, xi).
- [4] M Wallquist et al. “Hybrid quantum devices and quantum engineering”. In: *Physica Scripta* T137 (Dec. 2009), p. 014001 (cit. on pp. v, xi).
- [5] L.-M. Duan et al. “Long-distance quantum communication with atomic ensembles and linear optics”. In: *Nature* 414.6862 (2001), pp. 413–418 (cit. on pp. v, xi).
- [6] H. J. Kimble. “The quantum internet”. In: *Nature* 453.7198 (June 2008), pp. 1023–1030 (cit. on pp. v, xi).
- [7] T. D. Ladd et al. “Quantum computers”. In: *Nature* 464.7285 (Mar. 2010), pp. 45–53 (cit. on pp. v, xi).
- [8] Gregory S. Engel et al. “Evidence for wavelike energy transfer through quantum coherence in photosynthetic systems”. In: *Nature* 446.7137 (Apr. 2007), pp. 782–786 (cit. on pp. v, xi, 17).
- [9] Elisabetta Collini et al. “Coherently wired light-harvesting in photosynthetic marine algae at ambient temperature”. In: *Nature* 463.7281 (Feb. 2010), pp. 644–647 (cit. on pp. v, xi, 17).
- [10] G. Panitchayangkoon et al. “Long-lived quantum coherence in photosynthetic complexes at physiological temperature”. en. In: *Proceedings of the National Academy of Sciences* 107.29 (July 2010), pp. 12766–12770 (cit. on pp. v, xi, 17).
- [11] Robert E. Blankenship et al. “Comparing photosynthetic and photovoltaic efficiencies and recognizing the potential for improvement”. In: *science* 332.6031 (2011), pp. 805–809 (cit. on pp. v, xi, 17).
- [12] H. J. Briegel and S. Popescu. “Intra-molecular refrigeration in enzymes”. en. In: *Proceedings of the Royal Society A: Mathematical, Physical and Engineering Sciences* 469.2158 (July 2013), pp. 20110290–20110290 (cit. on pp. v, xi, 62).
- [13] Daniel Manzano et al. “Quantum transport efficiency and Fourier’s law”. en. In: *Physical Review E* 86.6 (Dec. 2012) (cit. on pp. v, xi).

- [14] Michael Ramm, Thaned Pruttivarasin, and Hartmut Häffner. “Energy transport in trapped ion chains”. In: *New Journal of Physics* 16.6 (June 2014), p. 063062 (cit. on pp. v, xi).
- [15] A. Bermudez, M. Bruderer, and M. B. Plenio. “Controlling and Measuring Quantum Transport of Heat in Trapped-Ion Crystals”. en. In: *Physical Review Letters* 111.4 (July 2013) (cit. on pp. v, xi).
- [16] Sarah Mostame et al. “Quantum simulator of an open quantum system using superconducting qubits: exciton transport in photosynthetic complexes”. In: *New Journal of Physics* 14.10 (2012), p. 105013 (cit. on pp. v, xi).
- [17] Patrick Rebentrost et al. “Environment-assisted quantum transport”. In: *New Journal of Physics* 11.3 (Mar. 2009), p. 033003 (cit. on pp. v, xi, 18).
- [18] Bruno Leggio, Bruno Bellomo, and Mauro Antezza. “Quantum thermal machines with single nonequilibrium environments”. In: *Phys. Rev. A* 91 (1 2015), p. 012117 (cit. on pp. v, ix, xi, 62, 63, 74–76).
- [19] D. Bouchet et al. “Long-Range Plasmon-Assisted Energy Transfer between Fluorescent Emitters”. en. In: *Physical Review Letters* 116.3 (Jan. 2016) (cit. on pp. vi, xi).
- [20] Pierre Doyeux et al. “Excitation injector in an atomic chain: Long-range transport and efficiency amplification”. In: *Phys. Rev. A* 95 (1 2017), p. 012138 (cit. on pp. vii, xii, 18).
- [21] Pierre Doyeux et al. “Giant interatomic energy-transport amplification with nonreciprocal photonic topological insulators”. In: *Phys. Rev. Lett.* 119 (2017), p. 173901 (cit. on pp. viii, xii, 44).
- [22] Bruno Leggio et al. “Distributed thermal tasks on many-body systems through a single quantum machine”. In: *EPL (Europhysics Letters)* 112.4 (Nov. 2015), p. 40004 (cit. on pp. ix, xiii, 61, 62).
- [23] Pierre Doyeux et al. “Quantum thermal machine acting on a many-body quantum system: Role of correlations in thermodynamic tasks”. en. In: *Physical Review E* 93.2 (Feb. 2016), p. 022134 (cit. on pp. ix, xiii, 61, 62).
- [24] Heinz-Peter Breuer and F. Petruccione. *The Theory Of Open Quantum Systems*. Berlin: Oxford University, 2002 (cit. on pp. 2, 6, 8, 57).
- [25] Bruno Bellomo and Mauro Antezza. “Creation and protection of entanglement in systems out of thermal equilibrium”. In: *New Journal of Physics* 15.11 (2013), p. 113052 (cit. on pp. 2, 67, 70).
- [26] Zbigniew Ficek and Stuart Swain. *Quantum interference and coherence: theory and experiments*. Springer series in optical sciences. New York: Springer, 2005 (cit. on pp. 2, 6, 14, 70).

- [27] S. Ali Hassani Gangaraj, George W. Hanson, and Mauro Antezza. “Robust entanglement with three-dimensional nonreciprocal photonic topological insulators”. In: *Phys. Rev. A* 95 (6 2017), p. 063807 (cit. on pp. 2, 6, 47, 48, 52, 56).
- [28] Bruno Bellomo et al. “Quantum systems in a stationary environment out of thermal equilibrium”. In: *Phys. Rev. A* 87 (1 2013), p. 012101 (cit. on pp. 8, 63).
- [29] R Alicki. “The quantum open system as a model of the heat engine”. In: *Journal of Physics A: Mathematical and General* 12.5 (1979), p. L103 (cit. on p. 8).
- [30] Ronnie Kosloff. “A quantum mechanical open system as a model of a heat engine”. In: *The Journal of Chemical Physics* 80.4 (1984), pp. 1625–1631 (cit. on p. 8).
- [31] Roger Balian. *From Microphysics To Macrophysics: Methods And Applications Of Statistical Physics*. Berlin: Springer-Verlag, 1991 (cit. on p. 8).
- [32] H. Weimer et al. “Local effective dynamics of quantum systems: A generalized approach to work and heat”. In: *EPL (Europhysics Letters)* 83.3 (2008), p. 30008 (cit. on p. 10).
- [33] V. Vedral. “The role of relative entropy in quantum information theory”. In: *Rev. Mod. Phys.* 74 (1 2002), pp. 197–234 (cit. on p. 11).
- [34] Harold Ollivier and Wojciech H. Zurek. “Quantum Discord: A Measure of the Quantumness of Correlations”. In: *Phys. Rev. Lett.* 88 (1 2001), p. 017901 (cit. on pp. 11, 12).
- [35] Gian Luca Giorgi et al. “Genuine Quantum and Classical Correlations in Multipartite Systems”. In: *Phys. Rev. Lett.* 107 (19 2011), p. 190501 (cit. on p. 11).
- [36] Jonas Maziero and Fábio M. Zimmer. “Genuine multipartite system-environment correlations in decoherent dynamics”. In: *Phys. Rev. A* 86 (4 2012), p. 042121 (cit. on p. 11).
- [37] N. A. Nielsen and I. L. Chuang. *Quantum Computation and Information*. Cambridge University Press, 2000 (cit. on pp. 11, 12).
- [38] Alexei Gilchrist, Nathan K. Langford, and Michael A. Nielsen. “Distance measures to compare real and ideal quantum processes”. In: *Phys. Rev. A* 71 (6 2005), p. 062310 (cit. on p. 12).
- [39] Kavan Modi et al. “The classical-quantum boundary for correlations: Discord and related measures”. In: *Rev. Mod. Phys.* 84 (4 2012), pp. 1655–1707 (cit. on p. 12).
- [40] F. M. Paula et al. “Overcoming ambiguities in classical and quantum correlation measures”. In: *EPL (Europhysics Letters)* 108.1 (2014), p. 10003 (cit. on p. 12).
- [41] D Spehner and M Orszag. “Geometric quantum discord with Bures distance: the qubit case”. In: *Journal of Physics A: Mathematical and Theoretical* 47.3 (2014), p. 035302 (cit. on p. 12).

- [42] S. Matthew Menke and Russell J. Holmes. “Exciton diffusion in organic photovoltaic cells”. en. In: *Energy Environ. Sci.* 7.2 (2014), pp. 499–512 (cit. on p. 17).
- [43] Johannes Schachenmayer et al. “Cavity-Enhanced Transport of Excitons”. In: *Phys. Rev. Lett.* 114 (19 2015), p. 196403 (cit. on p. 17).
- [44] Johannes Feist and Francisco J. Garcia-Vidal. “Extraordinary Exciton Conductance Induced by Strong Coupling”. en. In: *Physical Review Letters* 114.19 (May 2015) (cit. on p. 17).
- [45] Alexander N. Poddubny. “Collective Förster energy transfer modified by a planar metallic mirror”. en. In: *Physical Review B* 92.15 (Oct. 2015) (cit. on p. 17).
- [46] Carlos Gonzalez-Ballester et al. “Harvesting excitons through plasmonic strong coupling”. In: *Phys. Rev. B* 92 (12 2015), p. 121402 (cit. on p. 17).
- [47] G. S. Schlau-Cohen. “Principles of light harvesting from single photosynthetic complexes”. en. In: *Interface Focus* 5.3 (Apr. 2015), pp. 20140088–20140088 (cit. on p. 17).
- [48] F. Caruso et al. “Highly efficient energy excitation transfer in light-harvesting complexes: The fundamental role of noise-assisted transport”. en. In: *The Journal of Chemical Physics* 131.10 (2009), p. 105106 (cit. on p. 18).
- [49] Arend G Dijkstra and Yoshitaka Tanimura. “The role of the environment time scale in light-harvesting efficiency and coherent oscillations”. In: *New Journal of Physics* 14.7 (July 2012), p. 073027 (cit. on p. 18).
- [50] Seth Lloyd and Masoud Mohseni. “Symmetry-enhanced supertransfer of delocalized quantum states”. In: *New Journal of Physics* 12.7 (July 2010), p. 075020 (cit. on p. 18).
- [51] Daniel Manzano. “Quantum transport in networks and photosynthetic complexes at the steady state”. In: *PloS one* 8.2 (2013), e57041 (cit. on p. 18).
- [52] Leonardo Novo, Masoud Mohseni, and Yasser Omar. “Disorder-assisted quantum transport in suboptimal decoherence regimes”. en. In: *Scientific Reports* 6.1 (May 2016) (cit. on p. 18).
- [53] M B Plenio and S F Huelga. “Dephasing-assisted transport: quantum networks and biomolecules”. In: *New Journal of Physics* 10.11 (Nov. 2008), p. 113019 (cit. on p. 18).
- [54] Torsten Scholak, Thomas Wellens, and Andreas Buchleitner. “Optimal networks for excitonic energy transport”. In: *Journal of Physics B: Atomic, Molecular and Optical Physics* 44.18 (Sept. 2011), p. 184012 (cit. on p. 18).
- [55] Chen Wang, Jie Ren, and Jianshu Cao. “Nonequilibrium Energy Transfer at Nanoscale: A Unified Theory from Weak to Strong Coupling”. en. In: *Scientific Reports* 5.1 (Dec. 2015) (cit. on p. 18).

- [56] Ivan Kassal and Alán Aspuru-Guzik. “Environment-assisted quantum transport in ordered systems”. In: *New Journal of Physics* 14.5 (May 2012), p. 053041 (cit. on p. 18).
- [57] Jianlan Wu, Robert J. Silbey, and Jianshu Cao. “Generic Mechanism of Optimal Energy Transfer Efficiency: A Scaling Theory of the Mean First-Passage Time in Exciton Systems”. en. In: *Physical Review Letters* 110.20 (May 2013) (cit. on p. 18).
- [58] B. Leggio, R. Messina, and M. Antezza. “Thermally activated nonlocal amplification in quantum energy transport”. In: *Europhys. Lett.* 110.4 (May 2015), p. 40002 (cit. on pp. 18, 21).
- [59] Randy L. Haupt and S. E. Haupt. *Practical Genetic Algorithms*. Hoboken: Wiley, 2004 (cit. on p. 39).
- [60] M. Z. Hasan and C. L. Kane. “Colloquium”. In: *Rev. Mod. Phys.* 82 (4 2010), pp. 3045–3067 (cit. on p. 43).
- [61] S. Raghu and F. D. M. Haldane. “Analogues of quantum-Hall-effect edge states in photonic crystals”. In: *Phys. Rev. A* 78 (3 2008), p. 033834 (cit. on pp. 43, 45).
- [62] F. D. M. Haldane and S. Raghu. “Possible Realization of Directional Optical Waveguides in Photonic Crystals with Broken Time-Reversal Symmetry”. In: *Phys. Rev. Lett.* 100 (1 2008), p. 013904 (cit. on pp. 43, 45).
- [63] Zheng Wang et al. “Reflection-Free One-Way Edge Modes in a Gyromagnetic Photonic Crystal”. In: *Phys. Rev. Lett.* 100 (2008), p. 013905 (cit. on p. 44).
- [64] Zheng Wang et al. “Observation of unidirectional backscattering-immune topological electromagnetic states”. In: *Nature* (2009) (cit. on pp. 44, 45).
- [65] Mikael C. Rechtsman et al. “Photonic Floquet topological insulators”. In: *Nature* 496.7444 (2013). Letter, pp. 196–200 (cit. on p. 44).
- [66] Mikael C. Rechtsman et al. “Topological Creation and Destruction of Edge States in Photonic Graphene”. In: *Phys. Rev. Lett.* 111 (10 2013), p. 103901 (cit. on p. 44).
- [67] Mário G. Silveirinha. “Chern invariants for continuous media”. In: *Phys. Rev. B* 92 (12 2015), p. 125153 (cit. on pp. 44, 46).
- [68] K Stannigel, P Rabl, and P Zoller. “Driven-dissipative preparation of entangled states in cascaded quantum-optical networks”. In: *New Journal of Physics* 14.6 (June 2012), p. 063014 (cit. on p. 44).
- [69] Tomás Ramos et al. “Quantum Spin Dimers from Chiral Dissipation in Cold-Atom Chains”. en. In: *Physical Review Letters* 113.23 (Dec. 2014) (cit. on p. 44).
- [70] Carlos Gonzalez-Ballesterio et al. “Chiral route to spontaneous entanglement generation”. en. In: *Physical Review B* 92.15 (Oct. 2015) (cit. on p. 44).

- [71] Hannes Pichler et al. “Quantum optics of chiral spin networks”. en. In: *Physical Review A* 91.4 (Apr. 2015) (cit. on p. 44).
- [72] R. J. Coles et al. “Chirality of nanophotonic waveguide with embedded quantum emitter for unidirectional spin transfer”. In: *Nature Communications* 7 (Mar. 2016), p. 11183 (cit. on p. 44).
- [73] Sahand Mahmoodian, Peter Lodahl, and Anders S. Sørensen. “Quantum Networks with Chiral-Light-Matter Interaction in Waveguides”. en. In: *Physical Review Letters* 117.24 (Dec. 2016) (cit. on p. 44).
- [74] Peter Lodahl et al. “Chiral quantum optics”. In: *Nature* 541.7638 (Jan. 2017), pp. 473–480 (cit. on p. 44).
- [75] S. Ali Hassani Gangaraj, George W. Hanson, and Mauro Antezza. “Robust entanglement with three-dimensional nonreciprocal photonic topological insulators”. en. In: *Physical Review A* 95.6 (June 2017) (cit. on pp. 44, 99).
- [76] Kejie Fang, Zongfu Yu, and Shanhui Fan. “Realizing effective magnetic field for photons by controlling the phase of dynamic modulation”. In: *Nat Photon* 6.11 (2012), pp. 782–787 (cit. on p. 45).
- [77] Hafezi M. et al. “Imaging topological edge states in silicon photonics”. In: *Nat Photon* 7.12 (2013). Article, pp. 1001–1005 (cit. on p. 45).
- [78] Wen-Jie Chen et al. “Experimental realization of photonic topological insulator in a uniaxial metacrystal waveguide”. In: 5 (2014). Article, 5782 EP – (cit. on p. 45).
- [79] Alexander B. Khanikaev et al. “Photonic topological insulators”. In: *Nat Mater* 12.3 (2013), pp. 233–239 (cit. on p. 45).
- [80] Arthur R. Davoyan and Nader Engheta. “Theory of Wave Propagation in Magnetized Near-Zero-Epsilon Metamaterials: Evidence for One-Way Photonic States and Magnetically Switched Transparency and Opacity”. In: *Phys. Rev. Lett.* 111 (25 2013), p. 257401 (cit. on p. 46).
- [81] S. Ali Hassani Gangaraj, Andrei Nemilentsau, and George W. Hanson. “The effects of three-dimensional defects on one-way surface plasmon propagation for photonic topological insulators comprised of continuum media”. In: 6 (2016). Article, 30055 EP – (cit. on p. 46).
- [82] Hannes Pichler et al. “Quantum optics of chiral spin networks”. In: *Phys. Rev. A* 91 (4 2015), p. 042116 (cit. on pp. 47, 48).
- [83] C. Gonzalez-Ballester et al. “Chiral route to spontaneous entanglement generation”. In: *Phys. Rev. B* 92.15 (Oct. 2015), p. 155304 (cit. on pp. 47, 51).
- [84] C.W. Gardiner and P. Zoller. *The Quantum World of Ultra-cold Atoms and Light*. vol. 1. Imperial College Press, 2014 (cit. on p. 48).

- [85] Diego Martín-Cano et al. “Dissipation-driven generation of two-qubit entanglement mediated by plasmonic waveguides”. In: *Phys. Rev. B* 84 (23 2011), p. 235306 (cit. on p. 56).
- [86] H. E. D. Scovil and E. O. Schulz-DuBois. “Three-level masers as heat engines”. In: *Physical Review Letters* 2.6 (1959), p. 262 (cit. on pp. 61, 62).
- [87] M. J Henrich, M Michel, and G Mahler. “Small quantum networks operating as quantum thermodynamic machines”. In: *Europhysics Letters (EPL)* 76.6 (Dec. 2006), pp. 1057–1063 (cit. on p. 61).
- [88] Ronnie Kosloff. “A quantum mechanical open system as a model of a heat engine”. en. In: *The Journal of Chemical Physics* 80.4 (Feb. 1984), pp. 1625–1631 (cit. on p. 61).
- [89] Eitan Geva and Ronnie Kosloff. “The quantum heat engine and heat pump: An irreversible thermodynamic analysis of the three-level amplifier”. en. In: *The Journal of Chemical Physics* 104.19 (May 1996), pp. 7681–7699 (cit. on p. 61).
- [90] José P. Palao, Ronnie Kosloff, and Jeffrey M. Gordon. “Quantum thermodynamic cooling cycle”. en. In: *Physical Review E* 64.5 (Oct. 2001) (cit. on p. 61).
- [91] Hao Wang, Sanqiu Liu, and Jizhou He. “Thermal entanglement in two-atom cavity QED and the entangled quantum Otto engine”. en. In: *Physical Review E* 79.4 (Apr. 2009) (cit. on pp. 61, 62).
- [92] Yair Rezek and Ronnie Kosloff. “Irreversible performance of a quantum harmonic heat engine”. In: *New Journal of Physics* 8.5 (May 2006), pp. 83–83 (cit. on pp. 61, 62).
- [93] Obinna Abah and Eric Lutz. “Efficiency of heat engines coupled to nonequilibrium reservoirs”. In: *EPL (Europhysics Letters)* 106.2 (Apr. 2014), p. 20001 (cit. on p. 61).
- [94] Nicolas Brunner et al. “Virtual qubits, virtual temperatures, and the foundations of thermodynamics”. en. In: *Physical Review E* 85.5 (May 2012) (cit. on p. 61).
- [95] Markus J. Henrich, Günter Mahler, and Mathias Michel. “Driven spin systems as quantum thermodynamic machines: Fundamental limits”. en. In: *Physical Review E* 75.5 (May 2007) (cit. on p. 61).
- [96] Raam Uzdin, Amikam Levy, and Ronnie Kosloff. “Equivalence of Quantum Heat Machines, and Quantum-Thermodynamic Signatures”. en. In: *Physical Review X* 5.3 (Sept. 2015) (cit. on p. 61).
- [97] Upendra Harbola, Saar Rahav, and Shaul Mukamel. “Quantum heat engines: A thermodynamic analysis of power and efficiency”. In: *EPL (Europhysics Letters)* 99.5 (Sept. 2012), p. 50005 (cit. on p. 61).
- [98] Bruno Leggio and Mauro Antezza. “Otto engine beyond its standard quantum limit”. en. In: *Physical Review E* 93.2 (Feb. 2016) (cit. on p. 61).

- [99] Marlan O. Scully et al. “Quantum heat engine power can be increased by noise-induced coherence”. In: *Proceedings of the National Academy of Sciences* 108.37 (2011), pp. 15097–15100 (cit. on p. 61).
- [100] Paul Skrzypczyk et al. “The smallest refrigerators can reach maximal efficiency”. In: *Journal of Physics A: Mathematical and Theoretical* 44.49 (Dec. 2011), p. 492002 (cit. on pp. 61, 62).
- [101] Luis A. Correa et al. “Quantum-enhanced absorption refrigerators”. en. In: *Scientific Reports* 4.1 (May 2015) (cit. on pp. 61, 62).
- [102] J. E. Geusic, E. O. Schulz-DuBios, and H. E. D. Scovil. “Quantum equivalent of the Carnot cycle”. In: *Physical Review* 156.2 (1967), p. 343 (cit. on pp. 61, 62).
- [103] Ralph Silva, Paul Skrzypczyk, and Nicolas Brunner. “Small quantum absorption refrigerator with reversed couplings”. en. In: *Physical Review E* 92.1 (July 2015) (cit. on pp. 61, 62).
- [104] Amikam Levy and Ronnie Kosloff. “Quantum Absorption Refrigerator”. en. In: *Physical Review Letters* 108.7 (Feb. 2012) (cit. on pp. 61, 62).
- [105] Noah Linden, Sandu Popescu, and Paul Skrzypczyk. “How Small Can Thermal Machines Be? The Smallest Possible Refrigerator”. en. In: *Physical Review Letters* 105.13 (Sept. 2010) (cit. on pp. 61, 62).
- [106] Amikam Levy, Robert Alicki, and Ronnie Kosloff. “Quantum refrigerators and the third law of thermodynamics”. en. In: *Physical Review E* 85.6 (June 2012) (cit. on pp. 61, 62).
- [107] Nicolas Brunner et al. “Entanglement enhances cooling in microscopic quantum refrigerators”. en. In: *Physical Review E* 89.3 (Mar. 2014) (cit. on pp. 61, 62).
- [108] Yi-Xin Chen and Sheng-Wen Li. “Quantum refrigerator driven by current noise”. In: *EPL (Europhysics Letters)* 97.4 (Feb. 2012), p. 40003 (cit. on pp. 61, 62).
- [109] Davide Venturelli, Rosario Fazio, and Vittorio Giovannetti. “Minimal Self-Contained Quantum Refrigeration Machine Based on Four Quantum Dots”. en. In: *Physical Review Letters* 110.25 (June 2013) (cit. on pp. 61, 62).
- [110] Mark T Mitchison et al. “Realising a quantum absorption refrigerator with an atom-cavity system”. In: *Quantum Science and Technology* 1.1 (Mar. 2016), p. 015001 (cit. on pp. 61, 62).
- [111] J. Gemmer, M. Michel, and G. Mahler. *Quantum Thermodynamics*. Vol. 657. Lecture Notes in Physics. Berlin, Heidelberg: Springer Berlin Heidelberg, 2004 (cit. on p. 61).
- [112] Robert Alicki. “The quantum open system as a model of the heat engine”. In: *Journal of Physics A: Mathematical and General* 12.5 (1979), p. L103 (cit. on p. 61).

- [113] H. Weimer et al. “Local effective dynamics of quantum systems: A generalized approach to work and heat”. In: *EPL (Europhysics Letters)* 83.3 (Aug. 2008), p. 30008 (cit. on p. 61).
- [114] Michał Horodecki and Jonathan Oppenheim. “Fundamental limitations for quantum and nanoscale thermodynamics”. In: *Nature Communications* 4 (June 2013) (cit. on p. 61).
- [115] A. del Campo, J. Goold, and M. Paternostro. “More bang for your buck: Superadiabatic quantum engines”. en. In: *Scientific Reports* 4.1 (May 2015) (cit. on p. 61).
- [116] B. Leggio et al. “Entropy production and information fluctuations along quantum trajectories”. en. In: *Physical Review A* 88.4 (Oct. 2013) (cit. on pp. 61, 62).
- [117] B. Leggio et al. “Fluctuation theorems for non-Markovian quantum processes”. en. In: *Physical Review E* 87.3 (Mar. 2013) (cit. on pp. 61, 62).
- [118] Obinna Abah and Eric Lutz. “Optimal performance of a quantum Otto refrigerator”. In: *EPL (Europhysics Letters)* 113.6 (2016), p. 60002 (cit. on p. 61).
- [119] Obinna Abah and Eric Lutz. “Energy efficient quantum machines”. In: *EPL (Europhysics Letters)* 118.4 (2017), p. 40005 (cit. on p. 61).
- [120] Jose Joaquin Alonso, Eric Lutz, and Alessandro Romito. “Thermodynamics of Weakly Measured Quantum Systems”. In: *Phys. Rev. Lett.* 116 (8 2016), p. 080403 (cit. on p. 61).
- [121] T. B. Batalhão et al. “Irreversibility and the Arrow of Time in a Quenched Quantum System”. In: *Phys. Rev. Lett.* 115 (19 2015), p. 190601 (cit. on pp. 61, 62).
- [122] Sandu Popescu, Anthony J. Short, and Andreas Winter. “Entanglement and the foundations of statistical mechanics”. In: *Nature Physics* 2.11 (Nov. 2006), pp. 754–758 (cit. on p. 61).
- [123] Michele Campisi, Peter Hänggi, and Peter Talkner. “Colloquium : Quantum fluctuation relations: Foundations and applications”. en. In: *Reviews of Modern Physics* 83.3 (July 2011), pp. 771–791 (cit. on p. 61).
- [124] Michele Campisi, Peter Talkner, and Peter Hänggi. “Fluctuation Theorem for Arbitrary Open Quantum Systems”. en. In: *Physical Review Letters* 102.21 (May 2009) (cit. on p. 61).
- [125] Fernando Brandão et al. “The second laws of quantum thermodynamics”. en. In: *Proceedings of the National Academy of Sciences* 112.11 (Mar. 2015), pp. 3275–3279 (cit. on p. 61).
- [126] Massimiliano Esposito, Upendra Harbola, and Shaul Mukamel. “Nonequilibrium fluctuations, fluctuation theorems, and counting statistics in quantum systems”. en. In: *Reviews of Modern Physics* 81.4 (Dec. 2009), pp. 1665–1702 (cit. on p. 61).

- [127] Andreas Osterloh et al. “Scaling of entanglement close to a quantum phase transition”. In: *Nature* 416.6881 (2002), pp. 608–610 (cit. on p. 61).
- [128] Matthias Vojta. “Quantum phase transitions”. In: *Reports on Progress in Physics* 66.12 (2003), p. 2069 (cit. on p. 61).
- [129] Herbert Walther. “Quantum Coherence”. In: () (cit. on p. 61).
- [130] Paul Skrzypczyk, Anthony J. Short, and Sandu Popescu. “Work extraction and thermodynamics for individual quantum systems”. In: *Nature Communications* 5 (June 2014) (cit. on p. 61).
- [131] Johan Åberg. “Catalytic Coherence”. en. In: *Physical Review Letters* 113.15 (Oct. 2014) (cit. on p. 61).
- [132] Johannes Roßnagel et al. “A single-atom heat engine”. In: *Science* 352.6283 (2016), pp. 325–329 (cit. on p. 62).
- [133] Valentin Blickle and Clemens Bechinger. “Realization of a micrometre-sized stochastic heat engine”. In: *Nature Physics* 8.2 (Dec. 2011), pp. 143–146 (cit. on p. 62).
- [134] O. Abah et al. “Single-Ion Heat Engine at Maximum Power”. en. In: *Physical Review Letters* 109.20 (Nov. 2012) (cit. on p. 62).
- [135] Patrick P. Hofer et al. “Quantum Thermal Machine as a Thermometer”. en. In: *Physical Review Letters* 119.9 (Sept. 2017) (cit. on p. 62).
- [136] Riccardo Messina and Mauro Antezza. “Scattering-matrix approach to Casimir-Lifshitz force and heat transfer out of thermal equilibrium between arbitrary bodies”. In: *Phys. Rev. A* 84 (4 2011), p. 042102 (cit. on pp. 66, 67).
- [137] E. Albert and S. Leo. *Refrigeration*. US Patent 1,781,541. 1930 (cit. on p. 75).
- [138] Bruno Bellomo and Mauro Antezza. “Nonequilibrium dissipation-driven steady many-body entanglement”. In: *Phys. Rev. A* 91 (4 2015), p. 042124 (cit. on p. 84).
- [139] J.R. Johansson, P.D. Nation, and Franco Nori. “QuTiP 2: A Python framework for the dynamics of open quantum systems”. In: *Computer Physics Communications* 184.4 (2013), pp. 1234 –1240 (cit. on p. 99).

Abstract — This thesis deals with energy management in open quantum systems. Three different systems are under study in the limit of weak system–environment coupling, and their dynamics is described by Markovian quantum master equations. In the first chapter, the complete derivation of such equation is performed in a specific case, and several notions of quantum thermodynamics are introduced. In the first system, energy transport is investigated along atomic chains (between 2 and 7 atoms) embedded in blackbody radiation around room temperature. It is shown that the transport efficiency can reach remarkable values, exceeding 100% and reaching 1400% in some configurations. Moreover, when the efficiency is amplified, the transport range is also considerably increased. The following chapter also deals with energy transport in atomic chains. The quantum system is located at the interface of a photonic topological insulator (PTI), supporting a unidirectional surface-plasmon-polariton (SPP) immune to backscattering. The SPP propagates along the chain and assists energy transport. Comparison is made between reciprocal and unidirectional SPPs in terms of transport efficiency, and it is shown that the latter can yield an efficiency larger by one order of magnitude. In addition, several practical aspects stemming from PTIs are highlighted, including the robustness of energy transport in the presence of defects on the SPP path. In the last chapter, a quantum system embedded in an out-of-thermal-equilibrium electromagnetic field is investigated. It is composed of a three-level atom playing the role of an absorption quantum thermal machine, as well as N two-level atoms (‘qubits’), with $N = 1, \dots, 6$, which are the target bodies. It is demonstrated that the machine is able to perform significant thermal tasks on the qubits, even when their number is increased. Moreover, it is pointed out that due to qubit–qubit interactions, the tasks delivered by the machine are distributed throughout the system of interacting qubits, such that in some cases the temperature of the qubits which are completely decoupled from the machine can still be considerably affected by it. This task-distribution mechanism is investigated by means of the correlations between different subparts of the system. In addition, the tuning of thermal tasks is discussed.

Résumé — Cette thèse traite de la manipulation de l’énergie dans trois systèmes quantiques ouverts différents dans la limite de couplage faible système–environnement, et leurs dynamiques respectives sont décrites par une équation maîtresse quantique markovienne. Dans le premier chapitre, le calcul d’une telle équation est réalisé pour un système particulier, et diverses notions de thermodynamique quantique sont introduites. Pour le premier système physique, on analyse le transport d’énergie le long de chaînes atomiques (entre 2 et 7 atomes) soumises à un rayonnement de corps noir proche de la température ambiante. Il est montré que l’efficacité du transport peut atteindre des valeurs remarquables, surpassant 100% et atteignant jusqu’à 1400% dans certaines configurations. De plus, lorsque l’efficacité est amplifiée, la portée du transport est également considérablement augmentée. Le chapitre suivante traite aussi du transport d’énergie dans des chaînes atomiques. Le système quantique est placé à l’interface d’un isolant topologique photonique (ITP), qui supporte un plasmon polariton de surface (PPS) insensible à la réflexion. Le PPS se propage le long de la chaîne atomique et assiste le transport d’énergie. La comparaison est faite entre PPSs réciproque et unidirectionnel en termes d’efficacité du transport, et il est démontré que ce dernier produit une meilleure efficacité, de plus d’un ordre de grandeur. De surcroît, divers aspects pratiques dus aux propriétés des ITPs sont mis en avant, notamment la robustesse du transport d’énergie en présence de défauts sur le parcours du PPS. Enfin, un système quantique immergé dans un champ électromagnétique hors équilibre thermique est étudié. Il est composé d’un système à trois niveaux d’énergie, jouant le rôle de machine thermique quantique à absorption, ainsi que de N atomes à deux niveaux (‘qubits’) qui sont affectés par l’action de la machine. Il est montré que la machine est capable de délivrer des tâches thermiques d’intensité significative sur les qubits, y compris lorsque leur nombre augmente. De plus, il est mis en évidence qu’en raison d’interactions qubit–qubit, les tâches réalisées par la machine sont distribuées parmi l’ensemble du système des qubits en interaction, de sorte que dans certains cas, même les qubits complètement découplés de la machine subissent une modification de température considérable. Ce mécanisme de distribution des tâches est analysé à travers les corrélations entre différentes partitions du système quantique. Par ailleurs, le contrôle des tâches thermiques est également discuté.